

NONLINEAR EFFECTS IN LONG RANGE PROPAGATION

Kaëlig Castor,¹ Peter Gerstoft, W. A. Kuperman,¹ Gerald L. D'Spain,¹ and B. Edward McDonald²

Scripps Institution of Oceanography¹ and Naval Research Laboratory²

Sponsored by Defense Threat Reduction Agency

Contract No. DTRA01-00-C-0084

ABSTRACT

The Nonlinear Progressive Wave Equation (NPE) (McDonald and Kuperman, 1987) computer code was coupled with a linear normal mode code in order to study propagation from a high-intensity source in either shallow or deep water. Simulations using the coupled NPE/linear code are used to study both harmonic (high-frequency) and parametric (low-frequency) generation and propagation in shallow or deep water with long-range propagation paths. Included in the modeling are both shock dissipation and linear attenuation. The results of these studies are presented.

OBJECTIVE

Linear acoustic propagation in a waveguide has been studied extensively theoretically, numerically and experimentally. In case of a large underwater explosion, nonlinear processes affect the properties of the acoustic wave. One can expect to characterize and localize nuclear underwater explosions by examining spectrograms, which would show this specific nonlinear behavior (Kuperman et al, 2001; D'Spain et al 2000; Gerstoft, 1999).

The aim of this paper is to highlight the nonlinear phenomena of acoustical propagation such as the nonlinear steepening and shock dissipation. The nonlinear scar in a pulse propagated over long ranges is discussed. Work on this topic has also been carried out by B. Ed McDonald (2002).

Introduction

The nonlinear progressive wave equation (NPE) (McDonald *et al*, 1987; McDonald, 2000, 2002) has been developed to investigate nonlinear acoustic effects (including shocks) in an ocean waveguide. This model assumes propagation within a narrow angle and provides an alternative to the linear parabolic equation (PE) and normal mode (NM) approaches. The model is derived from the Euler equations of fluid dynamics retaining lowest order nonlinearity augmented by an adiabatic equation of state relating pressure and density. The NPE is cast in a wave-following coordinate system moving at a nominal average sound speed c_0 in a preferred propagation direction r .

For azimuthally symmetric propagation, the NPE in cylindrical (r, z) coordinates is

$$\frac{\partial R}{\partial t} = -\frac{\partial}{\partial r} \left(c_1 R + \frac{\mathbf{b} c_0}{2} R^2 \right) - \frac{c_0}{2} \frac{R}{r} - \frac{c_0}{2} \int_{rf}^r \frac{\partial^2 R}{\partial z^2} dr, \quad (1)$$

where \mathbf{b} is the nonlinear parameter (≈ 3.5 for the ocean), c_1 is the environmental sound speed fluctuation about c_0 .

$R = \mathbf{r}'/\mathbf{r}_0$ is the dimension-less density perturbation where \mathbf{r}_0 is the unperturbed density and $\mathbf{r}' = \mathbf{r} - \mathbf{r}_0$. The NPE can be also formulated in terms of a dimension-less pressure variable $Q = p'/\mathbf{r}_0 c_0^2$ by substituting R with Q in Eq. (1) (Ambrosiano *et al*, 1990). The terms on the right hand side of Eq. (1) represent from left to right, refraction, nonlinear steepening, radial spreading, and diffraction. The quadratic nonlinearity in Eq.(1) implies that the nonlinear contribution to the local sound speed is $\mathbf{b} c_0 R$. A linear propagation mode can be invoked in the code simply by setting $\mathbf{b} = 0$. The water is assumed to be an inviscid fluid and linear attenuation in the sediment layer was included.

RESEARCH ACCOMPLISHED

The nonlinear propagation of an acoustic wave induces high frequency harmonics. Furthermore, the nonlinear interaction of two monochromatic waves at frequencies f_1 and f_2 propagating in the same direction leads to a secondary radiation at frequencies $f_2 \pm f_1$. This parametric interaction effect is commonly used in many applications such as transducer realization providing high focused underwater acoustic intensity for active sonar; this effect is also used for measurements of the nonlinear parameter in liquids or biologic environments and solids (Barriere, 2002; Marchal, 2002; Lee *et al*, 1995; Hamilton *et al*, 1998).

The work presented in this paper focuses on the physical phenomena that influence the spectral distribution of the energy during propagation in order to understand the characteristics of acoustic signals measured after long-range nonlinear propagation. For this purpose, acoustic propagation for different source waveforms is investigated.

Two narrowband sources in shallow water

All the results presented in this section are for a 200-m depth Pekeris waveguide (Fig. 1.a.). The sound speed in the water column is 1500 m/s and is 1550 m/s in the sediment. At a source depth of 100 m, the NPE code is initialized by a sum of two narrowband sources centered at frequencies $f_1=275$ Hz and $f_2=425$ Hz, respectively (Fig. 2.a and 2.d). The wave packet is modulated by two Gaussian envelopes in depth and range. This source allows the study of spectral evolution of the acoustic waves due to nonlinearity within the propagation. High-frequency sources are convenient to get narrow frequency bands and to observe both harmonic and parametric generation. The aim of this section is to evaluate the relative energy associated with both effects. Figures 2.c. and 2.d. represent the depth-

averaged spectrum for two narrow band sources at the initial range and at the 280-m range where secondary waves created by both parametric ($f_2 \pm f_1$) and harmonic ($2f_1$ & $2f_2$) effects appear clearly. Higher order radiation with low amplitudes at other different frequency combinations, $2(f_2 - f_1) = 300$ Hz, $3(f_2 - f_1) = 450$ Hz, $4(f_2 - f_1) = 600$ Hz, and $f_1 + 2(f_2 - f_1) = 2f_2 + f_1 = 575$ Hz are also distinguishable.

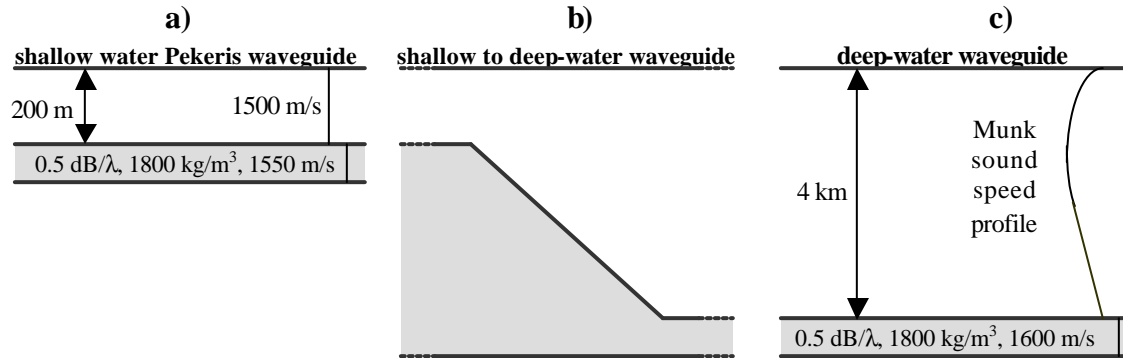


Figure 1. Representation of the environments used in the simulations.

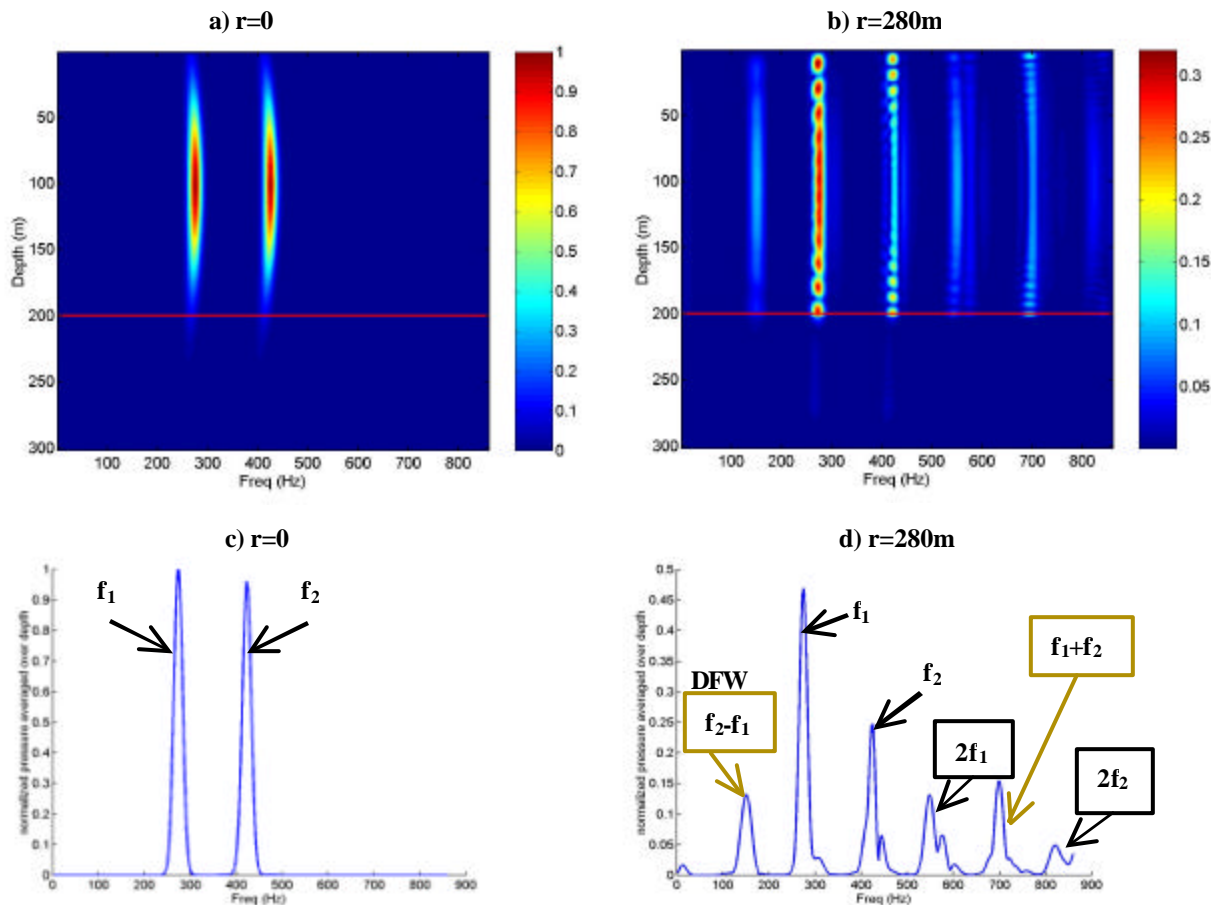


Figure 2: (a & b) Normalized spectrum for two narrow band sources ($f_1=275$ Hz, $f_2=425$ Hz) with a source overdensity $R_m=3 \cdot 10^{-5}$. (c & d) Normalized depth-averaged spectrum. (a & c) range=0. (b & d) range=280m.

Figure 3.a. represents for different maximum overdensity levels R_m the normalized total energy defined by

$$E_T(r) = \sum_i |p(f_i, r)|^2 / \sum_i |p(f_i, r=0)|^2, \quad (2)$$

where $|p(f_i, r)|$ is the amplitude of the pressure at the frequency f_i and at the range r . Even if the total energy is higher for a high source level, Figure 3(a). shows that the relative losses are much larger for high initial amplitudes since nonlinear effects induce shock dissipation in addition to classical linear absorption.

The only parametric effect considered here is the difference frequency wave (DFW) generation, which is directly related to the low-frequency generation. Figures 3(b) and 3(c) show the energy ratios E_h and E_p , respectively, associated to harmonics and DFW, which are expressed as follows

$$E_h(r) = \left(|p(2f_1, r)|^2 + |p(2f_2, r)|^2 \right) / E_i \quad (3)$$

$$\text{and } E_p(r) = |p(f_2 - f_1, r)|^2 / E_i, \quad (4)$$

with the initial energy E_i calculated such that

$$E_i = |p(f_1, r=0)|^2 + |p(f_2, r=0)|^2. \quad (5)$$

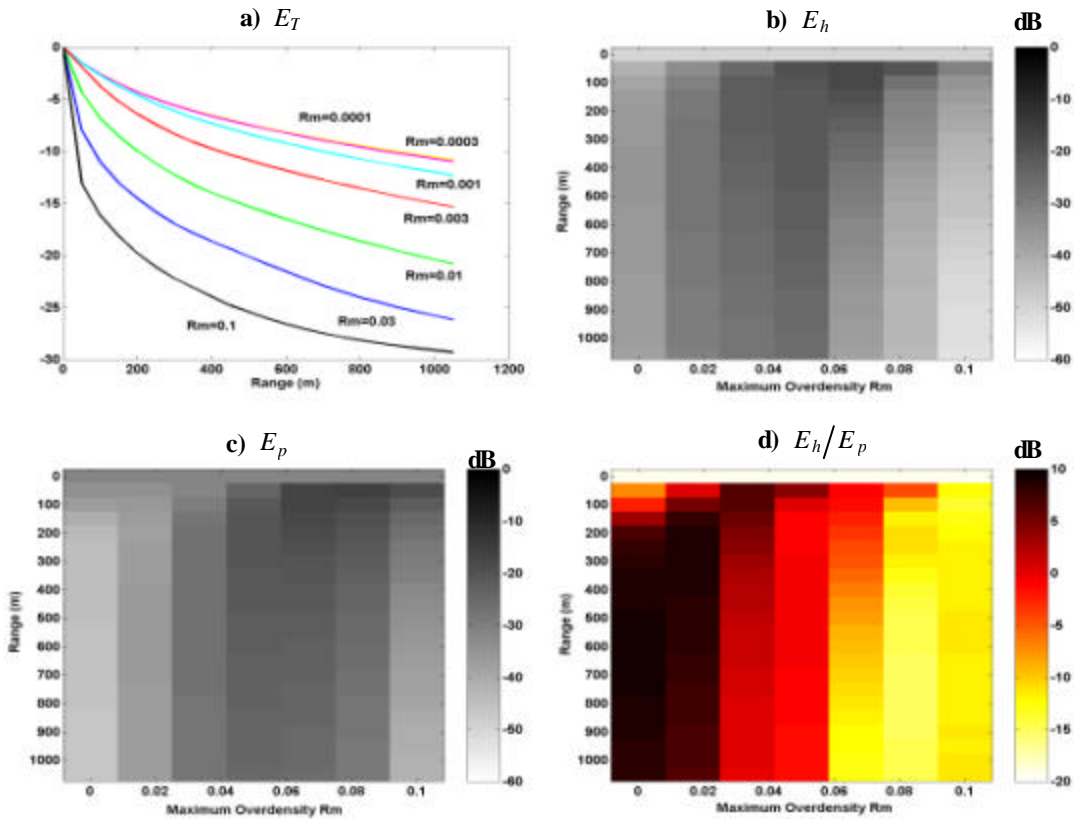


Figure 3: Energy ratios versus range and source overdensity R_m : (a) Total energy E_T , Eq. (2). (b) Energy in the first harmonic components E_h , Eq. (3). (c) Energy in the parametric difference frequency component E_p , Eq. (4). (d) Energy ratio E_h / E_p .

Near the source, both parametric DFW (E_p) and harmonic (E_h) energy increase for larger source overdensity until an optimum is reached (Fig. 3(b) and 3(c)). Both nonlinear effects are in competition with shock wave dissipation. The shock wave leads to an energy absorption process in addition to the intrinsic attenuation. When a discontinuity appears in the waveform profile, the shock wave formation distance is reached. For a shock wave, a cascade of higher frequencies is generated (Hamilton, 1998). This phenomenon increases entropy locally and constitutes a

mechanism of energy dissipation even in a perfect fluid. This shock wave formation distance decreases when the source level increases. Thus, for a strong explosion, nonlinearities are important and shock dissipation occurs at shorter ranges and leads to a high-energy decay.

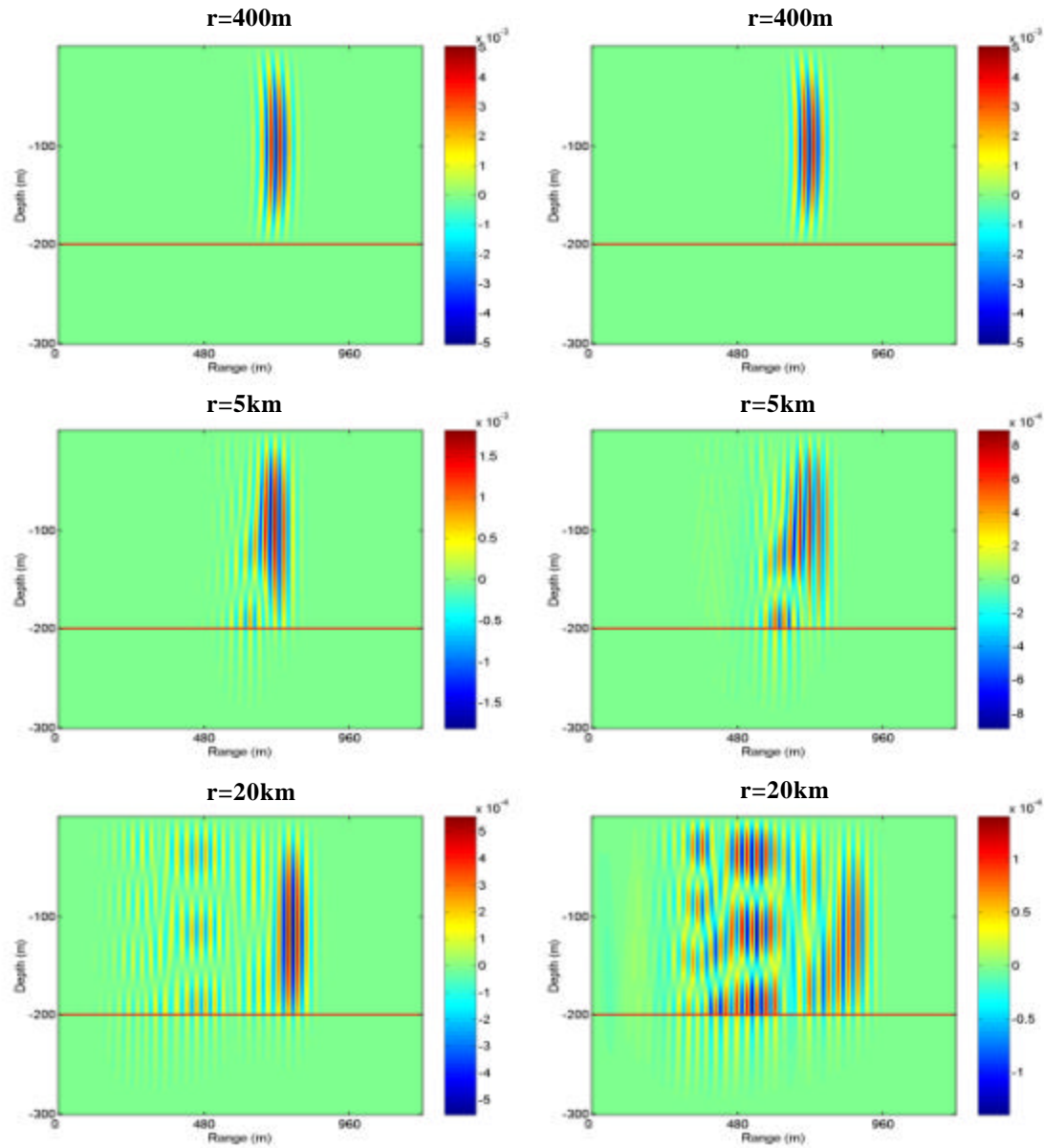


Figure 4: Snapshots at different ranges (400 m, 5 km, 20 km) for both linear (left) and nonlinear (right) shallow water cases with a single narrow band source centered at 50 Hz with a source overdensity $R_m = 3.5 \cdot 10^{-3}$.

Finally, even if harmonic (Fig. 3[b]) and difference frequency (Fig. 3[c]) generation have almost the same behavior versus range, there is a weak shift between maximum overdensities for which respective normalized energies E_h and E_p are maximal. Since absorption is more important at higher frequencies, harmonics are damped faster during propagation than the DFW. These observations are also relevant for Figure 3(d), which shows the ratio E_h/E_p . In this figure, three parts can be distinguished: The first part is for low-source overdensities where the shock wave formation distance is large. The harmonic generation due to the nonlinear steepening is greater than the parametric DFW. In the second part, for intermediate levels, both nonlinear effects are of similar importance. In the third part, for high-amplitude source, the shock wave formation distance is shorter. Strong absorption occurs then at short

ranges and leads to harmonic dissipation. The low difference frequency wave is thus predominant.

Single narrowband source

In this section, the source conditions are a five-cycle sine-wave packet with a center frequency of 50 Hz, modulated by Gaussian envelopes in depth and range. Figure 4 shows snapshots at different ranges for linear and nonlinear propagation in the Pekeris shallow water waveguide defined in part A (Fig. 1[a]). Corresponding time series are represented in Figure 5 at the source depth (100 m).

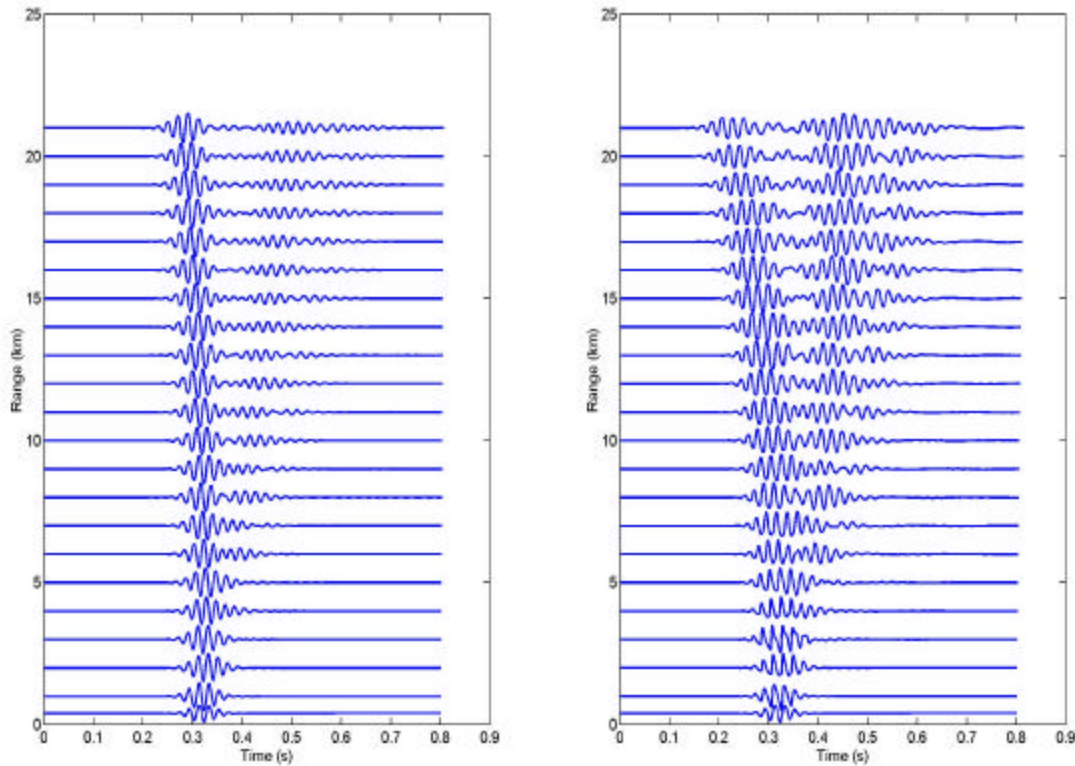


Figure 5: Time series at the source depth (100 m) for linear (left) and nonlinear (right) shallow water cases with a single narrowband source centered at 50 Hz with a source overdensity $R_m = 3.5 \cdot 10^{-3}$.

Even though the presence of nonlinearity does not lend itself to straightforward representation in linear normal modes, similarities between the two cases are expected since the nonlinearities are weak. The modal dispersion can be seen in both cases (Fig. 4). At 20-km range, four modes can be distinguished, and one can observe that the lower order modes travel faster. Because nonlinear effects lead to low- and high-frequency generation, the spectral distribution of the energy is generally more complicated and spread over a broad frequency band. Consequently, in the nonlinear case there is an energy transfer toward higher modes and the excitation of each mode is more uniform than in the linear case as can be seen at 20-km range in Figure 4. Furthermore, an important difference is the wave steepening (Fig. 5). In the nonlinear case, the wave form starts out sinusoidal, develops a sawtooth profile (range 3-6 km), and ultimately falls victim to effects of dissipation and reverts to a waveform resembling the signal at the source, although much reduced in amplitude (this attenuation is not visible in the time series representation shown in Fig. 5 since all the signals are normalized by their maximum at each range for lisibility). After an initial phase in which the nonlinear wave loses energy to shock processes and increased bottom penetration, its interaction with the waveguide becomes essentially linear. Then, a linear adiabatic normal mode code can be used to propagate the field to much longer ranges (i.e. several hundred kilometers), using less CPU time.

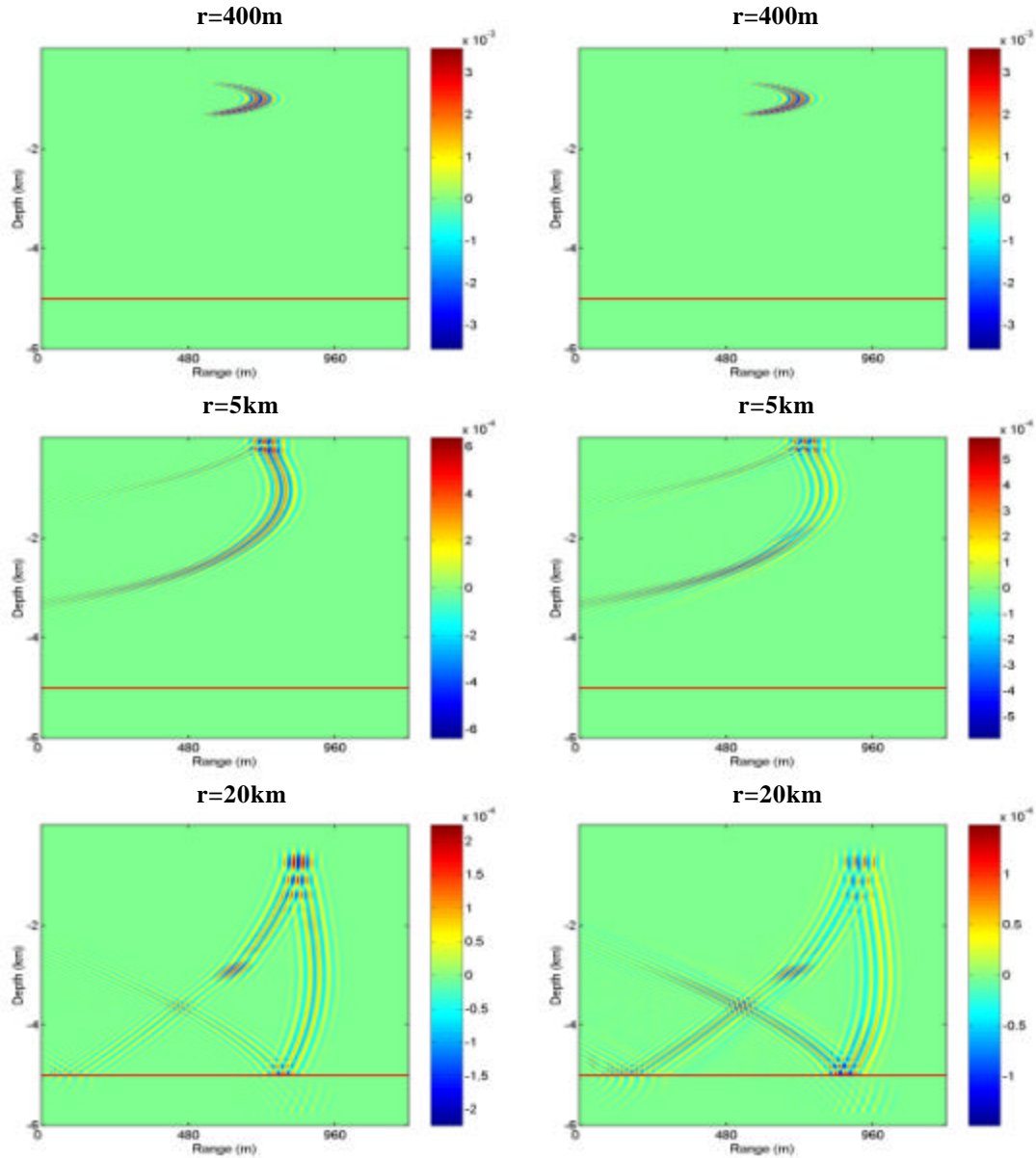


Figure 6: Snapshots at different ranges (400 m, 5 km, 20 km) for both linear (left) and nonlinear (right) deep water cases with a single narrow band source centered at 50 Hz with a source overdensity $R_m = 3.5 \cdot 10^{-3}$.

With the same source, Figures 6 and 7 show respectively snapshots and time series, at 1 km corresponding to the source depth, for linear and nonlinear cases within a 5-km deep water waveguide. The sound speed in the sediment layer is 1600 m/s and the absorption coefficient is 0.5 dB/ λ (Fig. 1.c.). The results show a weak interaction with the sediments and a localization of the energy at a depth where the sound speed is minimum. In the nonlinear case, there is more energy in the tail of the signal and the pulse duration is longer than in the linear case (Fig. 6). For both cases the signal that appears, at about 4 km and 0.8 s in Figure 7, is due to the bottom bounce, and at about 10 km, this signal melts together with the direct arrival.

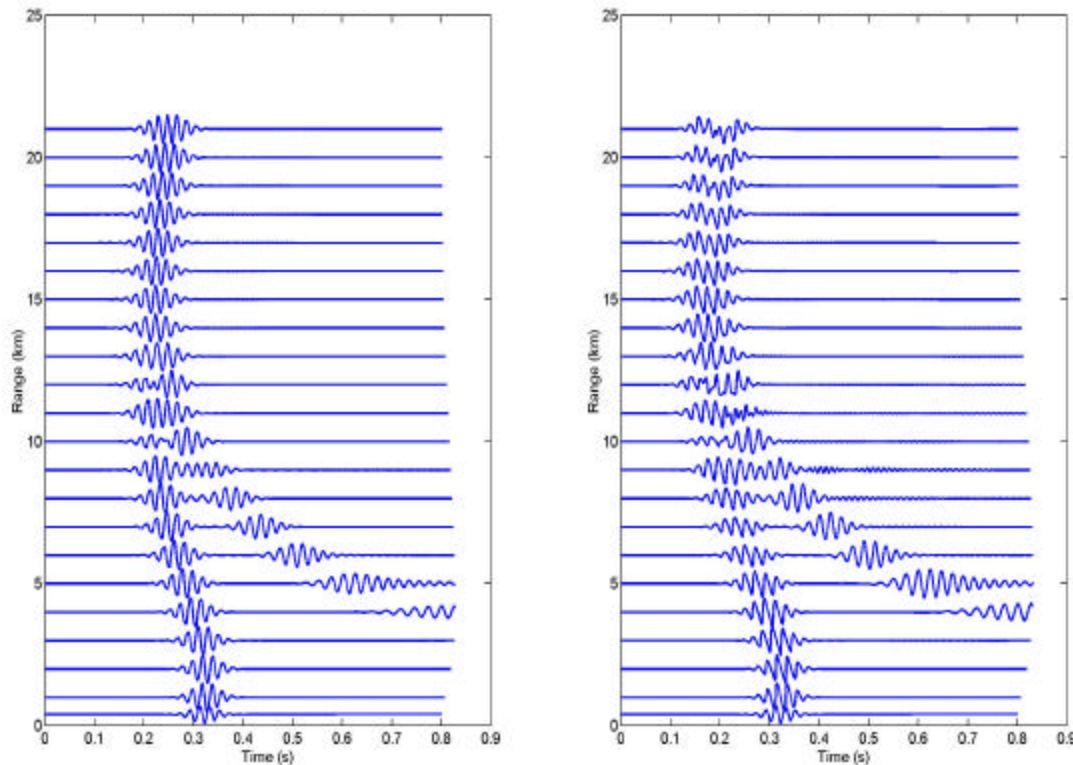


Figure 7: Time series at the source depth (1 km) for linear (left) and nonlinear (right) deep water cases with a single narrowband source centered at 50 Hz with a source overdensity $R_{in}=3.5 \cdot 10^{-3}$.

Figures 8 and 9 compare the influence of the source frequency on the normalized depth averaged spectrum for nonlinear propagation at several ranges. For a 50-Hz source (Fig. 6), one can see both difference-frequency wave Δf (DFW) and harmonic generation. Because of the frequency dependence of the viscous absorption, the waves f , $2f$, $3f$ are damped faster than the DFW. Therefore, only the difference frequency Δf exists at long ranges. There is a tendency for the spectrum to shift toward lower frequencies. However, in the shallow water, Figure 9 shows that the waveguide cut-off frequency (3.75 Hz in this example) limits this tendency for very low frequencies: for a 10-Hz source, the parametric difference frequency wave, related to the source broad frequency band, is not generated since it is below the waveguide cut-off frequency. Also, amplitudes for this 10-Hz source show a weaker dissipation than for the 50-Hz source case.

Below the waveguide cut-off frequency, no mode is generated; thus no modal energy propagates. An important difference between shallow and deep water is this waveguide cut-off frequency, which is greater in shallow water ($f_c=3.75$ Hz) and leads consequently to eliminate a part of the DFW energy, whereas, in deep water, the waveguide cut-off frequency is much smaller ($f_c=0.15$ Hz), so DFW generation is less affected in this case.

Long-range propagation

Since the nonlinear effects are important near the source, there is a range for which the amplitude is sufficiently low so that a linear normal mode code can be used to propagate the acoustic field further. The fields from the NPE code at 20 km for both shallow and deep water environments are used as a source in the Kraken normal mode code (Porter, 1991). For the shallow water case, the adiabatic approximation is used to propagate the field to deep water. The snapshots for linear and nonlinear cases are plotted respectively for this shallow-to-deep-water case (Figs. 1[b] and 10) and deep-water case (Fig. 1.c and 11). The results show that the influence of the nonlinear effects on acoustical propagation are greater if the explosion occurs in shallow water. In shallow water, the dispersion of mode-like arrival structures develops more rapidly for a nonlinear case (McDonald, 2002) than when the energy is

linearly propagated. When the energy is linearly propagated in deep water, the snapshots keep this different modal dispersion (Fig. 10). The nonlinear effects will cause the frequency spectrum to be broader and will usually excite a broader spectrum of modes, with more relative energy for the high-order modes. This causes a larger time spread. When the signal propagates to deep water, the signals keep this larger time spread (Fig. 10).

In contrast, for deep-water explosions, the nonlinearities do not generate a modal arrival structure, partly because of little interaction with the bottom. The typical modal arrival structure occurs at long ranges where the signals amplitudes are weak and nonlinear effects will not give a larger time spread (Fig. 11).

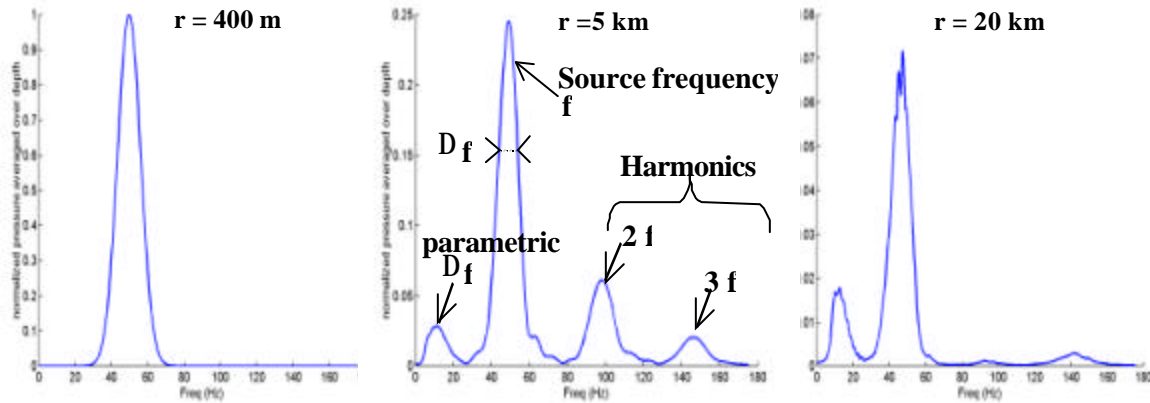


Figure 8: Depth-averaged spectrum at several ranges ($r = 400$ m, 5 km, and 20 km) for a nonlinear shallow water case with a single narrow frequency band source centered at $f = 50$ Hz with a source overdensity $R_m = 3.5 \cdot 10^{-3}$.

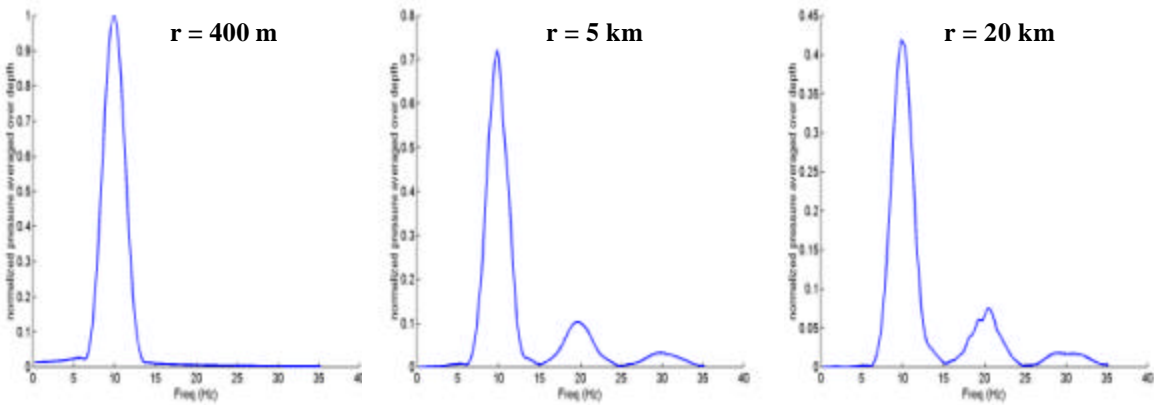


Figure 9: Depth-averaged spectrum at several ranges ($r = 400$ m, 5 km, and 20 km) for a nonlinear shallow water case with a single narrow frequency band source centered at $f = 10$ Hz with a source overdensity $R_m = 3.5 \cdot 10^{-3}$. Due to the waveguide cut-off frequency, 3.75 Hz, there is no generation of the parametric difference frequencies.

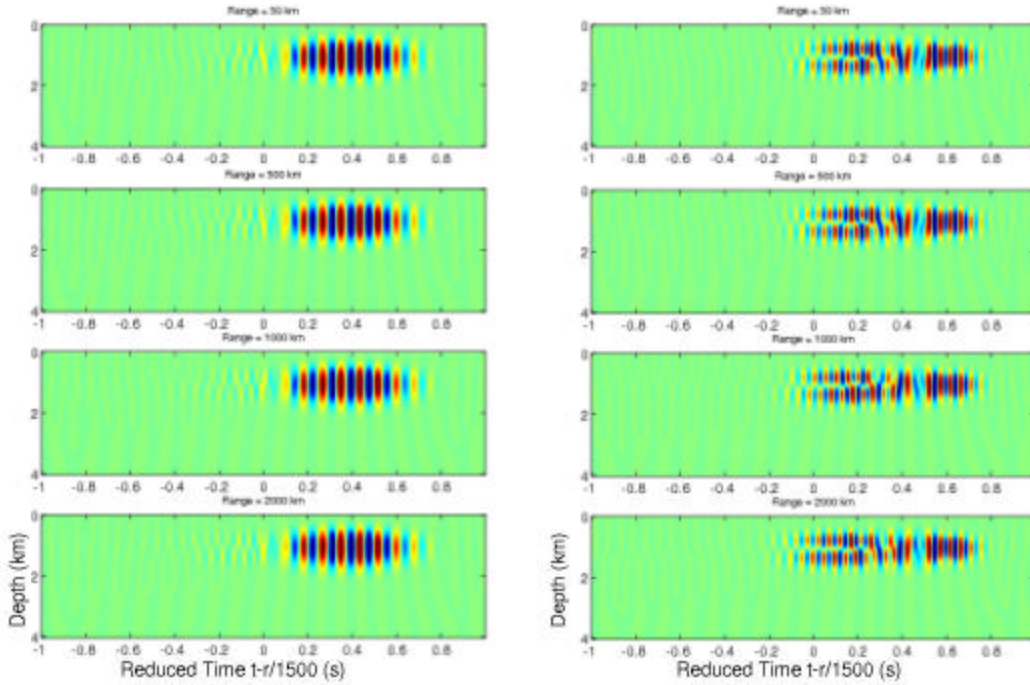


Figure 10: Time series for linear (left) and nonlinear (right) shallow-to-deep-water cases ($f = 10$ Hz, $r = 50$ km, 500 km, 1000 km, 2000 km).

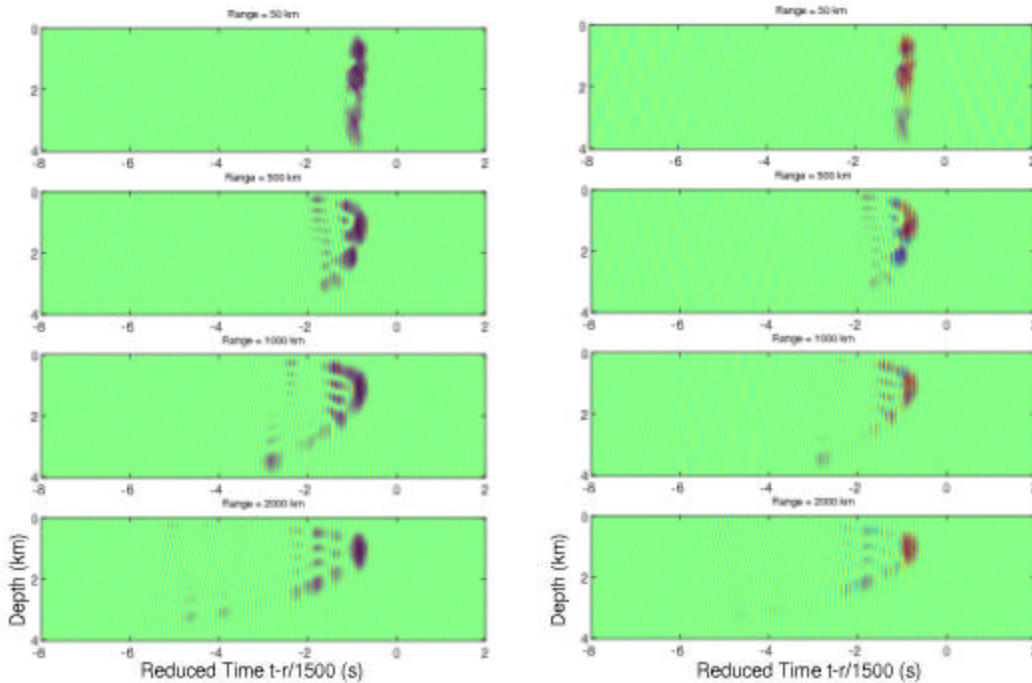


Figure 11: Time series for linear (left) and nonlinear (right) deep water cases ($f = 10$ Hz, $r = 50$ km, 500 km, 1000 km, 2000 km).

CONCLUSION AND RECOMMENDATIONS

Results presented here suggest that undersea explosions may be characterized by studying their spectral evolution over long-range nonlinear acoustical propagation. In shallow water, the signal interacts with the bottom earlier than in deep water, thus initially lower geometrical spreading is obtained (cylindrical versus geometric spreading). Therefore, signal amplitudes are initially higher than in the deep water case, causing stronger nonlinear effects. The

nonlinear effects will cause the frequency spectrum to be broader and will usually excite a broader spectrum of modes, with more relative energy for the high order modes. In shallow water, low order modes travel faster than high order modes and the nonlinearity will give a larger time spread of the received pulse.

Nonlinear effects on the modal dispersion are much more significant in shallow water than in deep water. Thus, if the event starts in shallow water, it would be easier to discriminate between signals that entered the ocean as linear waves (for example a seismic event or underground explosion) and those that began as nonlinear waves in the ocean itself. In this last case, after long-range propagation, the spectrum is strongly shifted toward low frequencies because of both difference frequency generation and shock dissipation processes. During propagation in shallow waveguide, the lowest frequencies might not be supported by the waveguide, due to modal cut-off. Thus, the low-frequency parametric wave might not always be observed.

ACKNOWLEDGMENTS

The authors are grateful to Philippe Roux for his support and helpful discussions.

REFERENCES

- Ambrosiano J. J., D. Plante, B.E. McDonald, W.A. Kuperman (1990), Nonlinear propagation in an ocean acoustic waveguide, *J. Acoust. Soc. Amer.*, **87**, 1473-1481.
- Barriere Ch. (2002), Effet de la diffraction sur l'interaction parametrique d'ondes acoustiques. Application a la mesure de parametres de non linearite et de champs acoustiques, PhD dissertation, Universite Denis Diderot-Paris 7.
- D' Spain G. L., W.A. Kuperman, J. Orcutt J, and M. Hedlin (2000), Long Range Localization of impulsive sources in the Atmosphere and Ocean from Focus Regions in Single Element Spectrograms, Proc. of 22nd Annual Seismic Research Symposium.
- Gerstoft P. (1999), Assessment of hydroacoustic processing in the CTBT release one monitoring software, Comprehensive Nuclear-Test-Ban-Treaty Organisation, Vienna, Austria.
- Hamilton M. F. and D.T. Blackstock (1998), *Nonlinear acoustics*, Academic Press.
- Kuperman W. A., B.E. McDonald, and G.L. D' Spain (2001), Arrival structure of long-range propagation excited by a finite amplitude source, Proc. of 23rd Annual Seismic Research Symposium.
- Marchal J. (2002), Acoustique non lineaire: contribution theorique et experimentale a l'etude de l'emission parametrique, PhD dissertation, Universite Pierre et Marie Curie-Paris 6.
- Lee Y. -S. and M.F. Hamilton (1995), Time-domain modeling of pulsed finite-amplitude sound beams, *J. Acoust. Soc. Amer.*, **97**, 906-917.
- McDonald B. E. and W.A. Kuperman (1987), Time domain formulation for pulse propagation including nonlinear behavior at a caustic, *J. Acoust. Soc. Amer.*, **81**, 1406-1417.
- McDonald B. E. (2000), High-angle formulation for the nonlinear progressive-wave equation model, *Wave Motion*, **31**, 165-171.
- McDonald B. E. (2002), Nonlinear effects in source localization, in *Ocean Acoustic Interference Phenomena*, eds. W. A. Kuperman and G. L. D'Spain, AIP Press, NY.
- Porter M. (1991), The Kraken normal mode program, SACLANTCEN SM—245.

AN ADVANCED CONCEPT DEMONSTRATION FOR MONITORING THE INDIAN OCEAN

Jeffrey A. Hanson, Roger Bowman, and Gregory Beall

Science Applications International Corporation

Sponsored by Defense Threat Reduction Agency

Contract No. DTRA01-99-C-0025

ABSTRACT

The Center for Monitoring Research (CMR) has embarked on an advanced concept demonstration (ACD) focused on improving nuclear explosion monitoring in the vicinity of the Indian Ocean. Central to the demonstration are the new hydrophone assets. These are the International Monitoring System's (IMS) hydrophone stations at Diego Garcia (part of the British Indian Ocean Territories) and Cape Leeuwin, Australia. The third Indian Ocean hydrophone station at Crozet Island will be simulated for purposes of this work because it is not currently operational.

The primary goal of the ACD is to demonstrate new approaches that improve the capability to detect, locate and characterize in-water sources in the context of an operational monitoring system. The advances that are being implemented include optimizing signal processing for the new tri-partite hydrophone array stations, improving acoustic propagation and attenuation models, making use of basin reflections, and creating visualization tools for more effective analysis.

A supporting effort for the ACD is to create realistic synthetic data for events of interest. Demonstrating the system improvement requires data representative of realistic scenarios that test the monitoring objectives. Large explosions are the primary events of interest. However there are no examples of large explosions since the new stations became operational. The few examples that are recorded in other ocean basins are of limited use because of the difference in instrumentation and basin characteristics, and therefore we require synthetic data. However, synthetics often contain many of the same assumptions that were used to create the operational system. The results from synthetics must be validated against real data to the extent possible. Thus, compilation of real data sets that can validate the synthetics and characterize the day-to-day system operation is also a major portion of the ACD.

OBJECTIVE

The CMR in Arlington, Virginia, has begun developing a series of Advanced Concept Demonstrations (ACD) that are designed to improve current operational nuclear-explosion monitoring systems by incorporating state-of-the-art research in a prototype operational system. The demonstrations concentrate on different regions that include test sites and geographic regions of interest. The demonstration described here focuses on the Indian Ocean, which is of particular interest because it is the first ocean basin covered by the new International Monitoring System's (IMS) hydrophone stations. The demonstration is currently under development with completion anticipated by the end of 2002.

The overall objective for the Indian Ocean ACD is to demonstrate new approaches that improve capability for monitoring in-water and sub-ocean sources in the Indian Ocean Basin with an emphasis on exploiting data from the new hydroacoustic stations. Our specific goal is to show improvement in detection, location, and characterization of events in the IOB compared to the current Nuclear Test Detection System (NTDS) at the CMR. The ACD will be assessed relative to the current baseline system. Some of the ACD components will provide new capability that does not exist in the current system while other parts will improve various aspects of the system's ability in detecting, locating, or characterizing an event.

RESEARCH ACCOMPLISHED

Hydrophone Array Processing

There are currently two new hydrophone stations operating in the Indian Ocean with a third scheduled to come on-line in spring of 2003. The operational systems are located off Cape Leeuwin, Australia, (HA01) and the island of Diego Garcia, British Indian Ocean Territories (HA08). The third station is located at Crozet Island in the southwest of the basin. These stations provide significantly higher quality data than the initial IMS hydrophone stations (e.g., Wake and Ascension Island).

The new stations consist of multiple hydrophones arranged as triads with inter-element spacing on the order of 2 km. The Cape Leeuwin station (HA01) is a single triad off the west coast of Australia. The Diego Garcia station (HA08) has two triads located northwest and southeast of the island to avoid blockage from the Chagos Archipelago. The station at Crozet (HA04) will also have two triads to the north and south of the island.



Figure 1. IMS Hydroacoustic Station Locations. Each triangle represents a triad of hydrophones. The current operational instruments are the two triads at Diego Garcia and the single triad at Cape Leeuwin. The two triads at Crozet are scheduled to come online in spring, 2003.

One of the efforts in this ACD is the implementation of coherent array processing of the triads in order to increase detection sensitivity. Current hydroacoustic station processing runs a detector on each individual hydrophone. Detections within a triad are then grouped, and azimuths are estimated by cross-correlating the waveforms. Although this method does produce accurate azimuths, it is not taking advantage of the possible signal gain using the triads as arrays. A 5-dB gain in the signal-to-noise ratio (SNR) is theoretically possible.

On initial examination, the triads appear inadequate to use as typical hydroacoustic arrays. The element spacing (~2000 m) is large relative to the typical signal wavelength (~200 m at 8 Hz), which results in severe spatial aliasing for narrow band signals (Figure 2). However, a signal with sufficient bandwidth removes much of degeneracy and allows the triads to be processed as coherent arrays (Figure 3).

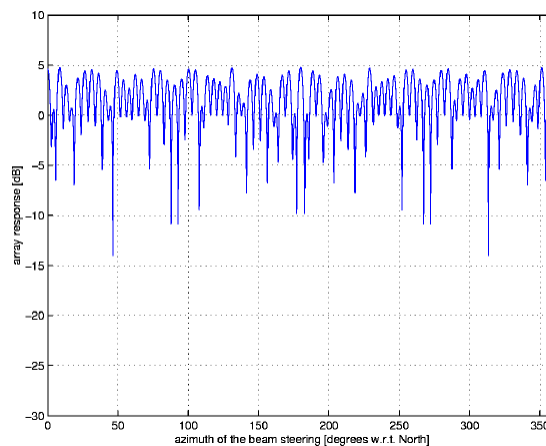


Figure 2 Array Beam Response for an Idealized Hydrophone Triad. The response is calculated for a monochromatic plane wave arriving from the south (8 Hz). The triad element spacing is much larger than the wavelength, which leads to the severe spatial aliasing.

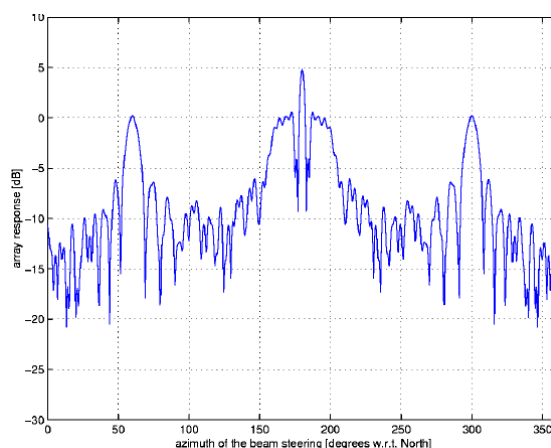


Figure 3 Array Beam Response for an Idealized Hydrophone Triad Using a Broadband signal. The response is calculated for a plane wave arriving from the south with energy between 6 to 10 Hz. The bandwidth of the signal reduces the side-lobes and produces a unique peak corresponding to the actual arrival azimuth.

The standard NTDS detection processing for coherent arrays uses what are known as beam recipes. The beam recipes specify a set of filter bands and steering angles that are used to compute beams. Each beam is fed into a signal detector that triggers on a preset SNR threshold. A suite of frequency bands is used because the band with highest SNR is not known a priori. The azimuthal spacing of the beam recipes depends on the width of the main lobe in the array's response function, which in turn depends on the center frequency of the signal. Table 1 specifies the number of beam recipes necessary for each frequency band necessary for coherent array detection processing. The total number of beams is 2690. This is significantly more than used for a typical seismic array that have on the order of a few hundred beams. This increase results in a considerably greater computational burden than current NTDS processing. However, initial results indicate that the system is capable of processing the typical hydroacoustic triad data.

Table 1. Predicted Main Lobe Width with Required Number of Beam Recipes

Frequency Band	Center Frequency (Hz)	Azimuth Main-Lobe Width (deg)	Number of Beam Recipes
1 - 2	1.5	19.02	20
1.5 - 3	2.25	12.66	30
2 - 4	3	9.49	40
3 - 6	4.5	6.32	60
4 - 8	6	4.74	80
6 - 12	9	3.16	120
8 - 16	12	2.37	180
12 - 24	18	1.58	240
16 - 32	24	1.18	360
24 - 48	36	0.79	480
32 - 64	48	0.59	720
1 - 48	24.5	1.16	360
Total			2690

Capability Assessment

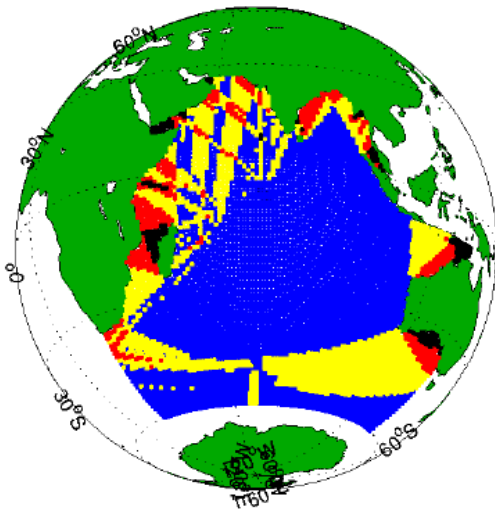
One technique for measuring the improvement of detecting and locating in-water events is to regionalize the basin into areas where some given criteria can or cannot be achieved. The variation in size of these areas between the current and ACD systems provides an intuitive quantification of the system's improvement. This analysis is in large part a predictive one because observational data do not exist to characterize the entire basin. These predictions will be validated using the available data.

We are dividing the basin into four main regions based on the ability to satisfy a set of criteria for an in-water explosion (an example of criteria set would be a detection threshold of $m_b=3.5$ and 90% error ellipse area $< 5000 \text{ km}^2$). The categories are:

1. Criteria achieved using the seismic network alone.
2. Criteria achieved using the hydrophone network alone.
3. Criteria achieved using some combination of the seismic and hydrophone networks together.
4. Criteria not achieved with the specified networks.

Because this particular ACD does not focus on enhancing seismic-only processing, the region covered by (1) should not change between the current and ACD systems and thus can be ignored for our purposes. It is useful to delineate area (2) because it should be relatively invariant to changes in a magnitude threshold criterion. This is due to the much lower detection threshold of the hydroacoustic network than the seismic network. The category (2) area established using an $m_b=3.5$ threshold is nearly equivalent to the area found using $m_b=2.5$ or even $m_b=1.5$. It is the areas covered in (3) and (4) that we anticipate exhibiting the largest improvements (Figure 4). These areas also cover most of the ocean margins and are more relevant to security issues.

Current Hydro Detection Capability



Current Location Capability, $m_b=3.5$

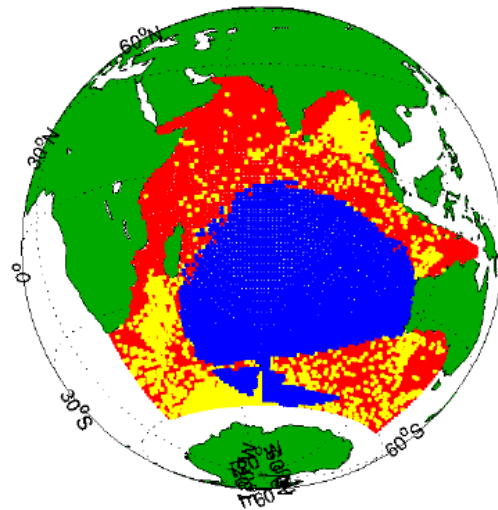


Figure 4. Example of Predicted Detection and Location Capability of the Current System. The left figure depicts hydroacoustic detection capability. The colors correspond to the number of detecting stations: 0-black, 1-red, 2-yellow, and 3-blue. The right figure depicts location capability using the criteria described in the text. The categorized regions are represented as different colors. Blue depicts the area that achieves the criteria using only the hydroacoustic network (category 2). Yellow depicts the area that achieves the criteria using both the hydroacoustic and the seismic network (category 3). Red depicts the area that does not meet the criteria (area 4). In this example the seismic-only processing (category 1) covers a minute region because of the low magnitude threshold. The ACD system is expected to reduce the area in red by improving measurements and models and by including new signal types such as reflected hydroacoustic signals.

Data Sets

Four sets of data will be used during this effort:

- The Calibration Data Set (CDS),
- The Fixed Data Set (FDS),
- Synthetic Data
- Live Data

The CDS will be a compilation of waveform data recorded during the calibration experiment conducted by Lawrence Livermore National Laboratory and Scripps Institution of Oceanography (Blackman *et al.*, 2002) and data recorded during a seismic refraction experiment on the Southeast Indian Ridge (Cochran *et al.*, 2002). These data contain the only real ground truth that we have for the new hydrophone stations. The sources that were used for both the calibration experiment and the refraction experiment were relatively small. The signals from these experiments will be primarily useful in validating travel-time modeling errors and possibly azimuthal measurement errors.

The FDS will provide a fixed set of hydroacoustic and seismic waveform data that can be used to assess and compare results of the different systems. The FDS contains a variety of signals from events throughout the IOB including mid-ocean ridge, trench, and inter-plate earthquakes. The variety of source locations will test the system's robustness and help validate our predicted assessments for monitoring signals of interest. In addition, the hydroacoustic waveform data cover a variety of noise conditions.

Because no large explosions have been recorded at the new hydrophone stations, synthetic waveforms are needed to characterize the system performance for a signal of interest. The synthetic waveforms will be generated by propagating an appropriate source function through range-dependent media extracted from oceanographic databases. The synthetics will be imbedded in typical background noise for the station.

The live data set consists of the waveform data from hydroacoustic and seismic stations that continuously arrive at the CMR. The ACD systems are intended to demonstrate prototype operational systems and as such are designed to process data in near real-time. The data include the hydrophone stations and primary IMS seismic stations.

Reflection Processing

The detection threshold of the hydroacoustic network for an in-water explosion is generally very low due to the efficient coupling of the source and the low attenuation within the ocean's sound channel. However, the geometry of the hydroacoustic network is not always sufficient to adequately constrain the event location. In these cases the current system relies on the seismic network. The ACD system will use hydroacoustic reflections in addition to the direct hydroacoustic and seismic signals to help constrain the location.

Reflections from earthquake-generated signals have been observed and identified at the hydrophone stations (e.g. Harben and Boro, 2001, Hanson, 2001). The azimuth estimates at the triads are generally accurate enough to identify the physical reflectors. Because the travel time between the reflector and the station can be computed, the reflector can be used as a synthetic omni-directional hydroacoustic station. These synthetic stations only provide an arrival time because it is not generally possible to determine the angle at which energy arrived at the reflector.

Hydroacoustic reflections can greatly improve the ability of the network to locate events. The reflections not only improve the geometrical coverage of an event, but they can also observe events where the direct path is completely blocked. Figures 5 and 6 show analysis of an event in the Mozambique Channel, which is one of the few areas in the Indian Ocean that have no direct path to any of the IMS hydrophone stations. This event would need additional information to constrain the location in the way that a regional seismic arrival would, but the reflections provide critical constraints for an event whose magnitude was near the seismic threshold.

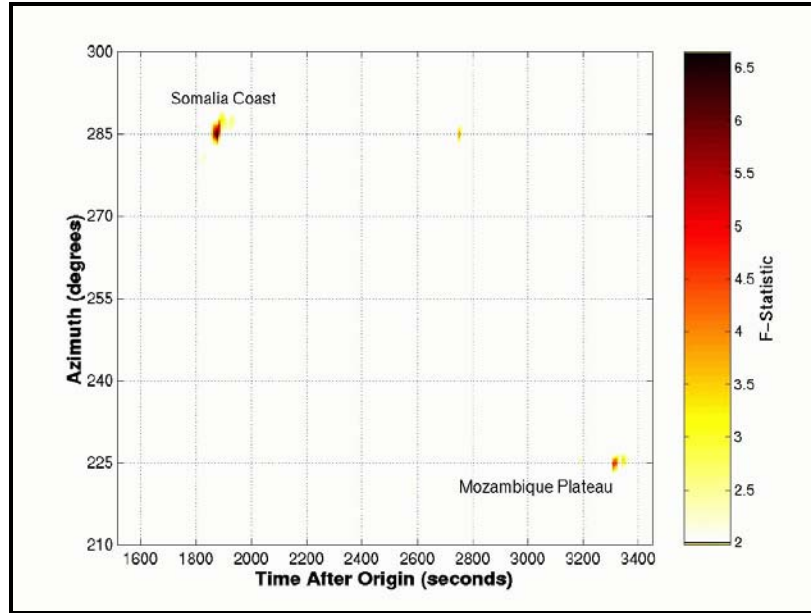


Figure 5. Time-bearing plot showing two reflections at the northern Diego Garcia triad for the event shown in Figure 6. The reflections are discrete arrivals that can be used to help constrain the event location. The azimuth estimates allow the physical reflector to be identified.

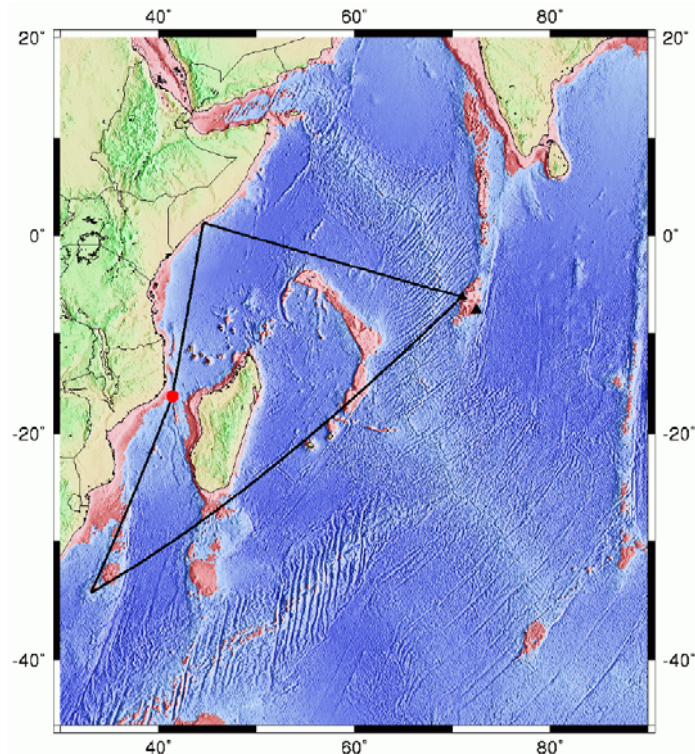


Figure 6. Example of reflections from a blocked event. The event occurred on April 2, 2002. The earthquake's epicenter is shown as the red dot in the Mozambique Channel. The black lines show the inferred path for the two reflectors seen in Figure 5. Bathymetry shallower than 2000 m is shaded pink to help identify potential reflectors. It is signals like these that will help improve the system's capabilities.

Visualization Tools

A large portion of the effort will be to provide an analyst with a set of tools that will enhance an analyst's ability to detect, locate and characterize an event. Some of these tools are standard applications that have been used by researchers for years, but have not been integrated into the NTDS operational environment for day-to-day operations. Other tools are implementations of novel methods that are relevant to the hydroacoustic monitoring problem. These components include a spectrogram tool, a cepstrum review tool, a blockage review tool, and an azimuth display tool. Figures 7 and 8 show examples of a spectrogram tool and a cepstrum review tool. Figure 5 shows an example of what the azimuth display tool will provide.

The spectrogram allows analysts to quickly identify signals and choose the frequency band that maximizes SNR. Small signals are observable that could be overlooked in a time series representation. The cepstrum tool allows the analyst to review results from automatic processing that are of critical importance in characterizing and identifying events. It can also be useful in associating arrivals to a single event because the cepstrum is relatively invariant to path effects. The blockage review tool will aid the analyst in associating arrivals and to look for evidence that contradicts a given location (such as no signal at an unblocked receiver). The azimuth display tool provides a detailed image of the coherent energy arriving at a hydrophone station. This is important for obtaining the best azimuth estimate for direct arrivals and for identifying potential reflections. All of these tools are intended for use in an operational system. They will be integrated into the analyst's environment to support routine analysis of events that are of potentially interest.

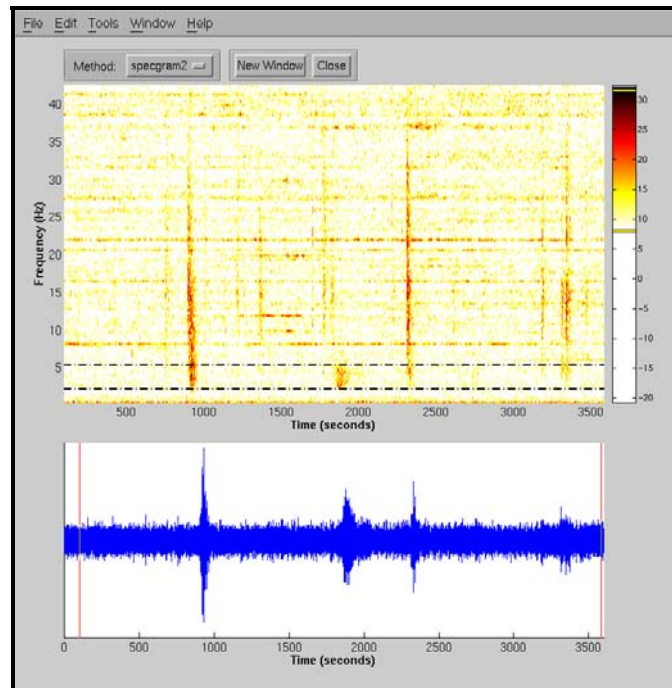


Figure 7. Example of a Spectrogram Tool. The spectrogram is the favored tool for analyzing hydroacoustic signals. The ACD is implementing an integrated spectrogram tool for analyst review. This particular spectrogram allows the analyst to simultaneously view the waveform and spectrogram, interactively choose filter bands, and adjust the color scale. The tool uses a sophisticated algorithm to enhance transient signals, which are the signals of greatest interest for test monitoring.

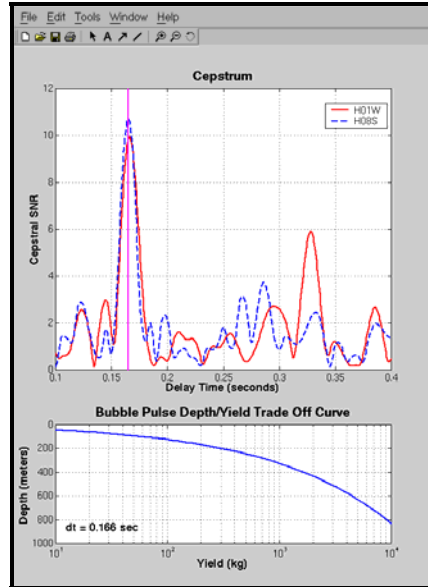


Figure 8. Example of a Cepstral Analysis Tool. The ability to review and modify cepstral results will be a new feature of this ACD. This tool allows the analyst to confirm the very important event characterization measurement. The estimated delay time (the first peak in the cepstrum) determines a depth/yield trade-off curve that will be used in determining a hydroacoustic magnitude. The automatic system picks the maximum peak that sometimes corresponds to the second bubble pulse and needs to be corrected by the analyst. The cepstra can also provide strong evidence for phase association as shown in this example with two signals measured at widely separated hydrophones that have nearly identical cepstral peaks.

Hydroacoustic Magnitudes

We are implementing a method for estimating a hydroacoustic station magnitude for in-water explosions. The energy measures extracted during processing (peak energy and total energy) provide some constraint on the magnitude of a particular event. However, it is difficult to directly determine quantities such as yield from these measures. The energy loss (transmission loss) due to propagation through the oceanic waveguide must be included in a yield determination.

Once a location for an event has been estimated, the transmission loss (TL) between the event location and a given hydroacoustic station can be calculated. TL is calculated for a number of potential source depths and across a wide frequency band. A standard model is used to calculate a set of candidate energy spectra as a function of charge weight and detonation depth consistent with the measured bubble pulse period. TL estimates and the source spectra are combined to predict a set of candidate energy spectra at the hydrophone station. The yield corresponding to the candidate spectra that best-matches the measured spectrum is used as the hydroacoustic magnitude estimate. This also provides an estimate of the source depth. An important feature of this approach is that it exploits the shape of the energy spectrum across the available frequency band. This shape provides critical information about the charge weight and detonation depth. Both the transmission loss and source spectra vary with frequency depending upon (among other factors) the source depth assumed.

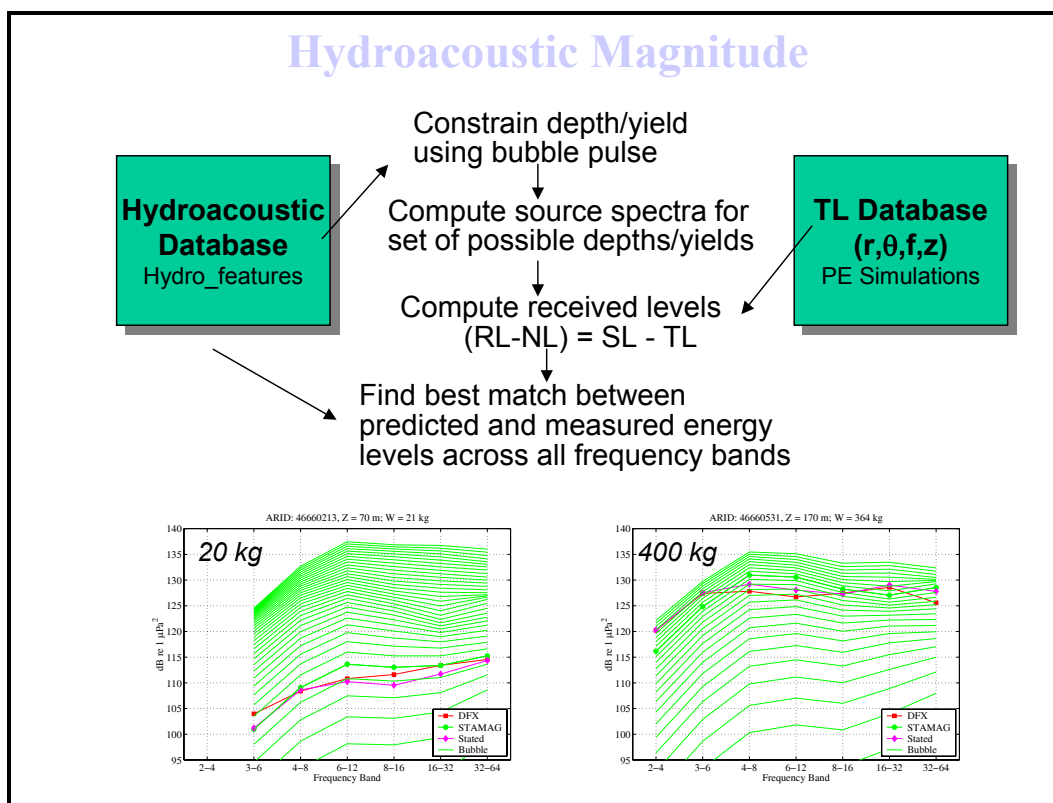


Figure 9. Estimation of hydroacoustic magnitudes. The received signal levels are matched to simulations based on source path and constrained using the bubble pulse depth/yield trade-off. The two examples use the actual measurements from explosions with nominal yields of 20-kg and 400-kg TNT equivalent.

Results using data from a well-documented seismic refraction survey show that accurate estimates of source yield and detonation depth are possible. This suggests that the measured spectral shapes and levels are sufficiently resolved in frequency, and that they can be predicted with sufficient fidelity using standard acoustic propagation codes and environmental databases.

CONCLUSIONS AND RECOMMENDATIONS

The new IMS hydrophone stations in the Indian Ocean provide a great opportunity to improve our hydroacoustic processing for detecting nuclear explosions in the region. This project will demonstrate enhancements in detection, localization and characterization of events occurring in the Indian Ocean Basin.

The Indian Ocean Advanced Concept Demonstration will improve detection by using coherent array processing and by providing analysts with visualization tools. The system's location capabilities increase by improving azimuth estimates, improving travel-time models, and incorporating hydroacoustic reflections into the location algorithm. The analyst will have significantly better resources to associate signals together including the spectrogram tool, the cepstral review tool, and the blockage review tool. New characterization abilities include the cepstral review tool and hydroacoustic magnitude estimation.

The data sets being compiled for the demonstration provide a unique resource that will be useful not only for evaluation of this project, but also for evaluating future enhancements to the system. There continues to be a need for definitive calibration data. This is especially true in regards to evaluating locations using reflected phases.

ACKNOWLEDGEMENTS

We would like to thank G. Eli Baker, Donna Blackman, Paul Dysart, Mariana Eneva, Charles N. Katz, and Brian Sperry for their contributions to this project.

REFERENCES

- Blackman, D., C. de Groot-Hedlin, P. Harben, A. Sauter, and J. Orcutt (2002, submitted), Scattering and Propagation of Controlled Acoustic Signals Throughout the Indian Ocean Basin, *J. Acoust. Soc. Amer.*
- Hanson, J.A. (2001), Initial Observations from the BIOT Hydroacoustic Station, *Proceedings from the CTBTO Hydroacoustic Workshop, October 8-11, 2001*.
- Hanson, J.A., R. Le Bras, P. Dysart, D. Brumbaugh, A. Gault, and J. Guern (2001), Operational Processing of Hydroacoustics at the Prototype International Data Center, *Pure Appl. Geophys.*, **158**, 425-456.
- Harben, P.E. and C.O. Boro (2001), Implosion Source Development and Diego Garcia Reflections, *Proceedings 23rd Seismic Research Review*, 23-31.
- Pulli, J.J. and Z.M. Upton (2001), Hydroacoustic Blockage at Diego Garcia: Models and Observations, *Proceedings 23rd Seismic Research Review*, 45-54.
- Cochran, J.R. (2002), Cruise Report R/V Maurice Ewing, December 7, 2001 – January 25, 2002, Fremantle, Australia to Hobart, Australia, EW0114.

**ACOUSTIC SOURCES FOR BLOCKAGE CALIBRATION OF OCEAN BASINS:
RESULTS FROM THE OCTOBER 2001 INDIAN OCEAN CRUISE**

Philip E. Harben,¹ Catherine de Groot-Hedlin,² and Donna Blackman²

Lawrence Livermore National Laboratory¹ and Scripps Institution of Oceanography²

Sponsored by Office of Nonproliferation Research and Engineering
Office of Defense Nuclear Nonproliferation
National Nuclear Security Administration

Contract No. W-7405-ENG-48¹ and DE-FC03-01SF22356²

ABSTRACT

Blockage and transmission loss calibration of hydroacoustic stations for explosion monitoring is important for assessing monitoring capability from new and existing stations. Unlike acoustic travel time, generally predicted with good accuracy by models, blockage and transmission loss predictions along many ray paths are poor. In large part, this is due to the relative coarseness of the global bathymetry databases for the acoustic frequency range of monitoring interest (1-100 Hz). When higher resolution bathymetry databases are integrated into models, blockage prediction accuracy improves; however, such high-resolution bathymetry databases are not available in large regions, such as the Indian Ocean, due to sparse coverage. A data-driven approach to the blockage and transmission loss prediction problem is an approach that sidesteps the bathymetry database problem as well as other difficulties such as modeling diffraction, higher modes, and providing predictions as a function of frequency. The data-driven approach requires a large number of ground truth events recorded at a specific station to calibrate it and allow prediction of blockage and transmission loss from a hypothetical source. Earthquakes can provide most of the calibration events but, with the exception of submarine volcanoes, there is no significant energy in the T-phase above about 15 Hz. To calibrate stations at higher frequencies, an artificial source is necessary. The purpose of the 2001 Indian Ocean cruise was to test three such sources at ocean basin scale.

Three sources were tested: an airgun array, a spherical implosion system, and a cylindrical implosion system. These sources were fired at numerous locations along a great circle ship-track between the Seychelles and Perth, Australia, and recorded at the Diego Garcia and Cape Leeuwin hydroacoustic stations. The airgun system was fired over shallow and/or sloping bathymetry along the track as much as possible to maximize coupling into the sound channel via bottom scattering. Although airgun signals were detected at Diego Garcia and at Cape Leeuwin, detections were not seen in several cases because the coupling was dependent on the complex process of bottom scattering into the SOFAR channel. The spherical implosion system was fired in two different configurations: 1-sphere and 5-sphere. The 22-liter single-sphere implosions were reliably detected at Diego Garcia for ranges from 800 km to 1200 km when fired at sound channel depths of 680 m. The 5-sphere shots were a cluster of 22-l spheres fired at 680 m. Both 5-sphere tests were reliably recorded at both Diego Garcia (4000- to 4500-km ranges) and Cape Leeuwin (1500- to 2000-km range). The sphere implosions produced useful signal from 40 Hz through 100 Hz. The sphere implosion systems also proved to be highly repeatable, especially the 1-sphere system. Tests with the cylindrical implosion system produced signal level too low to be detected at the International Monitoring System (IMS) hydroacoustic stations. A future cruise will test two additional sources: small explosives and a large continuous wave source previously employed in ATOC (Acoustic Thermometry of the Oceans Climate) experiments.

OBJECTIVE

The overall objective of this research is to assemble a database that provides accurate blockage prediction from any hypothetical oceanic source location to all hydroacoustic monitoring stations of interest. We know from experience that a model-based approach to this problem is not always accurate. The BBN Inc. code — HydroCAM — continues to be used at the National Data Center for model-based prediction of acoustic signal blockage. Model-based blockage predictions suffer, to first order, from the generally coarse bathymetry data available for the world's oceans. Less important, but significant, sources of model error are: ignoring scattering and diffraction, using only mode-1 propagation, and an inability to conveniently determine blockage as a function of source frequency.

The approach to improving blockage prediction in the world's oceans is to improve model capabilities by improving the resolution of the bathymetry databases and to assemble a database of ground truth events that define the blockage at any particular station. Emulating the regional seismic travel-time correction methodology, hydroacoustic ground truth data will trump any model prediction for locations close to where ground truth is available. The best prediction will transition to model-based when the location is far from any ground truth data. A critical issue in building the ground truth databases is understanding the suite of sources that will be needed and the limitations of each in providing the desired broadband blockage information. The nature of the source, accuracy of the source location, bandwidth of the source, and strength of the source will define the applicability of the source and the limitations for use in the database. For example, oceanic and near-coast earthquakes that generate large T-phases will certainly be a class of sources that make up a large part of a ground truth blockage prediction database. That they will not be the only class of sources is also clear since the bandwidth is generally limited to 1-15 Hz (much lower than in-water explosions) and their location is difficult to accurately assess (DeGroot-Hedlin, 2001) because the T-phase is not necessarily generated at the earthquake epicenter. We seek to understand the sources we will need in a complete ground truth database. To this end we have completed a cruise that tests three sources: two implosion source systems and an airgun array. The man-made sources sought are those that complement the natural sources: energy in the higher frequencies of the monitoring band (15-100 Hz), accurate locations, and sufficient signal for ocean-basin propagation ranges. The research conducted and presented here has a focus on a sphere implosion system that appears to meet some of the criteria for a man-made source with blockage calibration utility, though other sources remain to be tested.

RESEARCH ACCOMPLISHED

The research accomplished falls under three headings: 1) Blockage Issues, 2) Implosion Source Studies, and 3) Cruise Results. Our discussion of blockage issues will map out some of the difficulties and concerns that must be at the forefront of any attempt to improve blockage prediction capabilities. The Implosion Source Studies section will document the progress made over the past year in understanding the glass sphere implosion source, its utility, and its limitation in controlled-source calibration. Finally, a summary of the Indian Ocean cruise results will be presented. This cruise took place in October 2001 and tested three different controlled sources for hydroacoustic monitoring station calibration at long ranges.

Blockage Issues

Acoustic blockage prediction in hydroacoustic monitoring has yet to be clearly defined by a concise set of measurements. Model predictions with HydroCAM, for example, can estimate if a particular source-receiver path is blocked or unblocked in accordance with a minimum-ocean-depth criterion along the path. When done for all source paths to a given receiver, a map of blockage for that ocean basin results. The maps generated are very different if the blockage criteria are 800 meters vs. 50 meters, and no single depth criterion produces a best or most accurate map. The reason the models are inadequate is that scattering, diffraction, and reflections - and their frequency dependence - is not accounted for. In addition, the bathymetry databases are inadequate for the acoustic frequencies of interest. Examples of model-predicted blockage at a 50-meter-depth criterion along a particular source-receiver path have been shown to have large amplitude signals from earthquake events that get through, although the coherency of the signals among the tri-partite sensors is significantly degraded (Harben, 2001). Completely blocked source-receiver paths have been shown to have consistent reflected phase arrivals from the same topographic feature.

Blockage prediction is needed to assess which hydroacoustic stations, for a particular source region, can be used in detection, location, and discrimination analysis. That assessment can be made, but it will not always be a simple *yes* or *no* answer for any particular station. A full assessment - which will be backed by a ground truth database - will need to have a set of measurements on direct path attenuation and scattering energy loss, loss in coherency due to scattering, and reflected phases that may be used in subsequent analyses, all with frequency dependence. The question of blockage along a particular path may have an answer like: full blockage at high frequency along the direct path, adequate signal-to-noise ratio (S/N) at low frequencies but with a complete loss of coherency between tripartite sensors (i.e. back azimuth estimation not possible), two consistent reflected phases for large source energy with unblocked paths. Deciding on the most appropriate measures and automating them in a ground truth database used for blockage prediction is an essential next step.

Implosion Source Studies

The development of an imploding glass sphere source has been documented in past reports (see Harben, 2000; Pulli, 2000; and Harben, 2001). Here we present new results from tests and models that improve our understanding of source phenomenology, repeatability, and utility in calibration.

The single-sphere implosion source signal has now been recorded four times under similar conditions, though in widely varying locations. The implosions were conducted at nominally 680-m depth and recorded with a hydrophone hung off the side of the ship, nominally 30-m deep. The recordings are all overplotted in Figure 1. The repeatability of the source is apparent. This is an important result for calibration purposes because it allows for accurate transmission loss and other amplitude-dependent measurements with this source.

We modeled the source (Tipton, 1991) using a C-language Arbitrary Lagrangian-Eulerian code (CALE). Although our results showed qualitative agreement, the modeled peak pressure was half that observed. In consultations with the glass manufacturer, we found that the glass spheres were sealed in a partial vacuum due to the high air temperatures in the vicinity of the molten glass. When we modeled partial vacuums within the glass sphere, we were able to resolve the inconsistency in peak pressure. The modeling predicts the glass sphere internal pressure as 1/6 to 1/8 atmosphere, consistent with air pressures at temperatures of molten glass.

The 5-sphere system had been tested once off the Pacific coast in 2001 at 137-m depth (see Figure 2, left panel). During this test, one of the spheres failed, and the resulting shock wave caused the other spheres to fail. This is evident in the recorded waveform. The beginning of the record has the characteristic signature of a single-sphere implosion -- the sphere that self-failed. The time between the first sphere shock wave and the larger grouping of impulses that follow is controlled not by the acoustic propagation time between spheres but by the collapse time. The implosions at 680 m (Figure 2, right panel) show a markedly different signature that can only be interpreted as a nearly simultaneous implosion of all five spheres due to the smashing cylinder. Apparently, the cracking propagates from sphere to sphere (which are touching) and hence the implosion timing of individual spheres is controlled by the acoustic propagation time. It is also evident that the 5-sphere system is not as repeatable as the 1-sphere source, though the waveforms are similar. This is consistent with expectations if the spheres are failing nearly simultaneously. Such a failure does not have spherical symmetry and will consequently have a complex radiation pattern.

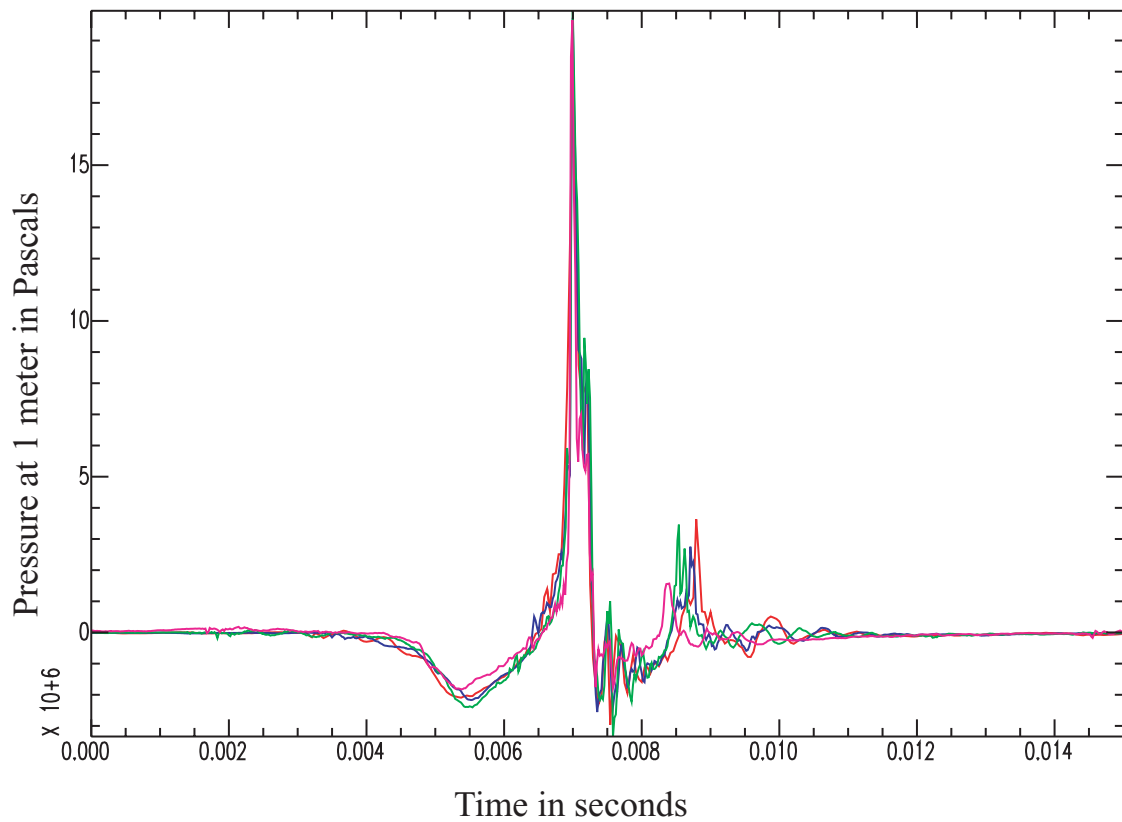


Figure 1. Repeated single-sphere implosions under similar conditions (680-m depth and projected to 1 m from the source). Note the good repeatability, especially for the implosion and main shock.

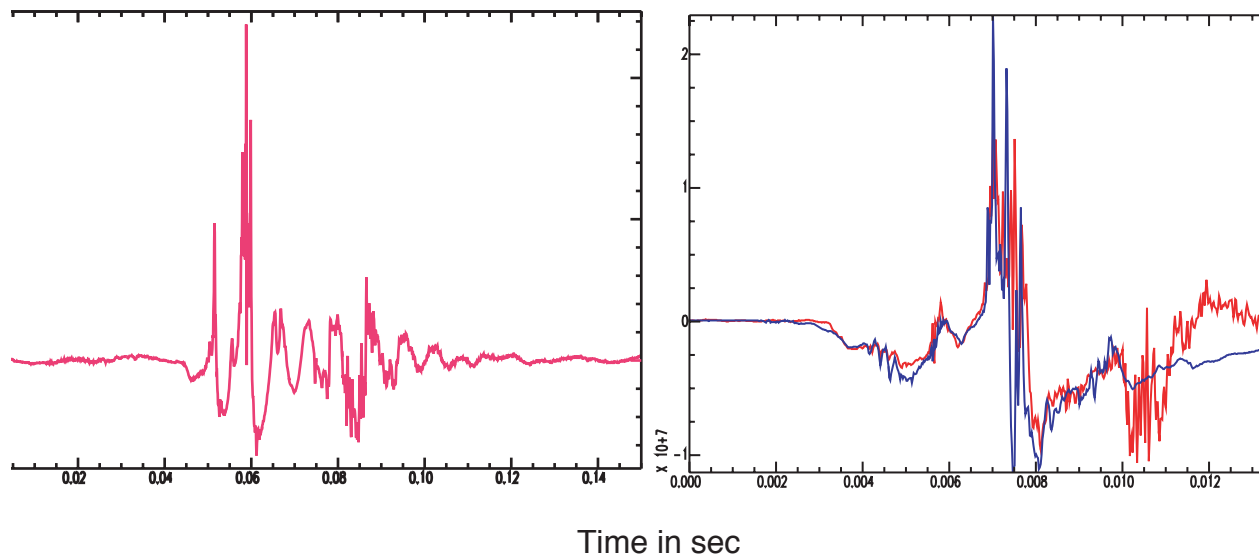


Figure 2. The 5-sphere implosion source waveforms are shown at 137 m (left) and for two tests at 680 m. Both plots are source strength at 1 m in Pascals. The horizontal axis is time in seconds. Note that the 137-m test was initiated by self-failure of a glass sphere. The 680-m tests were initiated properly by the cracking system.

Cruise Results

The purpose of the October 2001 Indian Ocean cruise aboard the Maurice Ewing was to produce acoustic signals at various locations in the Indian Ocean basin so that the nature of sound propagation, and losses, can be documented. One goal was to determine what types of topography are conducive to using large, shallow sources that require that energy be scattered off the seafloor into the SOFAR channel, for basin scale propagation. Another goal was to determine the range at which small, deep imploding sources can be detected at distant receivers. The acoustic sources consist of a large array of airguns, imploding glass spheres, and a triggered imploding cylinder. The receivers are permanently installed hydrophones that are part of the IMS that is overseen by the Comprehensive Nuclear-Test-Ban Treaty Organization. Each hydrophone station consists of three instruments. Two stations are deployed in the vicinity of Diego Garcia, on the east and west slopes of Chagos platform. One station is installed off Cape Leeuwin, southwestern Australia.

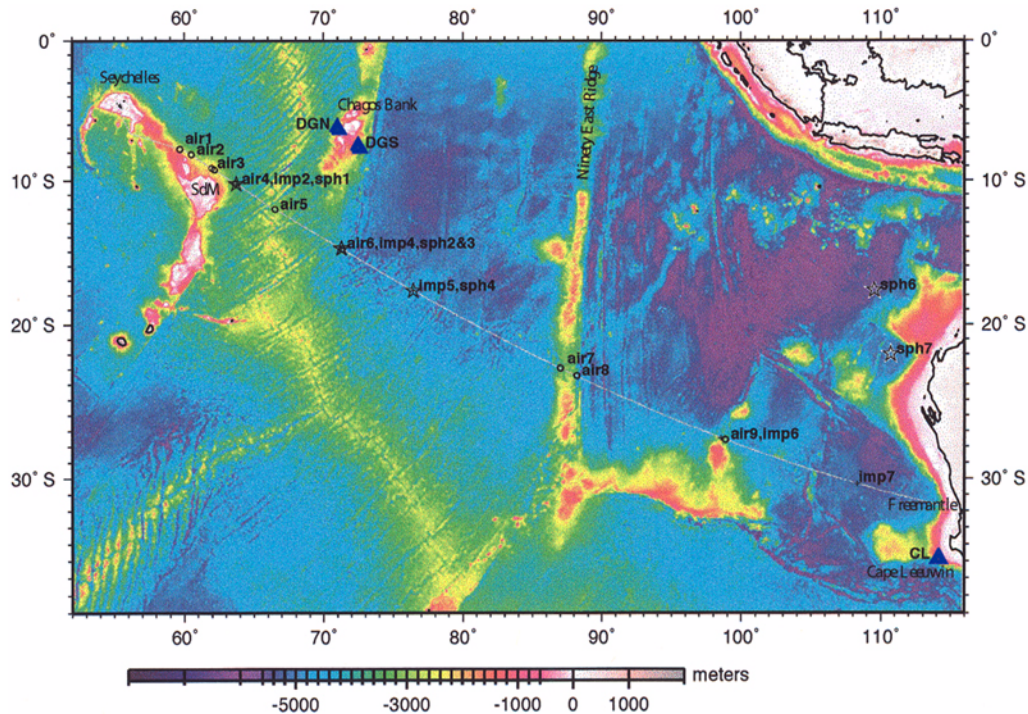


Figure 3. Topographic model of Smith and Sandwell (1997) in the Indian Ocean region is overlain by the 2001 R/V Ewing shiptrack (gray line) and the acoustic source locations for our experiment. IMS hydrophone stations are shown by blue triangles. Circles show where the airgun array shooting (air) was conducted. Stars show glass sphere (sph) implosion stations and 5-sphere implosions are highlighted in white. Crosses are where the MPL/SIO imploding cylinder (imp) was fired. SdM indicates Saya de Mahla bank.

The 'standard' Ewing array of 20 airguns was used. Total volume of the array was 8465 cubic inches. The shot interval was varied from 57 - 173 s. Each shooting period lasted about 30 min. The imploding glass spheres were those described above. Both 1-sphere and 5-sphere systems were tested. The triggered imploding cylinder was a 900-lb. reusable system which operates by using the available hydrostatic pressure at depth to mechanically open an empty 20-l cylinder upon electrical command. Displaced water fills the cylinder, generating an acoustical signal. We recorded all the implosion source waveform on a TEAC RD-145T 16-track using a calibrated (-194dB re 1V/uPa) Ball hydrophone. The hydrophone was deployed from the ship's deck. Shackles were attached to the cable to add weight, but at some stations the cable was not particularly vertical in the water. The sample rate was set to either 24000 or 48000 SPS for the stations.

The cruise track is shown in Figure 3 with the location of the IMS recording stations and the location of each source deployment. The cruise originated in the Seychelles and ended in Freeport, Australia, on the great circle path route between the two. Attempts were made to test airguns in areas of shallow and/or variable seafloor topography. The two 5-sphere shots, shown off the northwest coast of Australia, were conducted for us by researchers on a subsequent cruise.

Airguns: Near source recordings of the airgun array shots indicate very consistent source signatures. Shot durations are on the order of 40 ms, and most of the output energy is in the 6- to 110-Hz band, with peaks at 8 Hz and 14 Hz.

S/N for waveforms recorded at the IMS receivers in the Indian Ocean are shown as a function of frequency in Figure 4. Overall, S/Ns at Diego Garcia south (DGS) and Cape Leeuwin (CL) are much poorer than those at Diego Garcia north (DGN). In part, this is due to higher noise levels at these stations; noise levels at DGS and CL exceed those at DGN by about 6 dB and 12 dB, respectively. As expected, the S/N vary as a function of both source and receiver location mainly due to acoustic blockage. Propagation to DGS was blocked by the Chagos Bank for the first four airgun sites (the first 78 shots). Cape Leeuwin was expected to be blocked from the first site by the Saya de Malha bank and from some of the subsequent five sites by the Ninety East Ridge. Propagation to DGN was blocked by the Chagos Bank for all but the first four sites.

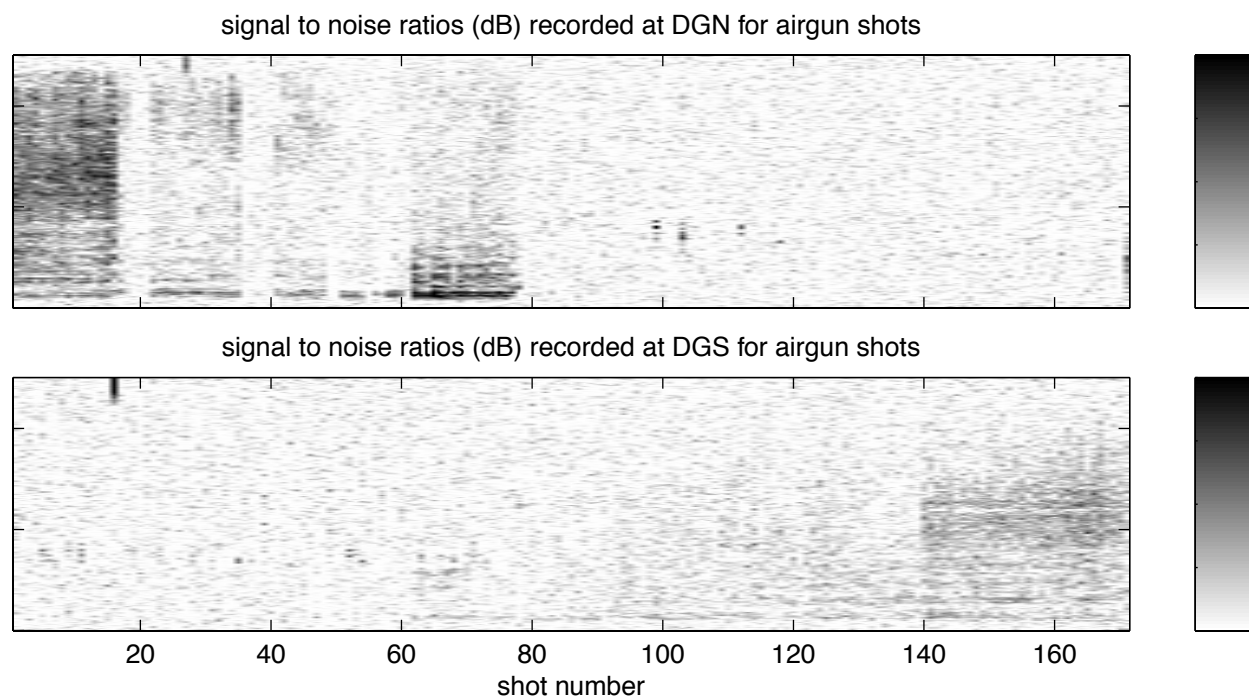


Figure 4. The S/N of the recorded waveforms are displayed in a shaded grey scale as a function of shot number and frequency. Note the recordings were at Diego Garcia north (top) and Diego Garcia south (bottom).

Bathymetry in the source region also affects the observed S/N. Waveforms were detected only when the airgun was shot over ridges, consistent with expectations. Shots 1-16 were located over shallow, sloping seafloor near the Mascarene Plateau just south of the Seychelles. Shots 62-78 were located over the Mid-Indian Ridge. Finally shots 141-178, detected at both DGS and Cape Leeuwin, were near the Ninety East Ridge. Modeling results indicate that energy from these shots couples to the SOFAR channel by downward propagation. However, several other sites were also located in shallow water, but coupled poorly to the SOFAR channel. Modeling is continuing to determine why.

Imploding Spheres: The imploding glass sphere tests showed that a single-glass-sphere system could be detected at unblocked ranges of at least 1200 km. The single-sphere spectra are shown in Figure 5 for three implosions

conducted south of Diego Garcia and recorded at the north Diego Garcia station (left panel) and at the south station (center and right panel). The signals were not observable in the time records unless high pass filtered. We determined a good corner for the high pass to be about 40 Hz. The S/N difference as a function of frequency clearly demonstrates that the imploding sphere will be limited as a calibration source to frequencies above about 40 Hz.

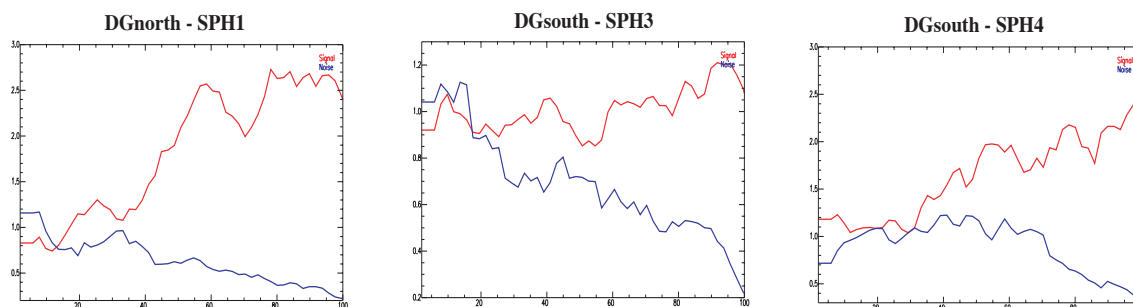


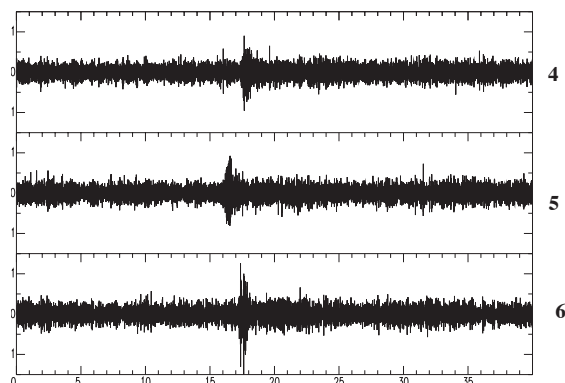
Figure 5. Spectra of the signal and pre-event noise levels for three single-sphere implosions as recorded at the Diego Garcia hydroacoustic monitoring stations. The horizontal scale is frequency in Hz. The vertical scale is normalized to 20-Hz noise levels in each case. The red curves are signal spectra, the blue are pre-event noise. A smoothed average of the three hydrophones at each station is shown.

The 5-sphere implosions were both conducted along the western Australia continental margin with ranges to Diego Garcia of 4168 km and 4397 km and ranges to Cape Leeuwin of 1960 km and 1465 km. The time waveform records are shown in Figure 6. The horizontal scale is in seconds with different time window lengths for the top panels compared to the bottom ones. The waveforms were 4-pole high passed at 40 Hz. Clearly, we are able to record a signal at both stations and hence have demonstrated the possibility of ocean basin scale calibration using the 5-sphere system. As with the single-sphere system, frequency content of the propagating signal is limited to 40 Hz and above. It is clear from the S/N of the recordings that the source strength is woefully inadequate for producing reflections off continental margins and islands that would be detectable. The relatively small amount of dispersion in the signal, after propagation over 4000-km ranges, indicated the implosion sources may be a good source for acoustic travel-time studies.

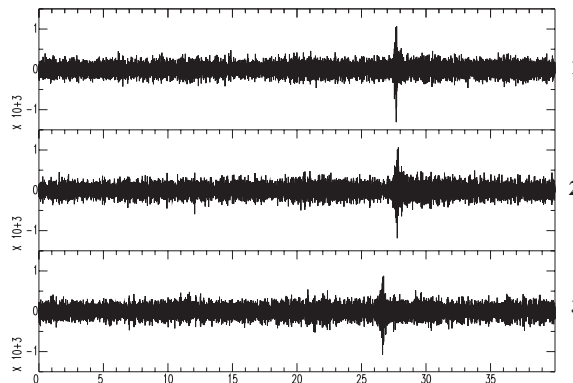
Imploding Cylinders: The cylindrical imploder (Sauter, 1996) was tested at six locations in the Indian Ocean. Although the imploding volume and test depth were similar, the imploding spheres had a peak pressure 20 times larger than the cylindrical imploder. This is due to the optimum convergent geometry of a sphere that gives rise to a larger shock wave. Because of the significantly lower peak pressures, the cylindrical imploder signals were not observed at the Diego Garcia and Cape Leeuwin stations.

5-Sphere Shot SPH5

Diego Garcia

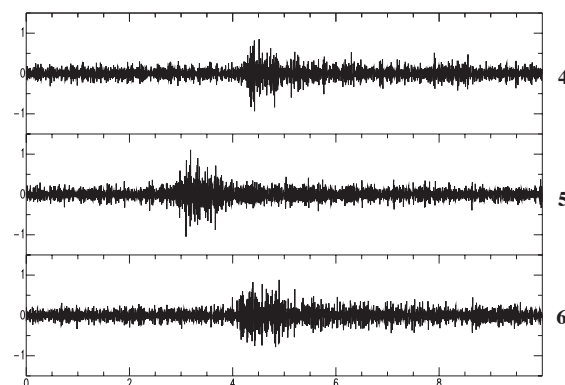


Cape Leeuwin



5-Sphere Shot SPH6

Diego Garcia



Cape Leeuwin

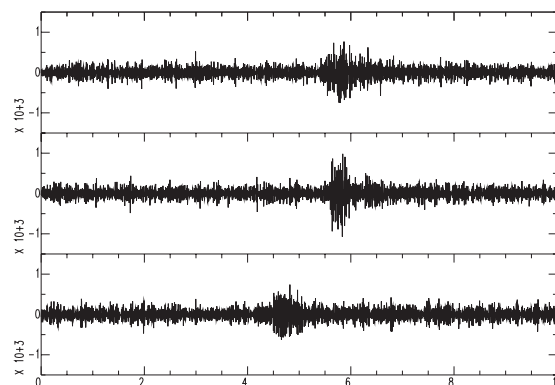


Figure 6. Recordings of the 5-sphere glass sphere implosions are shown with high-pass filtering at 40 Hz. The top two panels show the recording from shot SPH5 at both the Diego Garcia and Cape Leeuwin stations. The bottom panels shows the recordings for shot SPH6.

CONCLUSIONS AND RECOMMENDATIONS

The challenge of providing accurate assessments of acoustic signal blockage in the world's oceans is a large one. Purely model-based approaches fail because of inadequate bathymetric resolution in current databases and simplifying assumptions that make the calculations tractable. Establishing a database of ground-truth events is a strategy that is proving effective in regional travel-time calibration for seismic monitoring. Such an approach holds promise for acoustic signal blockage as well but has distinctly different technical issues that must be resolved. Unlike the solid earth, the acoustic medium is changing on a seasonal basis and hence a particular source-receiver path that is blocked in the summer could be open in the winter. Another issue is low-frequency (1- to 15-Hz) blockage vs. high-frequency blockage (15 to 100 Hz). Most earthquake sources are low frequency and hence can not be used to predict high-frequency blockage. Man-made sources can provide the high-frequency ground truth, and we are beginning to understand the utility of some types of man-made sources in providing ground truth for acoustic blockage prediction.

24th Seismic Research Review – Nuclear Explosion Monitoring: Innovation and Integration

An Indian Ocean cruise conducted in October 2001 tested implosion and airgun sources at source-receiver distances up to 4400 km. The results show that the glass sphere implosion source has utility at long ranges but only in the frequency band of 40-100 Hz. The airgun sources, unfortunately, are not consistently useful because coupling into the SOFAR channel -- hence long-range propagation -- is controlled by bottom scattering, which is highly variable. A follow-on cruise scheduled for May 2003 in the Indian Ocean will test explosives, an ATOC-type fixed-frequency source, and glass sphere implosions. The results of this cruise should complete the ground work needed before planning a systematic man-made source calibration study of an ocean basin.

We have alluded to the importance of reflected acoustic phases for increasing monitoring capability of hydroacoustic networks without any hardware changes (see Pulli, 2000). The practical application of this will require ground-truth calibration of all the major reflectors in an ocean basin. To first order, we believe that earthquake sources will be the best way to accomplish this because the acoustic energy is great enough to generate reflected phases with adequate S/N at the receiver. It will be necessary to understand how the reflected phases are altered at higher frequency. For this, a man-made source will probably be used though we cannot say at this stage if anything other than a large explosion will be capable of generating the acoustic energy needed to provide adequate S/N on the reflected phases.

ACKNOWLEDGEMENTS

We thank Allen Sauter and the Ewing ship crew for helping with all aspects of the cruise logistics and source deployments. We are also grateful to Fiona Sutherland and the shipboard crew for conducting the two 5-sphere deployments during the subsequent cruise leg. We are indebted to the staff of the Air Force Technical Applications Center and the Center for Monitoring Research for supplying the recordings from Diego Garcia and Cape Leeuwin during the time period of the cruise. Thanks to Doug Clarke and Willy Moss for implosion source modeling with the CALE code.

REFERENCES

- de Groot-Hedlin, C.D. and J.A. Orcutt (2001), Excitation of T-phases by Seafloor Scattering, *J. Acoust. Soc. Am.* 109, 1944-54.
- Harben, P.E., C. Boro, L. Dorman, and J. Pulli (2000), Use of Imploding Spheres: An Alternative to Explosives As Acoustic Sources At Mid-Latitude SOFAR Channel Depths, UCRL-ID-139032.
- Harben, P.E. and C. Boro (2001), Diego Garcia Reflections and Implosion Source Development, *Proceedings of 23rd DTRA/NNSA Seismic Research Review*, Jackson Hole, WY.
- Pulli, J.J., Z. Upton, R. Gibson, J. Angell, T. Farrell, and R. Nadel (2000), Characterization of Reflected Arrivals and Implications for Hydroacoustic Test-Ban-Treaty Monitoring, *BBN Tech. Memor.* W1380.
- Pulli J.J. and P.E. Harben (2000), Hydroacoustic Calibration with Imploding Glass Spheres, in *22nd DoD/DOE Seismic Research Proc.*, Vol. III, pp. 65-74.
- Sauter, A., L. Dorman, E. Canuteson (1996), Development of a Seismo/Acoustic Implosive Source, *EOS Trans. AGU*.
- Smith, W.H.F. and D.T. Sandwell (1997), Global Seafloor Topography from Satellite Altimetry and Ship Soundings, *Science* **277**, 1956-1962.
- Tipton, R. (1991), CALE User s Manual, Version 920701, Lawrence Livermore National Laboratory, Livermore, CA.

HYDROACOUSTIC T PHASES FROM LARGE ICEBERGS DRIFTING IN THE ROSS SEA

Emile A. Okal¹, Jacques Talandier², and Olivier Hyvernaud²

Northwestern University¹; Laboratoire de Géophysique, Papeete, Tahiti²

Sponsored by Defense Threat Reduction Agency¹ and Commissariat à l'Energie Atomique²

¹Contract Number DTRA01-00-C-0065

ABSTRACT

In Late 2000, numerous sequences of T phases were detected by seismic stations of the Polynesian network and in the Cook Islands, with an origin in the Ross Sea off the coast of Antarctica. This observation was corroborated by records at seismic stations, at permanent sites VNDA and SBA, and at the volcano monitoring network on Erebus. A combined location procedure using both seismic phases (presumed to be Lg) and T phases, narrowed down the source of the activity to huge icebergs which at the time were drifting in the Ross Sea after calving off the Ross Ice shelf. The signals present a broad variety of spectral characteristics, most of them featuring prominent eigenfrequencies in the 4-to-7 Hz range, often complemented by overtones. Most epicenters follow the spatio-temporal evolution of the drift of iceberg B15-B. The majority of the signals are generated during a 36-day time window when it is speculated that B15-B collided with smaller icebergs or was scraping the ocean floor on the shallow continental shelf. We speculate on the possible physical nature of the resonator generating the signals, which could correspond to an elastic mode of the iceberg, or to the oscillation of the fluid-filled crack in the ice. The signals differ from those previously recorded during volcanoseismic swarms in that the spectral lines have a much higher quality factor Q (in general found to be > 100). Such oscillations document a new source of acoustic energy in the ocean column, which is of general interest in the framework of the CTBT. The location procedure used in this context also underlines the powerful synergy which can be developed between various kinds of geophysical data. In 2002, more such signals are being recorded from various sites around Antarctica, and we also report on these developments, following the break-up of a gigantic segment of the Ross Ice shelf on 2002 May 10.

OBJECTIVE

The objective of this research is the analysis of the source characteristics of hydroacoustics signals in the world's oceans, and in particular the discrimination between man-made explosions and natural sources, such as earthquakes, landslides and volcanoes. We report here on the identification of a new source capable of contributing significant hydroacoustic energy over extended periods of time.

RESEARCH ACCOMPLISHED

Starting in August 2000, seismic stations operating as *T* –phase stations in Polynesia detected irregular activity originating from the Southern Ocean. The activity was concentrated in a group of 13 sequences (hereafter the "Ross Events") whose principal characteristics are listed in Table 1, with representative spectrograms of signals shown on Figures 1a-d. At seismic stations located on atolls, such as Vaihōa (VAH), the acoustic-to-seismic conversion is particularly efficient, and the seismic signal at the *T* –phase station can be regarded as essentially equivalent to the acoustic one inside the SOFAR, within the frequency window of interest ($2 \leq f \leq 16$ Hz). In most instances, the energy of the Ross events is concentrated at one or several prominent frequencies, which suggests that its source must involve the oscillation of some kind of resonator, a model also supported by the often long duration of the signals, e.g., Event 4, which lasts for 3 hours. However, some sequences feature significantly broader spectra (e.g., Event 12), and some like Event 2 (Figure 1a) last no more than 2 minutes. In addition, the frequency of the largely monochromatic signals does fluctuate with time, a property already observed during the Hollister volcanic swarm (Talandier and Okal, 1996), with some of the Ross events featuring more substantial variations of frequency with time (e.g., Event 7), which give the spectrograms a contorted, "snake-shaped" aspect. Finally, several sequences end with singular signals exhibiting an increase of frequency with time (suggestive of the shrinking of the resonator), which can be slow and gradual (Event 4) or fast and abrupt (Event 3, Figure 1b). In the case of Event 13, the termination of the sequence involves a complex evolution of prominent frequencies with time, featuring several episodes of frequency decrease, a property termed "gliding" and identified during episodes of volcanic tremor (Hagerty et al., 1997) which in general terms would suggest a geometrical expansion of the resonator (Chouet, 1996).

A systematic effort was conducted to complement the Polynesian dataset with records at other Pacific seismic stations. When available, the IRIS station at Rarotonga (RAR) provided increased azimuthal aperture; the station was, however, inoperative from 04 to 18 December 2000. Unfortunately, no other seismic station could contribute *T* –phase signals, and this for a variety of reasons, including blockage at NOUC, JOHN, and at the ocean-bottom observatory H2O; unfavorable station locations involving long post-conversion seismic paths (TAU, KIP, XMAS); a probable combination of those two effects at VIB; and a high level of background noise at the small island of Pitcairn (PTCN). Finally, no signal was detected at Easter Island (RPN), where detection of *T* phases has been previously recognized as irregular (Okal and Talandier, 1997; Okal et al., 2001; Reymond et al., 2001).

The principal events in the sequence were first located using the techniques developed by Talandier and Okal (1996) during the Hollister volcanic swarm: using whenever possible impulsive arrival times of sharp sub-events, or in their absence, differential travel-times between stations by cross-correlating the fluctuations with time of the frequency of quasi-monochromatic *T* waves. After implementing station corrections to compensate for the post-conversion land path, the locations of the sources were inverted using the seasonally adjusted, laterally varying model of acoustic velocities of Levitus et al. (1994). The location procedure is enhanced by a Monte Carlo algorithm consisting of injecting Gaussian noise into the dataset of arrival times (Wysession et al., 1991); a best-fitting ellipse is then computed for the resulting cluster of epicenters.

In all cases, these preliminary epicenters locate in the general area of the Ross Sea, and of the Borchgrevink and George V coasts of Antarctica, but the limited azimuthal coverage provided by the band of available stations (at most 30°) results in weak resolution of epicentral distance. Nevertheless, several statistically distinct groups can be identified, with Events 2 and 13 along the coasts, while the remaining epicenters locate in the center of the Ross Sea.

In view of these preliminary results, we conducted a systematic search for additional records of conventional seismic waves at Antarctic stations. We were able to identify signals at the IRIS station at Scott Base (SBA), at the GTSN station Vanda (VNDA), and at several stations of the Mount Erebus Volcanic Observatory (MEVO), located on Ross Island (courtesy of Dr. Richard Aster).

In order to use the Antarctic seismic signals in a combined relocation with the Polynesian T phases, we need to know the velocity of seismic waves along the source-to-receiver path. For this purpose, we tested a series of relocations, for variable values of the velocity V to the Antarctic stations. In this experiment, we used a priori bounds of $V_{\min} = 1.3$ km/s, thus including the possibility of an acoustic velocity in the cold waters of the Southern sea, and $V_{\max} = 8.25$ km/s, corresponding to a P_n velocity under the continental shelf, and we varied V in increments of 0.05 km/s. For each value of V , we quantify the quality of the relocation through the root-means squares of the residuals, σ . We determined that the best-fitting value of V is consistently $V_{opt} = 3.7 \pm 0.2$ km/s.

The interpretation of V_{opt} is not straightforward, and remains somewhat unresolved. On the one hand, it matches well the velocity of P waves in recrystallized ice (Thiel, 1961). However, and even in the case of Event 1, which may have occurred on the Ross Ice Shelf or at its boundary (see below), this interpretation is improbable, since the ice shelf is only 300 m thick, i.e., less than 1/5 of the longest wavelengths recorded in Antarctica. For the other events located farther North, satellite imagery disproves the existence of a continuous layer of thick ice along the path to VNDA.

Rather, we propose to interpret the arrivals at $V_{opt} = 3.7$ km/s as L_g wavetrains, and interpreted as shear energy trapped in the continental crust (e.g., Knopoff, 1973). As documented, for example by Bouchon (1982) and Campillo et al. (1984), L_g can be the first prominent arrival at regional distances in conditions where P arrivals do not emerge from noise, in particular for shallow crustal dislocation sources. In addition, L_g energy can propagate efficiently at frequencies of a few Hz (Bouchon, 1982). Furthermore, the value of V_{opt} falls in the range of predicted and observed L_g velocities in the relevant frequency window (Cara and Minster, 1981). Finally, we will see that the epicentral locations of the Ross Sea events are on the continental shelf or at its boundaries, so that L_g wavetrains would not be blocked by transit over an oceanic path.

Notwithstanding our inability to definitely identify the nature of the seismic phases recorded at Antarctic stations, we will use the optimized velocity $V_{opt} = 3.7$ km/s for all seismic phases at Antarctic stations in order to locate the Ross events from a combined dataset of acoustic and seismic arrival times.

As discussed in Table 1, out of the 13 sequences investigated, we obtain seven very well constrained locations, with semi-major axes of ≈ 25 km for the Monte Carlo ellipses (Events 2, 3, 5, 8, 10, 11, 12), and two poorly resolved ones (Events 1 and 13). The remaining sequences (Events 4, 6, 7, 9) are given tentative locations based on their temporal association with well-located events. As shown on Figure 2, all epicenters, except Events 1, 2, and 13, fall in the center of the Ross Sea. The location of Event 13 (Figure 1d), which was recorded neither by the Antarctic stations nor by RKT, could not be improved beyond the estimate obtained from Polynesian T phases. Event 1 (15 August 2000) has a large uncertainty, but lies significantly South of the November-December group. As for Event 2 (08 November 2000), it has a well constrained epicenter just South of Cape Adare on the Borchgrevink Coast.

We reject volcanism as a possible origin of the Ross Sea events. First, an important aspect of our results is that all nine located events cannot share a common epicenter. This is well documented by the Monte Carlo ellipses on Figure 2, and was confirmed by a formal attempt at inverting the full dataset of arrival times for a common epicenter and distinct origin times, which resulted in unacceptable residuals of more than one minute. We conclude that the location of the Ross Sea events moved with time in a generally SE to NW direction (with the exception of Event 2). Their spatio-temporal evolution is in sharp contrast with our previous experience of long-range hydroacoustic detection at volcanic sites such as Macdonald Seamount and Hollister Ridge (Talandier and Okal, 1996). Second, we note the presence of three known sites of volcanic (or fumarolic) activity in the area: Erebus (77.6°S; 167.2°E), Melbourne (74.35°S; 164.70°E) and the Balleny Islands (66°S; 163°E). When tested as possible epicenters for our datasets, r.m.s. residuals exceeding several minutes made all of these locations unacceptable. In the case of Event 12, for example, Erebus was a legitimate epicenter on the basis of the RSP hydroacoustic data alone). However, the inclusion of the Antarctic dataset leads to a discrepancy of more than 9 minutes between Polynesian and Antarctic stations. We reject volcanism as a source of the Ross Sea events, since even an uncharted volcanic source would have had to move hundreds of km across the Ross Sea over a period of a few weeks.

Rather, we propose that the sources of the Ross Sea events lie within very large icebergs, documented to have calved off the Ross Ice Shelf in the [Northern] Spring of 2000, and which were drifting across the Ross Sea in a northwesterly direction during the later part of the year. We base our interpretation on the dataset of reported coordinates and infrared satellite photographs available from the web site of the University of Wisconsin's Antarctic Meteorological Research Center (Anonymous, 2002a).

Around March-April 2000, Iceberg B-15 (300 km by 40 km) and the smaller B-17 to the East calved off the shelf around 78°S, between 177 and 165°W. By 15 August 2000, the date of Event 1, B-15 had broken up into two principal pieces, B-15A and B-15B, and several smaller fragments. B-15B then takes a Northerly path towards the Center of the Ross Sea, at an average drift velocity of 4 km/day (or 5 cm/s). Figure 2 plots the positions of B-15B and B-17 at a number of dates between 09 November 2000 and 05 January 2001. During that time window, B-15B engages in a large rotation, collides with B-17 in Early November 2000, calves off a further small fragment, B-15F, on its West side, some time between 14 November and 29 November 2000, and frees itself from B-17 as the latter breaks into pieces around 30 December 2000. By 05 January 2001, B15-B has taken a Northwesterly direction, rounds Cape Adare about 03 May 2001 (it has then broken into two parts), and then progresses along the Oates Coast, where it currently (2002) lies around 155°E (Anonymous, 2002b).

As documented on Figure 2, there is a spectacular correlation between the epicenters of Events 3, 5, 8, 10, 11 and 12 (and hence presumably of the intervening Events 4, 6, 7, 9) and the location of the icebergs B15-B and B-17. In particular, the spatio-temporal evolution from the Southeastern group of epicenters (3, 5, 8) in November to the Northwestern one (10, 11, 12) in December mimics the drift and rotation of B-15B. In the case of the relatively poorly located Event 1 (on 15 August 2000), Figure 2 shows the Northern end of the large Monte Carlo ellipse similarly intersecting the position of B15-B on that same day.

On this basis, we propose that the source of the Ross Sea events consists of unidentified phenomena taking place inside large icebergs (principally B15-B) drifting in the Ross Sea.

As discussed below, we can offer only vague speculation as to the nature of the events taking place inside the icebergs and generating the hydroacoustic and seismic signals studied. Whatever these phenomena may be, it is remarkable that they take place only during a small part of the long drift of B-15B from the Ross Ice shelf to Cape Adare and beyond, namely during a 36-day window and over a distance of less than 200 km (with the exception of Event 1, farther South). In particular, B-15B becomes silent after 18 December 2000, and during its 4-month voyage to Cape Adare. We know of no prominent bathymetric feature which would explain this pattern through hydroacoustic blockage along the path to Polynesia. Rather, B-15B's silence must reflect the cessation of the physical source process.

Among possible mechanisms for the excitation of an oscillator, that would be geographically (or temporally) controlled, we envision collisions with other ice masses, and rubbing on the sea floor. A possible scenario would correlate the Ross Sea events with the collision between B-15B and B-17, which lasted at least one month, until B-17 breaks into pieces at the end of December. Another scenario would be to invoke friction on the floor of the Ross Sea. Bathymetric coverage of the Ross Sea is scarce, especially since the relevant area lies outside the Southern limit (72°S) of Smith and Sandwell's (1994) satellite altimetry database. However, the Northern portion of B-15B's path (traveled Westwards after 01 January 2001) most probably lies over deep water, whereas its Southern portion (traveled Northwards) is over the continental shelf. We can only speculate as to the presence of large seamounts or other underwater structures, against which the iceberg could have rubbed, but the spatio-temporal distribution of the Ross Sea events would be in very general agreement with this scenario. We also note that significant iceberg furrows have been documented on the sea floor, including around Antarctica, at depths as great as 400 to 500 m (Harris and Jollymore, 1974; Barnes and Lien, 1988), making it legitimate to assume that motion over the continental shelf at similar depths would occasionally involve scraping against bathymetric features. Finally, as shown by Campillo et al. (1984), a superficial source (such as an iceberg scraping the ocean floor) will excite L_g most efficiently, whereas the excitation of P_g would be relatively insensitive to depth; these properties would lead naturally to L_g being the prominent seismic phase for sources exciting the solid Earth at the water-crust interface.

Regarding the actual physical nature of the sources generating the Ross Sea signals, the prominence of distinctive frequencies (typically 4 Hz) in many spectra (occasionally with harmonics) suggests the oscillation of a resonator. In this respect, our sources differ significantly from the "icequakes" widely observed ever since seismic stations were installed on glaciers and large icecaps. Being essentially instantaneous sources, the latter are characterized by short durations and a broad spectrum featuring high frequencies (Sinadinovski et al., 1999). Even the so-called "low-frequency icequakes" attributed to calving of ice blocks from glaciers (Qamar, 1988) and occasionally featuring a monochromatic spectrum (VanWormer and Berg, 1973) are of much shorter duration than the Ross events.

In order to investigate more in detail the spectral characteristics (eigenfrequency and quality factor Q) of a representative signal, we selected the VAH record from Event 4 (on 12 November 2000) because of its exceptional duration (3 hours). For this purpose, we use a running window of 81.9 s duration (4096 samples), offset 10 s at a time. At

each step, we then identify the frequency f_0 at which the spectral amplitude $X(f)$ reaches its maximum, which we interpret as the eigenfrequency of the resonator, and we fit a resonance curve of the form

$$X_r(f) = \frac{A}{\sqrt{(f - f_0)^2 + \frac{\pi^2 f_0^2}{Q^2}}} \quad (1)$$

to the shape of the spectral amplitude $X(f)$ in the frequency interval $I \{f_0 - 0.125 \text{ Hz} \leq f \leq f_0 + 0.125 \text{ Hz}\}$. We retain only values of Q for those windows where $X(f_0)$ is at least 40% of its maximum value, and for which the spectral line is adequately modeled by (1), as defined its goodness of fit. The two frames on Figure 3 show the variation of f_0 and Q as a function of time t , taken at the center of the running window.

While f_0 can remain remarkably constant over intervals of time of a few minutes (see Figure 1), Figure 3a shows that it varies significantly on a time scale of tens of minutes. Changes in f_0 can be continuous (e.g., the "gliding" observed at the start of the record), or sharp and stepwise, the windows with stronger and cleaner signals being more stable in frequency. This would require the presence of several oscillators, some of which capable of an evolution with time of their eigenfrequency, which in turn most probably expresses an evolution of their dimension.

The quality factors Q of the resonators range between 100 and 650, with an inverse average value of 250, much greater than typically reported for volcanic tremor ($Q = 5$ to 10) or even during the Hollister swarms ($Q = 20$ to 50); this further argues strongly against a volcanic origin for the Ross Sea signals. The attenuation of seismic waves in ice has been reported in the Greenland icefield by Langleben (1969) who reported a fall-off coefficient $c_1 = 4.45 \times 10^{-2} \text{ dB m}^{-1} \text{ kHz}^{-1}$ equivalent to $Q = 166$, and in sea ice by Kohnen (1970), who gives a slope of attenuation with frequency $q = 0.56 \times 10^{-5} \text{ m}^{-1} \text{ Hz}^{-1}$, equivalent to $Q = 175$. Note however that these values were measured at considerably higher frequencies in both studies, and on longitudinal waves in the latter.

Speculating further on the possible physical nature of the resonator, we note the approximate dimensions of B-15B, 135 km by 40 km, and we take its thickness as at least 300 m, based on an estimation of the emerged fraction from airborne photographs, and of the thickness of the Ross Ice shelf from seismic soundings. We can then eliminate gravitational oscillations as the source of the signals, since the bobbing frequency of the iceberg on the sea would be on the order of 30 mHz, rather than 4 Hz. Rolling and pitching eigenfrequencies would also be much lower than observed — on the order of 20 mHz.

Rather, the frequencies observed could represent various eigenmodes of oscillation of the iceberg. For example, for a 300-m thick ice layer, the eigenfrequency of a vertical shear mode would be 3.07 Hz (with $\beta = 1.84 \text{ km/s}$, or a Poisson ratio of 0.34). The eigenfrequency of a fundamental "Crary" mode (Ewing and Crary, 1934; essentially a shear wave propagating horizontally with a phase velocity equal to the P -velocity α) would be 3.51 Hz for the ice sheet in a vacuum; it could be affected by the presence of water (Press and Ewing, 1951), but its order of magnitude would remain in general agreement with the resonance frequencies observed in our signals. This interpretation would be particularly likely under the assumption that the ice mass is set in resonance by scraping the ocean floor, or rubbing against another ice mass; it could also explain the presence of harmonics, or overtones, since several modes would be excited by a source essentially similar to hitting a bell, and resulting in musical "richness". However, under this scenario, the iceberg would be expected to resonate at a set of discrete, and well defined pitches, and the observed continuous fluctuation of eigenfrequency with time would be more difficult to explain.

Another scenario would involve the resonance of a fluid-filled cavity in a mode comparable to the oscillation of magma within a fissure in a volcanic system (Aki et al., 1977). As summarized by Chouet (1996), the eigenfrequencies of such a resonator are complex functions of its size and shape, and of the impedance contrast between the fluid filling the crack and the surrounding medium. In the particular case of icebergs, the fluid would have to be water, but the almost certain presence of air bubbles could greatly reduce the sound speed in the fluid. Furthermore, this model could explain the observed fluctuations of frequency with time, as both the dimension of the resonator and the supply of air bubbles could be expected to vary with time continuously, for example during filling or emptying of the fluid in the crack. These interpretations remain of course highly speculative at this point.

CONCLUSIONS AND RECOMMENDATIONS

We have documented prolonged episodes of hydroacoustic activity in the Ross Sea during the months of August-December 2000. By combining datasets of T phases recorded in Polynesia with regional seismic phases recorded at

Antarctic stations, we obtain epicentral locations correlating systematically with the position of large icebergs, specifically B-15 B and B-17, which were drifting in the Ross Sea at that time, and thus we conclude that the signals originated at or inside the icebergs. This study illustrates the powerful synergy obtained by combining hydroacoustic and classical seismological datasets, and resulting in epicentral precision of a few tens of km in a very remote area of the world's oceans.

Despite a broad variability in the spectral characteristics of the Ross events, they cannot be compared to seismic sources previously identified and analyzed in the ice environment, such as icequakes and calving events. Rather, our observations define a new kind of source capable of contributing hydroacoustic energy to the SOFAR channel over extended periods of time. The presence of preferential frequencies in the 3 to 7 Hz range (often associated with overtones) clearly implicates the resonance of an oscillator, whose exact nature presently eludes us. In the context of the use of hydroacoustic waves for explosion monitoring, it is clear that a deeper investigation of the phenomena involved is warranted; a possible avenue would involve the direct deployment of portable seismic stations on massive icebergs known to be calving off the major Antarctic ice shelves (May 2002).

REFERENCES

- Aki, K., M. Fehler, and S. Das (1977), Source mechanism of volcanic tremor; fluid-driven crack models and their application to the 1963 Kilauea eruption, *J. Volcanol. Geotherm. Res.*, 2, 259–287.
- Anonymous (2002a), Antarctic Meteorological Research Center, <http://amrc.ssec.wisc.edu>, Univ. Wisconsin, Madison.
- Anonymous (2002b), National Ocean and Atmospheric Administration, <http://www.noaanews.noaa.gov/stories/s862.htm>, U.S. Dept. of Commerce.
- Barnes, P.W., and R. Lien (1988), Icebergs rework shelf sediments to 500 m off Antarctica, *Geology*, 16, 1130–1133.
- Bouchon, M. (1982), The complete synthesis of seismic crustal phases at regional distances, *J. Geophys. Res.*, 87, 1735–1741.
- Campillo, M., M. Bouchon, and B. Massinon (1984), Theoretical study of the excitation, spectral characteristics, and geometrical attenuation of regional seismic phases, *Bull. Seismol. Soc. Amer.*, 74, 79–90.
- Cara, M., and J.B. Minster (1981), Multi-mode analysis of Rayleigh-type L_g , *Bull. Seismol. Soc. Amer.*, 71, 973–984.
- Chouet, B. (1996), New methods and future trends in seismological volcano monitoring, in: *Monitoring and mitigation of volcano hazards*, ed. by R. Scarpa, and R.I. Tilling, pp. 23–97, Springer, Berlin.
- Ewing, M., and A.P. Crary (1934), Propagation of elastic waves in ice, II, *Physics*, 5, 181–184.
- Hagerty, M.T., M.A. Garces, S.Y. Schwartz, and M. Protti (1997), Long-term broad-band observations of ground deformations at Arenal Volcano, Costa Rica, *Eos, Trans. Amer. Geophys. Un.*, 78, (46), F431 [abstract].
- Harris, I.McK., and P.G. Jollymore (1974), Iceberg furrow marks on the continental shelf Northeast of Belle Isle, Newfoundland, *Can. J. Earth Sci.*, 11, 443–524.
- Knopoff, L. (1973), Interpretation of L_g , *Geophys. J. Roy. astr. Soc.*, 33, 387–402.
- Kohnen, H. (1970), Über die Absorption elastischer longitudinaler Wellen im Eis, *Polarforschung*, 39, 269–275.
- Langleben, M.P. (1969), Attenuation of sound in sea ice, 10–500 kHz, *J. Glaciology*, 8, 399–406.
- Levitus, S., T.P. Boyer, J. Antonov, R. Burgett, and M.E. Conkright (1994), *World Ocean Atlas 1994*, NOAA/NESDIS, Silver Springs, Maryland.
- Neave, K.G., and J.C. Savage (1970), Icequakes on the Athabasca glacier, *J. Geophys. Res.* 75, 1351–1362.
- Okal, E.A., and J. Talandier (1997), T waves from the great 1994 Bolivian deep earthquake in relation to channeling of S wave energy up the slab, *J. Geophys. Res.*, 102, 27421–27437.
- Okal, E.A., P.-J. Alasset, O. Hyvernaud, and F. Schindelé (2001), The deficient T waves of tsunami earthquakes, *Geophys. J. Intl.*, submitted.
- Press, F., and M. Ewing (1951), Propagation of elastic waves in a floating ice sheet, *Trans. Amer. Geophys Un.*, 32, 673–678.
- Qamar, A. (1988), Calving: A source of low-frequency seismic signals from Columbia Glacier, Alaska, *J. Geophys. Res.*, 93, 6615–6623.
- Reymond, D., O. Hyvernaud, J. Talandier, and E.A. Okal (2001), T –wave detection of two underwater explosions off Hawaii on April 13, 2000, *Bull. Seismol. Soc. Amer.*, submitted.
- Sinadinovski, C., K. Muirhead, S. Spiliopoulos, and D. Jespen (1999), Effective discrimination of icequakes on seismic records from Mawson station, *Phys. Earth Planet. Inter.*, 113, 203–211,

24th Seismic Research Review – Nuclear Explosion Monitoring: Innovation and Integration

- Smith, W.H.F., and D.T. Sandwell (1994), Bathymetric prediction from dense satellite altimetry and sparse ship-board bathymetry, *J. Geophys. Res.*, 99, 21803–21824.
- Talandier, J., and E.A. Okal (1996), Monochromatic *T* waves from underwater volcanoes in the Pacific Ocean: Ringing witnesses to geyser processes?, *Bull. Seismol. Soc. Amer.*, 86, 1529-1544.
- Thiel, E., and N.A. Ostenso (1961), Seismic studies on Antarctic ice shelves, *Geophysics*, 26, 706–715.
- VanWormer, D., and E. Berg (1973), Seismic evidence for glacier motion, *J. Glaciology*, 12, 259–265.
- Wyssession, M.E., E.A. Okal, and K.L. Miller (1991), Intraplate seismicity of the Pacific Basin, 1913–1988, *Pure Appl. Geophys.*, 135, 261-359.

Table 1. Principal characteristics of the 13 events studied

Number	Date and time D M (J)	Epicenter		Duration (mn)	Peak-to-peak velocity at VAH ($\mu\text{m/s}$)	Remarks
		(°S)	(°E)			
1	15 AUG (228) 22:28:18.6	78.21	-168.61	1.3	1.23	Edge of Ross Ice Shelf. No data at RAR, RKT. Monochromatic signal (3.5 Hz) with overtones; sharp impulsive beginning.
2	08 NOV (313) 22:18:31.3	72.10	170.16	2	2.18	Borchgrevink Land. Relatively monochromatic; frequency fluctuates; no overtones.
3	12 NOV (317) 01:13:26.6	75.76	-175.75	8	0.62	Central Ross Sea. Generally weak at Antarctic stns. Narrow spectrum centered around 4 Hz. Strong final puff with frequency increasing with time.
4	12 NOV (317) 06:00 — 09:00	75.8	-175.8	3 hr	0.24	Central Ross Sea. Only traces in Polynesia (except VAH); No signal at SBA and Erebus. Long signal, generally monochromatic (2.5 to 4 Hz), with frequency fluctuations but few overtones.
5	14 NOV (319) 01:01:56.6	75.92	-175.60	3	0.81	Central Ross Sea. No data: Erebus; No signal: SBA. Relatively broad spectrum on acoustic records. Dominant frequency 2.5 Hz at VNDA.
6	19 NOV (324) ~ 02:30	75.8	-175.8	10	0.42	No signal: RSP except VAH. No data: Erebus, SBA. Broad spectrum (2 – 16 Hz). Assumed in same area as Events 3–5, based on times at VNDA & VAH.
7	21 NOV (326) 15:22	75.8	-175.8	10	0.24	No signal: Polynesia except VAH. No data: Erebus, SBA. Fluctuation of dominant f , leading to "snake-shaped" spectrogram. Assumed at same location as Events 4–6, based on VNDA & VAH times.
8	22 NOV (327) 21:32:13.0	75.85	-176.28	10	0.34	Central Ross Sea. No data: Erebus, SBA. Same general characteristics as Event 7.
9	05 DEC (340) 03:21:19.8	75.08	-177.75	8	0.30	Central Ross Sea. No data: Erebus; No signal: SBA. Broad spectrum (2 – 10 Hz), with dominant f = 2.9 Hz. Final sequence with sharply increasing frequency.
10	05 DEC (340) ~ 20:46	75.1	-177.8	15	0.32	Noisy record; broad spectrum (2 - 10 Hz), with 2 sequences; assumed to share location of Event 9.
11	15 DEC (350) 03:16:14	74.4	-178.4	10	0.44	Central Ross Sea. No signal: SBA. Broad spectra (2 - 12 Hz); weak correlation of acoustic and seismic records.
12	18 DEC (353) 09:56:29.1	74.82	-178.68	8	0.42	Central Ross Sea. Two parts; 1st short (30 s) with impulsive start; 2nd emergent and long (150 s). Broad spectrum.
13	14 JAN (014) 2001 17:36:10	67.0	141.5	7	1.31	Off Oates or George V Coasts. No signal: RKT; all Antarctic stations. Relatively broad spectrum with dominant f at 4, 5.5 and 7 Hz; first sequence ends abruptly, followed by short (60 s) puff, with spectrogram showing several lines of strongly decreasing frequencies (gliding). Location only tentative.

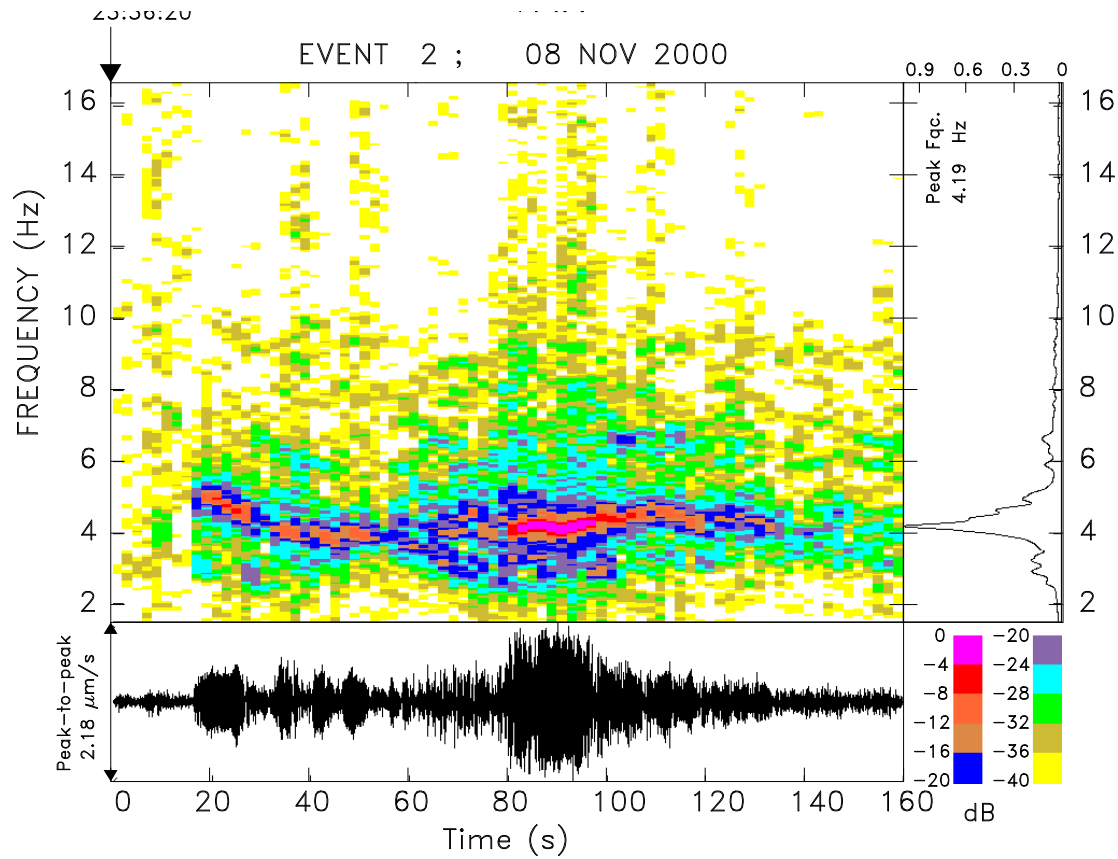


Figure 1a. T-phase record of Event 2 at Vaihoo. The figure is composed of three frames: The bottom one shows a 160-second time series of the ground velocity (in black), high-pass filtered for $f \geq 2$ Hz. The frame at right is a plot of the amplitude spectrum of the high-pass-filtered ground velocity record. The main color frame is a spectrogram representation of the distribution of spectral amplitude in the record, as a function of time and frequency. The color-coding is logarithmic, with the key (in dB relative to the most energetic pixel) given at bottom right. White pixels correspond to spectral amplitudes below -40 dB. Note the impulsive start of the signal, and the slow, contained, fluctuation of the prominent frequency with time.

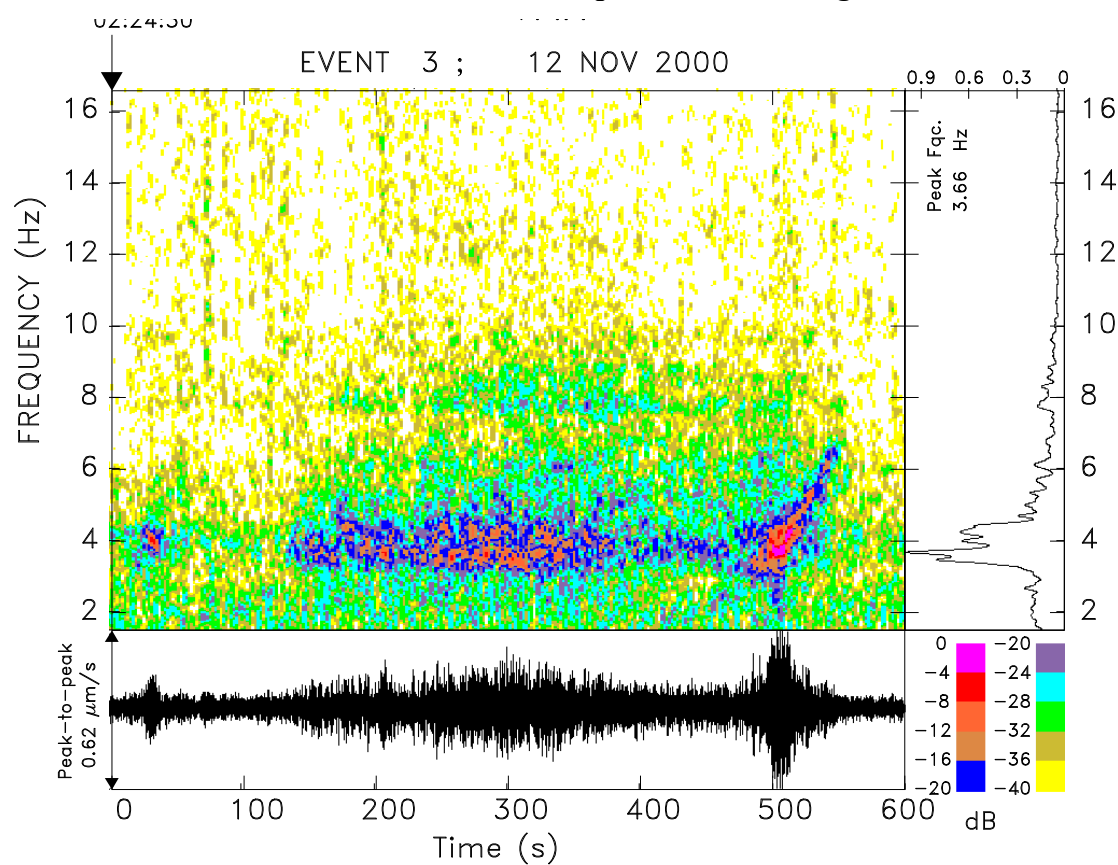


Figure 1b. Same as Figure 1a for Event 3. The time series is now 600-s long. Note the singular signal ending the sequence, featuring an increase of frequency with time.

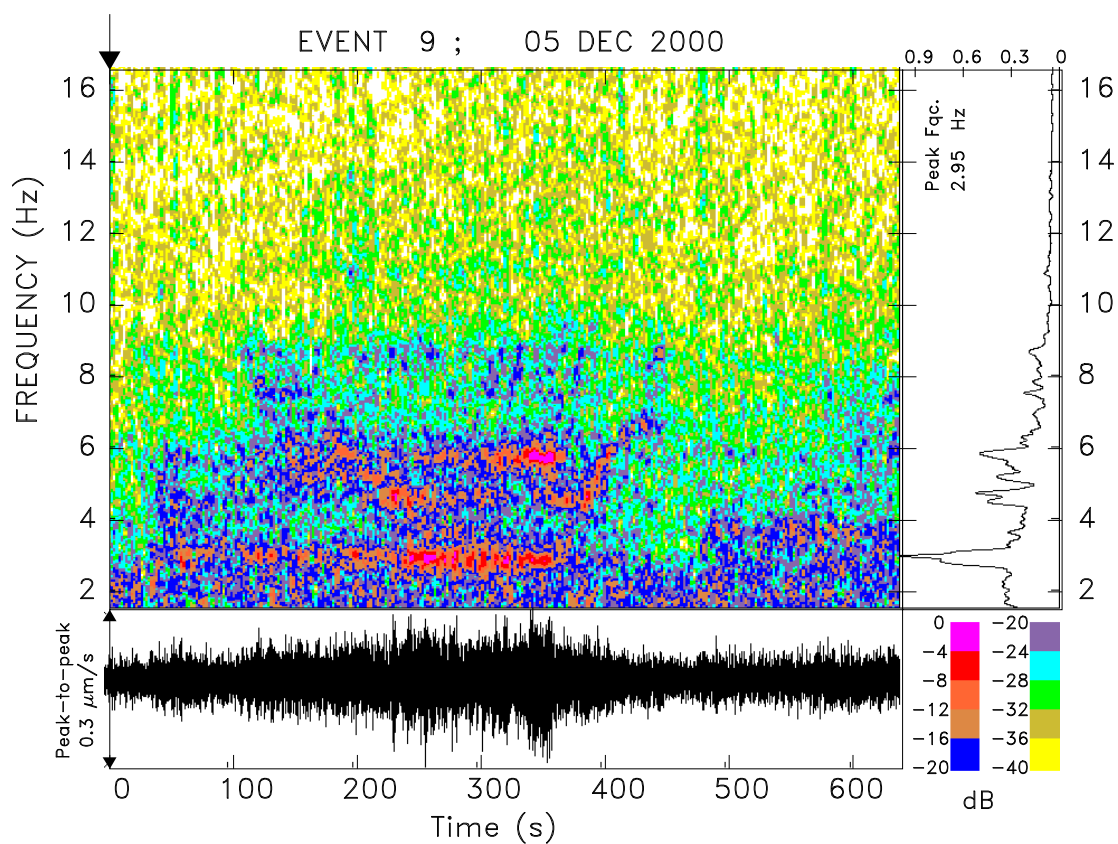


Figure 1c. Same as Figure 1a for Event 9. Note the relative complexity of the spectrum, and the trend towards an increase in frequency at the end of the main pulse (400 s into the signal).

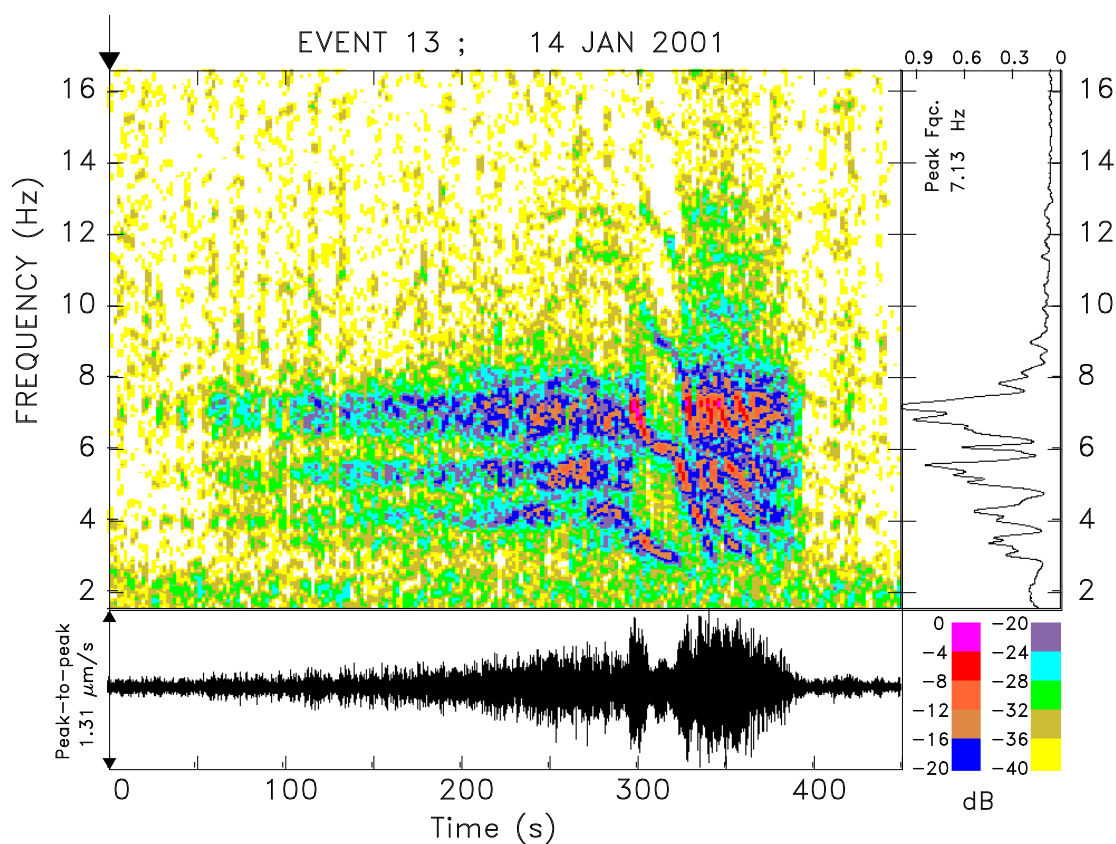


Figure 1d. Same as Figure 1a for Event 13. Note the complex character of the spectrogram, especially in the final phases of the pulse, where the eigenfrequency tends to decrease with time ("gliding").

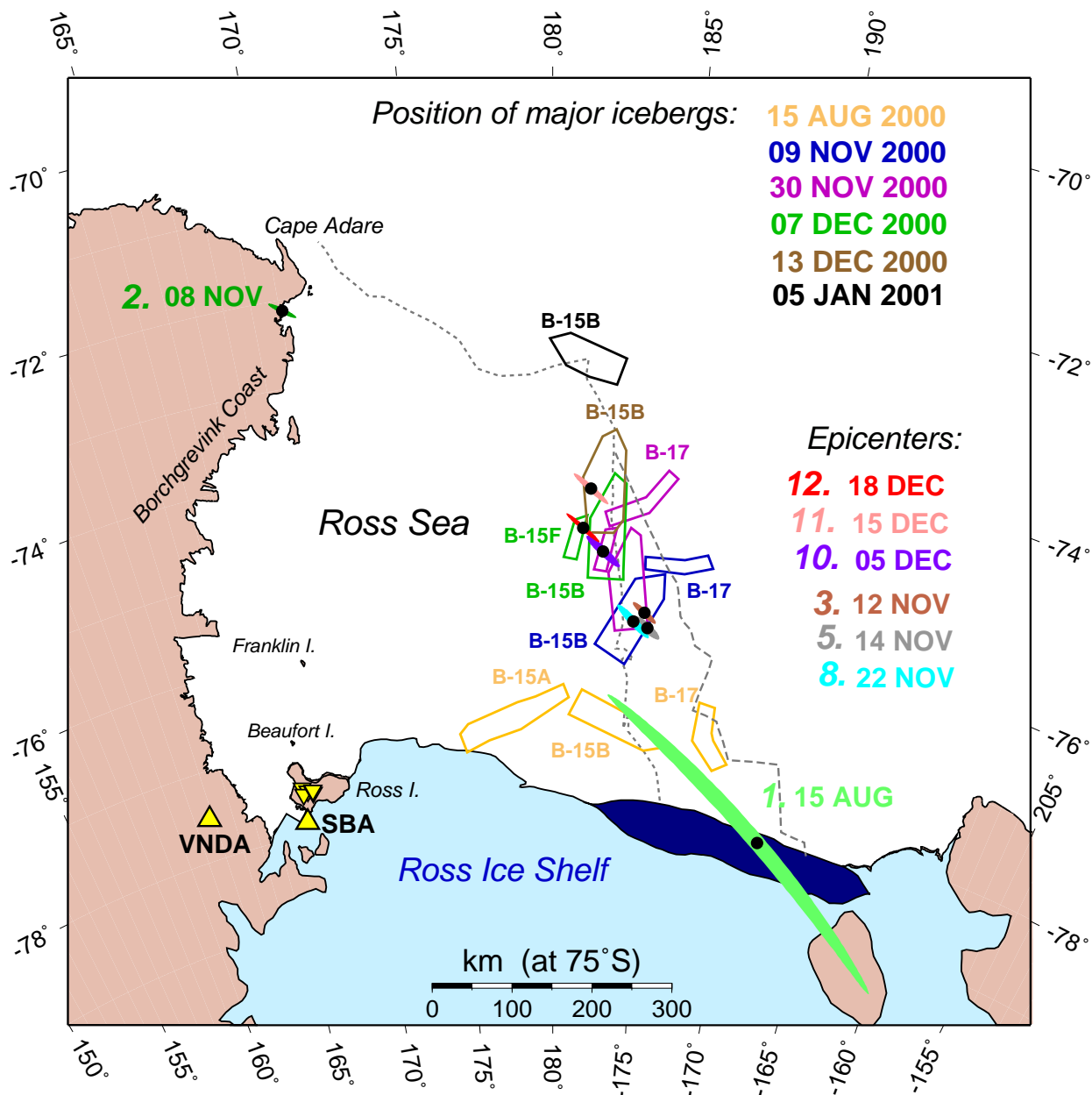


Figure 2. Final epicenters obtained by joint inversion of T-phase and seismic data. The individual epicenters are shown as black solid dots and the associated Monte Carlo ellipses are shaded (see color key at right; Event numbers in italics). The position of B-15 B is shown schematically at a number of dates from August 2000 to January 2001 (color-keyed; legend at top). Positions of the smaller iceberg B-17 are also shown at a few critical times until Late November 2000, when it breaks up into pieces following its collision with B-15 B. The paths of the two icebergs are also shown continuously by the dotted (B-15 B) and dashed (B-17) lines. The upward-pointing triangles show the global network seismic stations VNDA and SBA, the downward-pointing ones the MEVO network on Ross Island. The dark blue region schematizes the portion of the shelf which calved off and eventually gave rise to the B-15 and B-17 series. The projection is equidistant azimuthal centered at the South Pole.

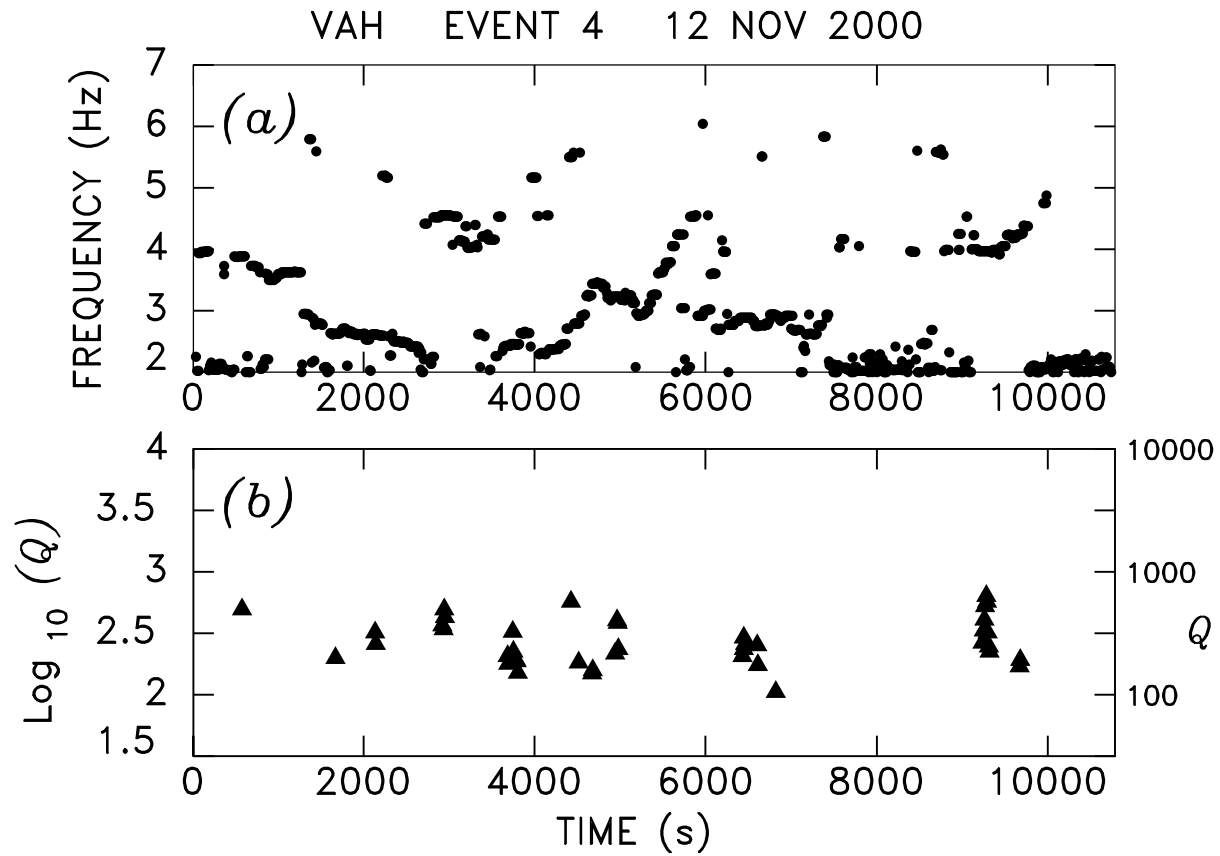


Figure 3. Evolution of spectral properties with time during Event 4. (a): Frequency f_0 at maximum of spectral amplitude. (b): Values of Q retained by application of quality thresholds.

ANALYSIS OF HYDROACOUSTIC SIGNALS IN THE INDIAN OCEAN

M. Tolstoy and D.R. Bohnenstiehl

Lamont-Doherty Earth Observatory, Columbia University

Sponsored by Defense Threat Reduction Agency

Contract No. DTRA01-01-C-0070

ABSTRACT

Hydroacoustic processing software developed over the past decade by National Oceanographic and Atmospheric Administration Pacific Marine Environmental Laboratory (NOAA/PMEL) has been modified to process CSS 3.0 format data from hydroacoustic stations within the Indian Ocean. This allows for the simultaneous inspection of multiple hydrophone channels, displaying trace amplitudes and spectrograms. When the hydroacoustic station at Crozet (H04) comes online in February 2003, this software package will allow events within the Indian Ocean Basin to be rapidly located solely on the basis of hydroacoustic arrivals, using a non-linear least squares algorithm that minimizes the differences between recorded and predicted T-wave arrivals. Previous work in other ocean basins suggests that this approach will improve significantly our detection capability and location accuracy for Indian Ocean earthquakes. Given the final configuration of the Indian Ocean Hydroacoustic Network (stations H04, H08, H01), point-source simulations suggest location accuracy of ~2 km (68% level) within much of the array, assuming a random arrival error with normal distribution and standard deviation of 0.75 s for all channels. However, errors within the ocean sound velocity model and the width of the T-wave source region will decrease the accuracy of locations within the basin.

Commonly detected signals at the existing Diego Garcia (H08) and Cape Leeuwin (H01) hydrophones include a range of seismic phases (most commonly T, P and S), marine mammal vocalizations, ice-sheet movements, airguns and shipping noise, as well as other presently unidentified sounds that may be anthropogenic or natural in origin. Initial estimates of station noise levels indicate that Diego Garcia North is the quietest station, followed by Diego Garcia South and then Cape Leeuwin. When a full year's data have been analyzed, a catalog of annual noise variations will be merged with seismic and T-wave derived earthquake catalogs to examine the impact of noise on the hydrophones array's detection and location capabilities.

The natural seismicity within the ocean basin is used to map out areas of topographic blockage. The expected arrival time at individual hydrophones is calculated from Reviewed Event Bulletin (REB) events and each hydrophone is inspected for detectable T-waves. Based on the presence or absence of signals, regions of topographic blockage are mapped for the H01 and H08 hydrophones. Preliminary analysis of 2002 data indicates that $>3.0 m_b$ events within the deep basin should be detectable on at least one hydrophone triad, given the final configuration of the network.

The incorporation of CSS 3.0 format data into the NOAA/PMEL processing suite improves synergy between hydroacoustic and seismic datasets. In the future, T-wave arrivals at island atoll stations (such as COCO, Keeling Island) could be used jointly with the hydrophone stations to locate events within an ocean sound velocity model.

OBJECTIVES

Hydroacoustic monitoring is a critical component of the Comprehensive Nuclear-Test-Ban Treaty (CTBT). It ensures that nuclear tests conducted in the ocean, or in the lower atmosphere directly above the ocean, do not go undetected. As such, it is essential that sub-oceanic earthquakes and other natural acoustic sources can be identified and subsequently ruled out as explosions. This requires a full characterization of the geological, biological and man-made noises generated within an ocean basin on a day-to-day basis. Characterizing the source and location of various signals provides an important framework by which to further improve our understanding of hydroacoustic wave propagation. Moreover, as the hydroacoustic network expands into new areas of geologic and anthropogenic complexity, prioritizing such work ensures the timely and efficient use of the network as a monitoring tool.

Given the limited number of hydroacoustic stations within the present International Monitoring System (IMS) that report to the International Data Centre (IDC), we also must assess the ability of land-based stations alone, or in conjunction with a limited number of hydrophones, to accurately detect and locate events within the oceans.

The research presented here represents a preliminary characterization and quantification of Indian Ocean acoustic sources, using existing IMS hydroacoustic stations (Figure 1). The routine location of events using hydroacoustic sensors alone will begin once the Crozet hydroacoustic station comes on line. Existing techniques for locating events using topographic reflections are too labor intensive to be used for all the many thousands of events occurring in the Indian Ocean basin each year. As part of this research we have adapted existing academic hydroacoustic analysis software to incorporate both hydroacoustic and seismic data from the IMS. This software will allow rapid location of small events when the Indian Ocean network is completed and currently provides an efficient platform for event characterization and quantification. This includes not only identifying the source origin and signal strength but also providing station specific topographic blockage and background noise information.

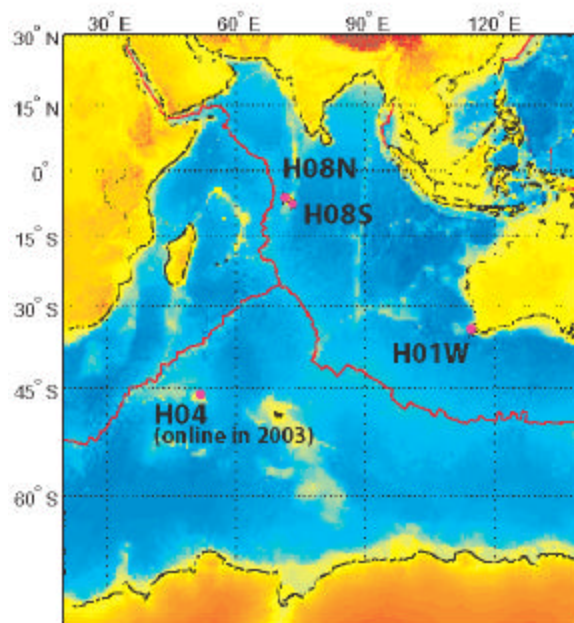


Figure 1. Location of IMS hydroacoustic stations in the Indian Ocean. Diego Garcia North & South (H08N & H08S) and Cape Leeuwin (H01W) are currently operational. Crozet (H04) is expected to come on-line in February 2003. At each station there is a three-hydrophone array, or triad, with an instrument separation of ~2 km.

RESEARCH ACCOMPLISHED

Software

We have adapted the hydroacoustic analysis software developed at NOAA-PMEL (Fox et al., 2001) for use in the Indian Ocean. This work included the development of an Indian Ocean sound speed model (based on the Generalized Digital Environmental Model (GDEM) developed by the US Naval Oceanographic Office) and writing of conversion code to allow the CSS format data to be read directly into the software. The software allows data from different stations to be visually inspected, side by side, (Figure 2) and for events to be picked and located.

Based on the final configuration of the Indian Ocean Hydroacoustic Network (when the Crozet stations are operational), point-source simulations are used to predict the expected location errors. Figure 3 shows expected location error for events observed on at least three of the hydroacoustic stations (H-08S, H-01 & H04). The event location and magnitude is calculated based on an iterative, non-linear least squares method developed at NOAA-PMEL in which the sound is propagated through the ocean medium as represented by digital sound speed, in this case the GDEM model. A preliminary location and source time is used to predict arrival times at each sensor. The predicted time is compared to recorded arrival times, and the differences iteratively minimized using a Gradient-Expansion (Marquardt) algorithm, a least-squares method. Following the determination of the position and source time, statistics are calculated and a simple spherical and cylindrical propagation equation is used to estimate propagation loss for each path. This factor is applied to the peak recorded acoustic energy for each sensor and multiple independent estimates of the source strength calculated. The mean and variance of this estimate is saved (Fox *et al.* 2001). Based on the final configuration of the Indian Ocean Hydroacoustic Network (when the Crozet hydrophones are operational), point-source simulations are used to predict the expected location errors. Figure 3 shows expected location errors in kilometers for point-source events observed on at least three of the hydroacoustic stations (H-08S, H-01 & H04).

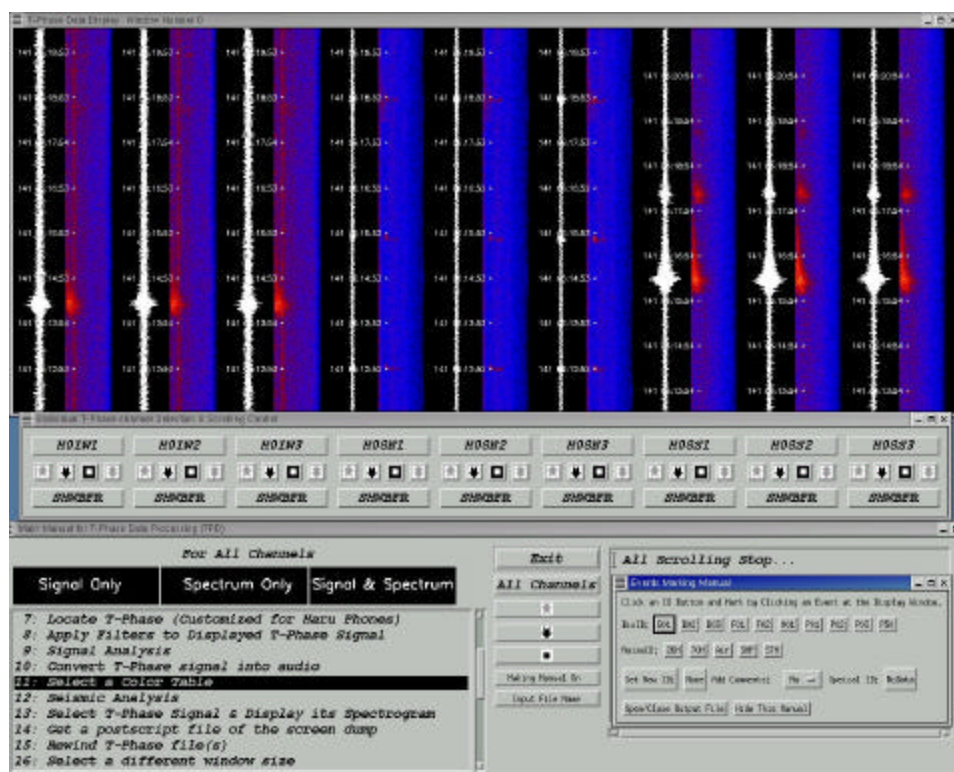


Figure 2. Example of software interface with data being simultaneously scrolled at all three hydroacoustic sites. Time increases on vertical axis, with trace amplitudes and 0-125 Hz spectrograms displayed.

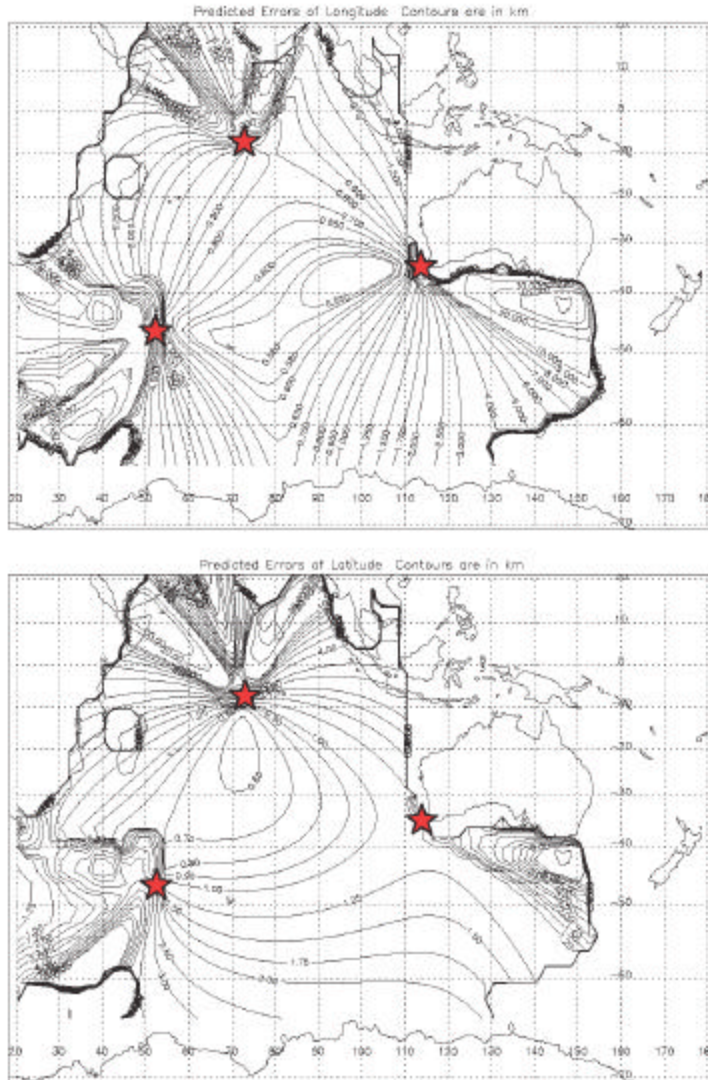


Figure 3. Predicted point-source location errors using an Indian Ocean sound speed model for the anticipated hydrophone configuration in February 2003 (see Figure 1). Location error estimates in latitude and longitude represent the 1σ (68%) confidence level and are given in kilometers. The error field was generated from Monte Carlo simulations of point sources and assumes arrival picks from six hydrophones (two at each triad, red stars). For each simulation the point-source location is prescribed and a random error with normal distribution and 0.75-s standard deviation is added to each arrival. The standard deviation of the picking error is based on calibrations within the Pacific (Fox *et al.*, 2001). Location errors may be larger due to uncertainties in sound speeds along the path, which are not well known, and the width of the T-wave source region on the seafloor. However, similar to arrays in the Atlantic and Pacific Oceans, we expect to be able to calibrate the Indian Ocean array using known sources.

Synergy with land seismic data

The software development completed now allows data from land-based seismic stations to be scrolled simultaneously along side the hydroacoustic data (Figure 4). For stations near the coast, a simple time correction (to allow for the faster travel time of the crustal borne portion of the T-wave) would allow near shore stations to be used as additional T-wave monitoring sites, thus improving location accuracy.

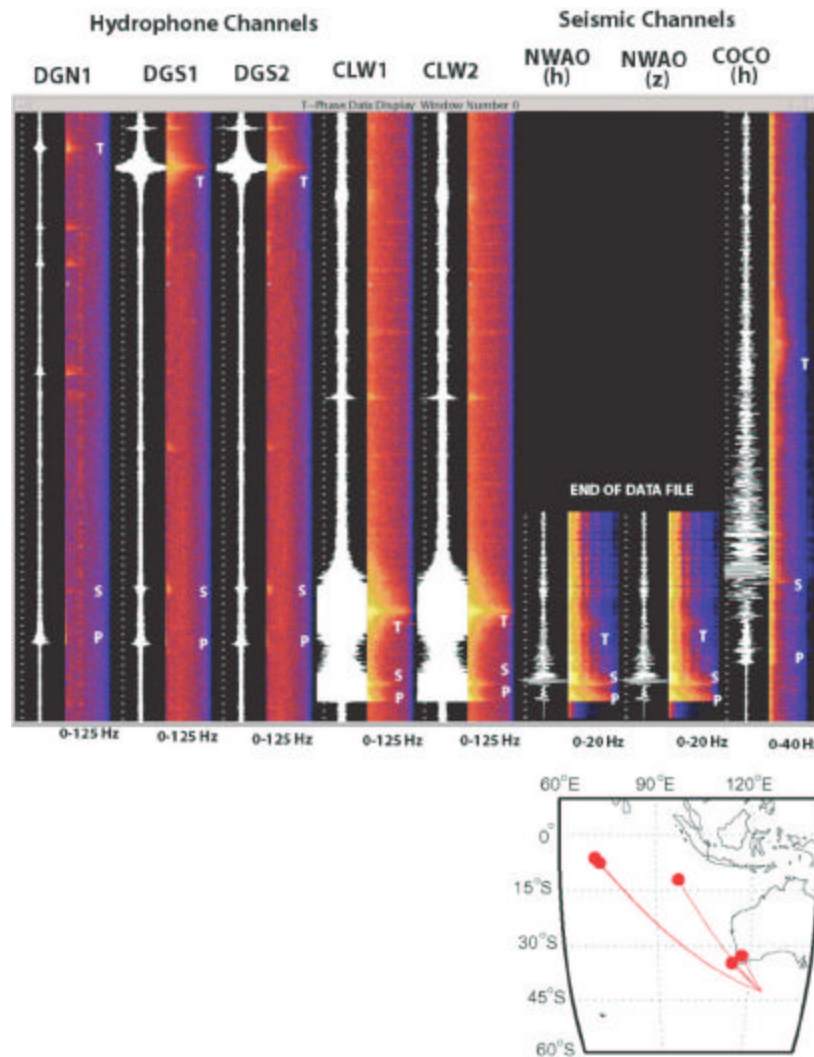


Figure 4. Example of arrivals from a large ocean basin event (7.1 Mw, JD 346, 2001) on hydrophones (HO8N, HO8S & HO1W), and land seismic stations in southwestern Australia (NWA0) and Cocos/Keeling Island (COCO). Great circle paths are shown below. NWA0 is ~200 km from the shelf where the T-wave would be converted into a crustal phase, so it is not ideal. However, the event was large enough that some T-wave related energy is still observed. Note it is about the same distance from the event as HOW1, and the P & S arrivals come in at the same time. The T-wave energy arrives earlier at NWA0, however, since it travels at faster crustal velocities for the last ~200 km of its path. The COCO station is located on a small island atoll, providing a short seismic path and excellent T-wave recording.

Event Characterization

Characterization of events is accomplished through visual inspection of the data, primarily in spectrogram form. Considerations in determining the event type include frequency content, duration, pattern through time, and relative amplitude if it is seen at both HO8 and HO1. While some signals are apparent in the waveform data, the spectrogram is much more informative, as seen in some of the examples below (Figure 5). Event characterization is important for a number of reasons. First, it is the initial step that must be taken before quantifying events and characterizing the ‘typical’ background signals in the Indian Ocean. Further, it will enable improved detection algorithms to be developed by establishing the amplitude and time/frequency range of various known signals.

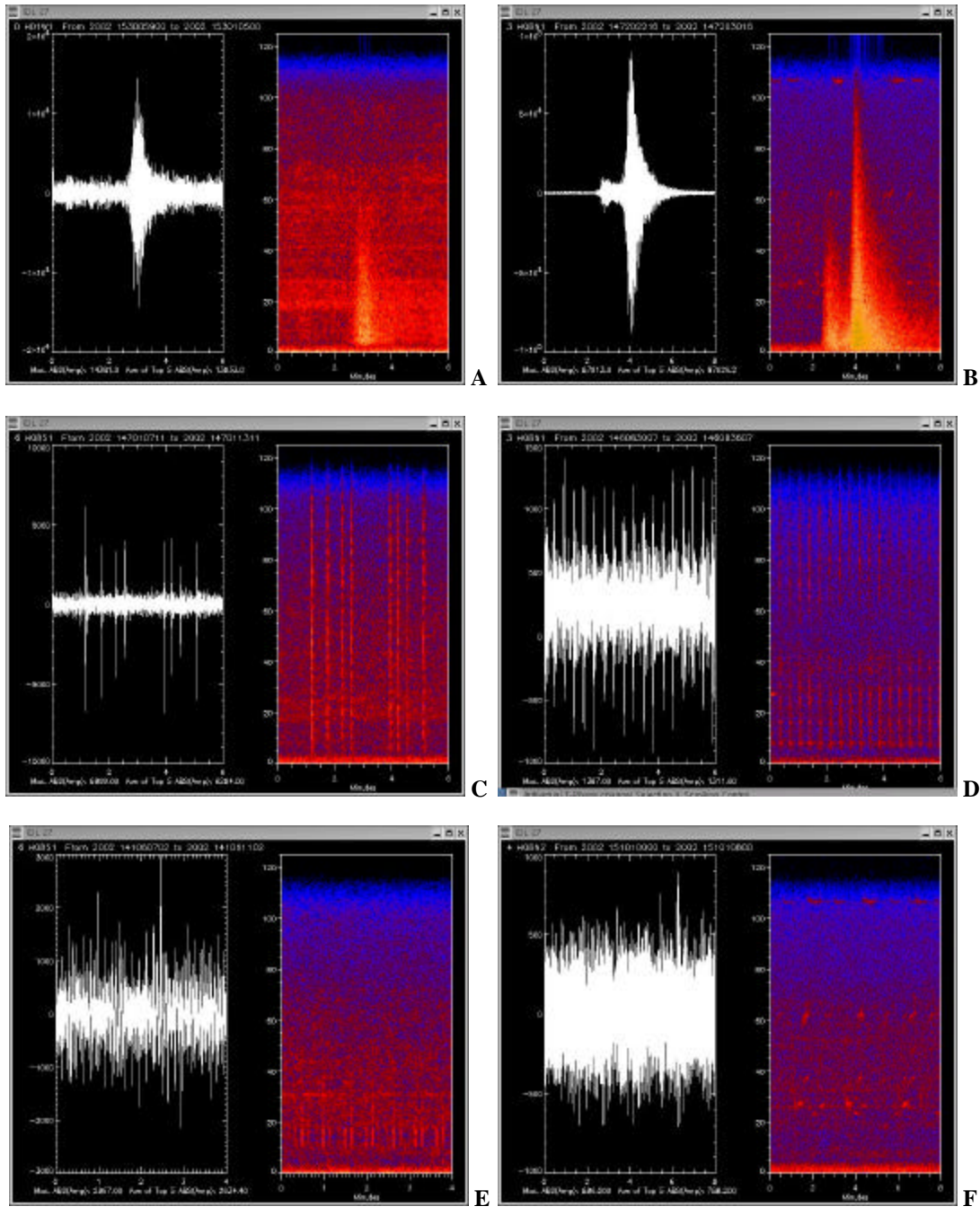


Figure 5: Examples of events observed regularly in the Indian Ocean. A) Typical T-wave arrival. B) P-wave arrival, followed by T-wave arrival. P-waves can be distinguished from T-waves by their more abrupt initiation. C) These ‘spikes’ look similar to airguns, but do not show the regular repeat intervals of airguns, and sometimes show up as individual spikes, without any indication of airgunning in the area before or after. These are of concern as possible explosive signals. D) Airgunning is frequently observed, but is easily distinguished from an explosion by its regular repeat interval (often 10 or 20 seconds). E) Fin Whale. F) Blue Whale.

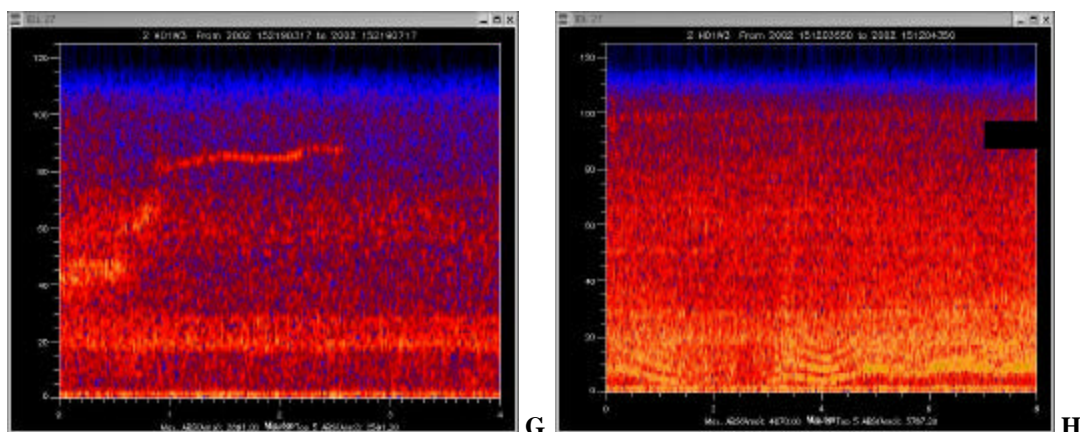


Figure 5. (continued) Examples of events observed regularly in the Indian Ocean. G) This high-frequency ‘screech’ may be biological in origin (perhaps a whale call). H) These low-frequency signals consist of monochromatic bands that evolve, or undulate, through time. They are similar in nature to T-phase signals associated with the movement of icebergs off the Antarctic shelf, as described by Talandier et al. (2002) from island stations in Polynesia.

A quantification of some of these signals for one week can be found in Table 1. Note final column on Table 1 is described as ‘sharp signals’. These refer to events similar to what is seen in Figure 5C, where there is a sharp signal that cannot be associated with airgunning or other obvious causes, and therefore may be explosive in origin. The number of events detected at any given station is likely to vary from week to week (or day to day as shown) depending on levels of local and regional seismicity, and seasonal variations in anthropogenic (shipping, airgunning) and natural (mammal vocalizations, ice movement) background noise sources. Such variation may impact our ability to detect and locate other signals.

This table represents the number of times each feature was identified in the hydrophone data. The P- and T-wave arrivals were marked every time an event was seen. The air guns were marked every hour making 24 the greatest number of events allowed in one day. The whale calls were marked each hour every time a unique signal was seen (i.e. one hour may be marked twice if different whale species were observed within that hour). Many individual whale calls lasts for over an hour and were marked for each hour in which they appeared.

Table 1. Event quantification for week of May 26th – June 1st 2002.

Day	T-Waves			P- and S-Waves			Air Guns (out of 24)			Whales			Sharp Signals		
	H01W	H08N	H08S	H01W	H08N	H08S	H01W	H08N	H08S	H01W	H08N	H08S	H01W	H08N	H08S
146	12	6	8	0	10	4	2	5	0	5	23	4	1	1	1
147	12	20	15	0	4	2	3	8	0	14	34	28	1	1	6
148	18	12	8	0	5	2	3	6	0	8	28	11	2	0	2
149	35	13	13	0	6	1	3	0	0	10	22	15	2	0	11
150	23	11	14	0	5	1	3	0	0	1	17	14	1	1	3
151	22	13	4	1	6	1	0	0	0	4	27	22	3	0	9
152	12	10	6	0	6	1	0	0	0	2	25	22	0	0	6
Total	135	85	68	1	42	12	14	19	0	44	176	116	10	3	38

Topographic Blockage

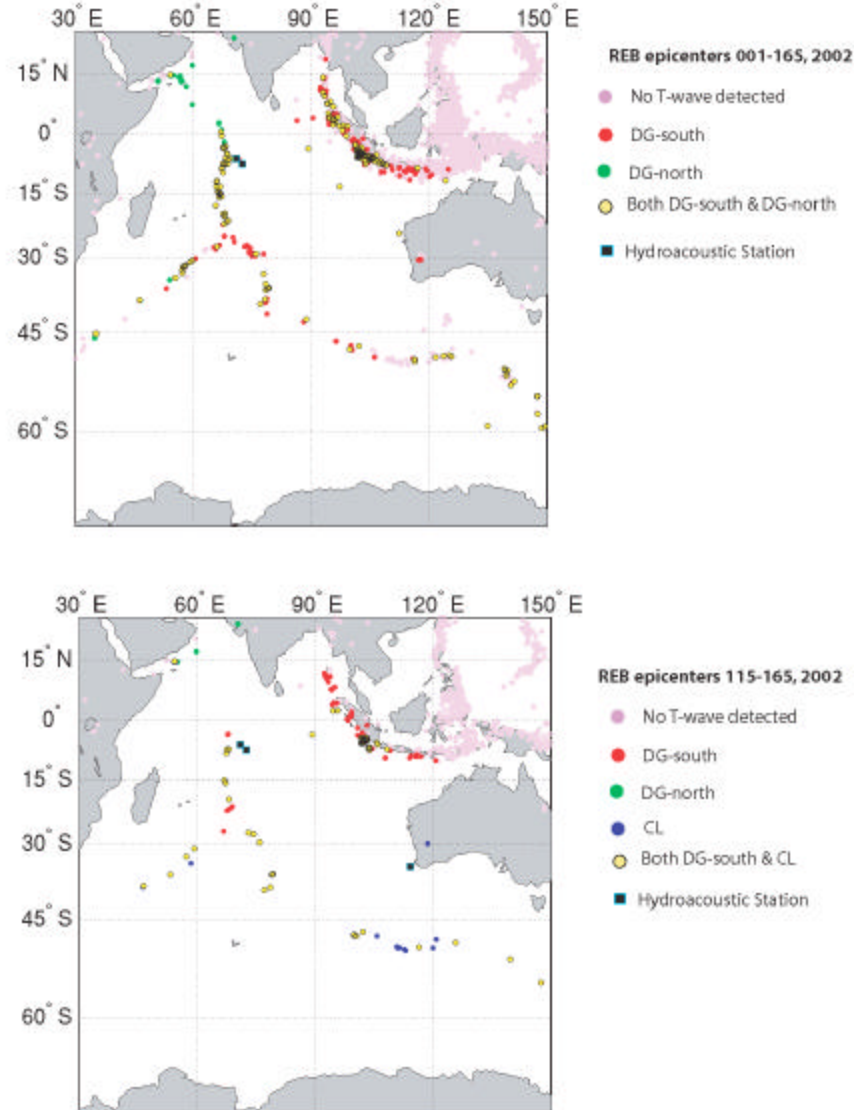
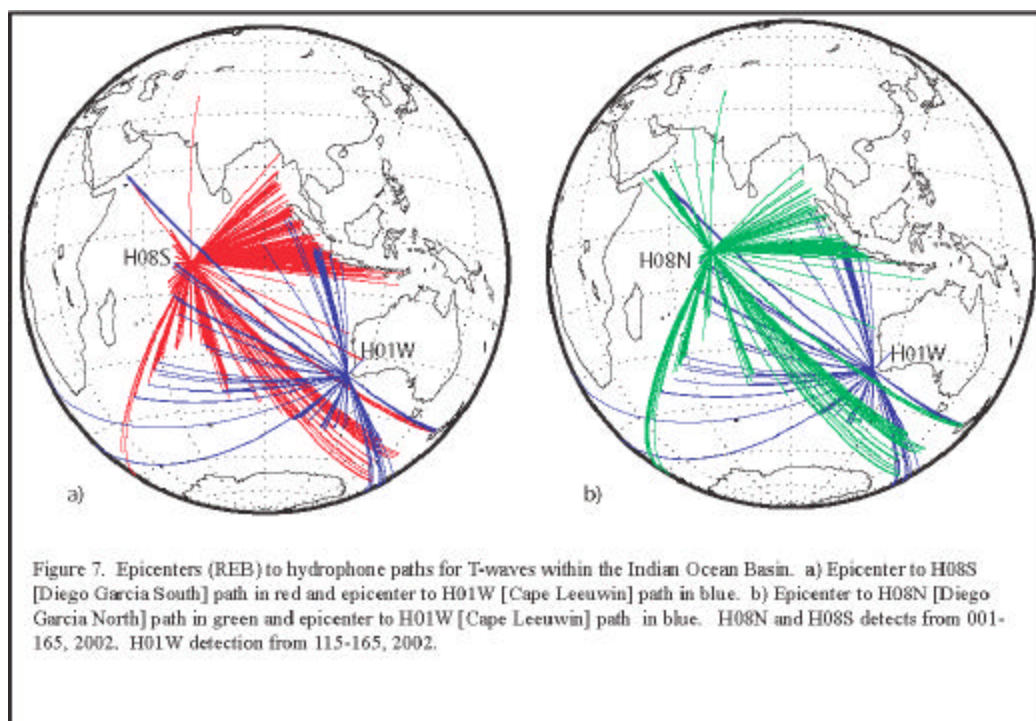


Figure 6. Locations of > 3.0 m_b events listed in the REB and observed at the Diego Garcia and Cape Leeuwin hydroacoustic stations. Top figure shows events for Julian days 1-165, 2002, for Diego Garcia stations only. Bottom figure shows events for Julian days 115-165, 2002, (CL arrival data become available through the REB on day 115) as observed on all three stations. Note that some events were observed at DG-North, as well as DG-South and CL, but are covered by the yellow symbols.

Predicted paths of topographic blockage can be modeled using seafloor bathymetry maps and station locations (e.g. Pulli and Upton, 2001); however, this is sometimes dependent on poorly known bathymetry and varies with event magnitude. Another approach is to examine the T-wave arrival records for known events, which were located using land station body wave arrivals (e.g. also Pulli and Upton, 2001). Below we present some initial results based on events observed in 2002. Figure 6 shows the events in the first 165 days of 2002 that were observed at Diego Garcia (HO8N & HO8S), as well as events that were observed at Cape Leeuwin (H01) and Diego Garcia from Julian days 115-165 (when Cape Leeuwin arrival data are available). These figures illustrate that there is reasonably good coverage to single stations within the Indian Ocean. Figure 7 indicates the raypaths for these hydroacoustically

detected events, and so provides a map of areas where complete blockage does not occur. However, there is also clear evidence that the magnitude of the event can impact degree of blockage. For example, in the top panel of Figure 5 there is a cluster of events at ~43S, 125E that are not observed at Diego Garcia South (HO8S). These events are aftershocks of a very large ($M_w=7.1$) earthquake in the same area in December 2001 that was observed at Diego Garcia South – (see Figure 4.). These much smaller magnitude events in early 2002 were not large enough to be detected above background noise at the H08, perhaps due in part to partial blockage associated with Broken Ridge (the elevated area running along ~32°S west of Cape Leeuwin).



Background Noise

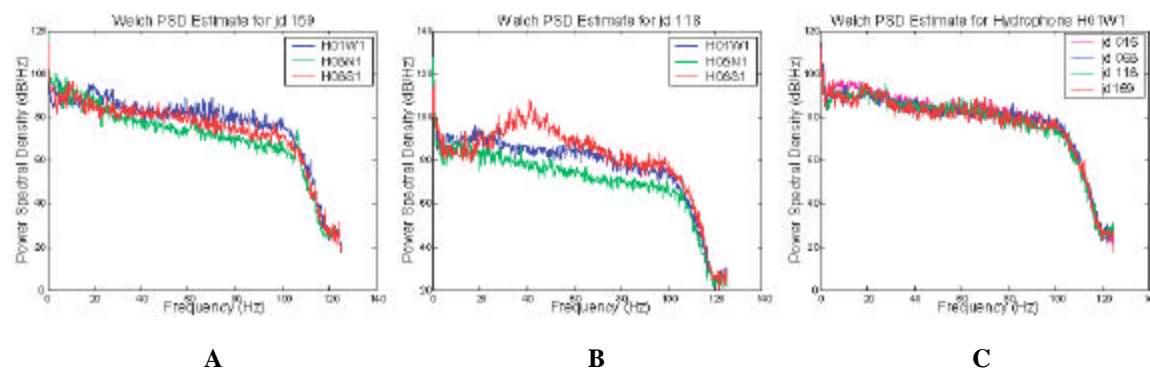


Figure 8. Daily noise spectra for HO8N, HO8S and HO1W. A) Spectra for Julian Day 159, 2002, at all three sites. B) Spectra for Julian Day 118, 2002, at all three sites. Note the influence of a particularly loud ship in HO8S (red). C) Spectra for various days from January 15th through June 8th at HO1W.

The background noise at hydrophone sites is controlled by a number of factors including proximity to shore (wave noise), weather variations and shipping in the area. The level of background noise is a critical factor in the ability of a station to observe specific events. As background noise increases, the detection sensitivity of the station decreases accordingly. Many noise sources are seasonal; therefore, it is important to characterize the noise for the full annual

24th Seismic Research Review – Nuclear Explosion Monitoring: Innovation and Integration

spectrum. Previous work at Diego Garcia (Hanson, 2001) has shown that Diego Garcia North is quieter than Diego Garcia South, and that both sites show a slight decrease (~3db) in noise level between January and July. Figure 8a illustrates that in general Diego Garcia North is quieter than Diego Garcia South, and that both are quieter than Cape Leeuwin. However, Figure 8b shows that this can vary on a daily basis when unusual noise sources are present. Figure 8c shows a snapshot of Cape Leeuwin daily noise profiles at various dates from January through May 2002. No clear seasonal variation is apparent, but since daily noise variations are susceptible to local events, a more detailed look at more days is required before drawing any conclusions. Eventually daily, weekly and monthly averages will be provided when a full year's data has been delivered and analyzed.

CONCLUSIONS AND RECOMMENDATIONS

We have adapted existing hydroacoustic processing software to read the CSS 3.0 format. This allows hydroacoustic data from the presently available H08 (Diego Garcia) and H01 (Cape Leeuwin) stations to be examined by an analyst in an efficient manner, viewing both amplitude traces and spectrograms. These modifications also will facilitate increased synergy between seismic (island or near shore stations) and hydroacoustic data sets.

As data from the H04 (Crozet) hydrophones become available, earthquake events will be located solely on the basis of T-wave arrivals. Previous work and limited ground truth in other ocean basins suggests this approach will improve significantly our ability to detect and locate moderate size earthquakes and other hydroacoustic signals.

Using the data presently available from H08 and H01, we have begun an effort to characterize and catalog sound sources within the Indian Ocean Basin. These include seismic phases, marine mammal vocalizations, airguns and possible ice-sheet movements. Initial noise estimates indicate that Diego Garcia South appears to be the quietest triad, followed by Diego Garcia North and then Cape Leeuwin.

Initial blockage results indicate good spatial coverage of much of the Indian Ocean by at least one hydrophone.

ACKNOWLEDGEMENTS

We thank E. Chapp for assistance in figure preparation and the analysis of these data. The NOAA/PMEL hydroacoustic software was developed over the course of many years by C. Fox, A. Lau, A. Schreiner and R. Dziak, and funded through the NOAA vents program.

REFERENCES

- Fox, C.G., H. Matsumoto, and T.-K. Lau (2001), Monitoring Pacific Ocean Seismicity from an Autonomous Hydrophone Array, *J. Geophys. Res.*, **106**, 4183-4206, 2001.
- Pulli, J.J., and Z.M. Upton (2001), Hydroacoustic Blockage at Diego Garcia: Models and Observations, *Proceedings of the 23rd Seismic Research Review*, Vol. II, 45-54.
- Hanson, J.A. (2001), Initial Analysis of Data from the New Diego Garcia Hydroacoustic Station, *Proceedings of the 23rd Seismic Research Review*, Vol. II, 12-22.
- Talandier, J., P.-F. Piserchia and E.A. Okal (2002), Hydroacoustic signals detected in Polynesia from mega-iceberg drifting in the Ross Sea, Antarctica, *abstract, annual meeting SSA, Seismological Research Letters*, **73**, 217.

**LOCALIZATION OF SUB-SEA EARTHQUAKES USING HYDROACOUSTIC REFLECTIONS AND
MATCHED-FIELD PROCESSING**

Zachary M. Upton and Jay J. Pulli

BBN Technologies

Sponsored by National Nuclear Security Administration
Office of Nonproliferation Research and Engineering
Office of Defense Nuclear Nonproliferation

Contract No. DE-AC03-02SF22560

ABSTRACT

The purpose of this study is to investigate the localization of long-range hydroacoustic events, such as sub-sea earthquakes and underwater explosions, received at a single monitoring station. A matched-field technique is used to predict synthetic waveforms that would be received at a hydroacoustic station for a given source location. A grid of potential source locations is selected based on the areas of natural seismicity defined by the mid-ocean ridges in the Indian Ocean and the subduction zones to the east (Carlsberg Ridge, Mid-Indian Ridge, Southeast & Southwest Indian Ocean Ridges, and Java Trench). This matched-field technique makes use of a previously designed propagation model (Pulli, *et al*, 2000) along with a detailed knowledge of bathymetry to predict arrivals at the receiver including reflections from bathymetric features. An earthquake detected at the Diego Garcia hydroacoustic station in the Indian Ocean, for which bathymetric reflectors have already been identified (Harben and Boro, 2001), is used to validate the synthetic waveform algorithm. Earthquakes in the Indian Ocean are then localized using the matched-field algorithm and signals recorded at Diego Garcia. These localizations are used to study the sensitivity of the matched-field algorithm. This research shows that hydroacoustic events can be localized using data from single stations if reflections from bathymetric features are included.

OBJECTIVE

The objective of this research is to assess the feasibility of using matched-field techniques to localize sub-sea earthquakes and underwater explosions using a single monitoring station and hydroacoustic reflections. Previous research has shown that reflected arrivals from an explosion or earthquake can be predicted for a given source-receiver pair. This study seeks to extend that work by creating a field of modeled waveforms and comparing them to the measured waveform using matched-field techniques.

The value of single station localization using hydroacoustic reflections is that it has the potential to extend the detection and localization coverage of the International Monitoring System (IMS) hydroacoustic network. Acoustic energy from a strategically placed explosion might have a direct acoustic path to only one IMS station. Worse, the energy might have no direct acoustic path. However, if reflections can be used as a basis for detection and/or localization, areas that were once not covered by the IMS hydroacoustic network could be considered within its coverage.

RESEARCH ACCOMPLISHED

Validation of reflector model in the Indian Ocean

The first step in this study was to validate past research on reflections for use in the Indian Ocean. Pulli, *et. al.* (2000) designed a model that, for a given source-receiver pair, calculated potential bathymetric reflectors in an ocean basin. The model used these potential reflectors to form the impulse response of the ocean basin. By convolving this impulse response with a synthetic source function, the model was able to predict a received waveform envelope based on the direct arrival and bathymetric reflections. Pulli *et. al.* (2000) then used this model to predict waveforms received at stations in the Atlantic and Pacific Oceans.

The Indian Ocean is chosen as the ocean basin for this study because of the IMS station HA08 located near Diego Garcia. This station not only provides a consistent, reliable source of hydroacoustic data, but it is the first IMS hydroacoustic station to begin to transmit data to the International Data Centre (Vienna, Austria) and Prototype International Data Center (Virginia, USA). Earthquakes regularly occur in the Indian Ocean and are a good source of acoustic information. Analyses of the signals from some of these earthquakes show what appear to be reflected arrivals (Harben and Boro, (2001); Hansen (2001).

In a paper written in 2001, Harben and Boro study a magnitude 6.8 earthquake that occurred January 18, 2000, near Jawa, Indonesia. Figure 1 is a map depicting the location of this earthquake, determined using seismic techniques, with respect to the Diego Garcia IMS station. The waveform envelope of this earthquake, recorded on the north array at Diego Garcia, is shown in the top graph of Figure 2. To validate the reflections model for use in the Indian Ocean, the model was run using the origin of the earthquake as the source location and a nominal, centralized location for the northern array of the Diego Garcia IMS station as the receiver position. The bottom graph in Figure 2 shows the synthetic waveform result of the model calculations.

Note that the major reflections at approximately 55 minutes and 59 minutes are identified by the synthetic waveform. Harben and Boro identify a reflector at the Seychelles/Mauritius Plateau that corresponds to the reflections at approximately 55 minutes. There is a peak in the envelope that is not in the replica waveform (at ~42 minutes). This peak could be the result of some non-reflected energy, like a low-level aftershock. It could also simply be a deficiency in the model that caused the discrepancy between the real and synthesized waveforms. These results are comparable to those in the Atlantic and Pacific Oceans, and therefore validate the use of the reflections model, and its resulting synthetic waveforms, in the Indian Ocean Basin.

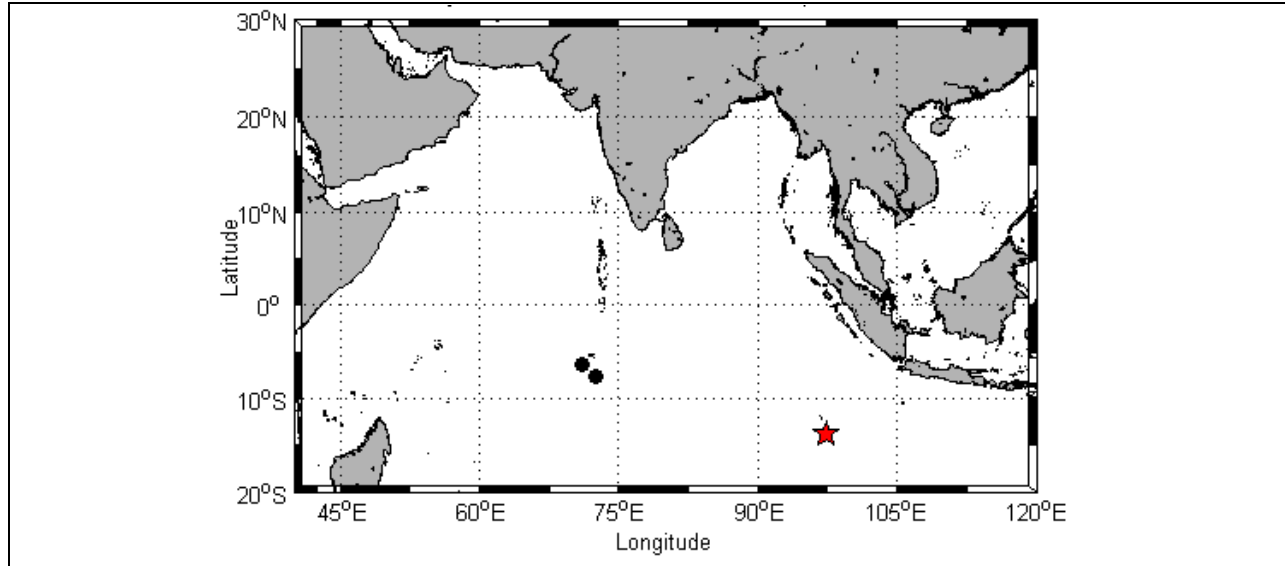


Figure 1. Location of the January 18, 2001, earthquake near Jawa, Indonesia (red star). The Diego Garcia IMS station is also shown in black circles.

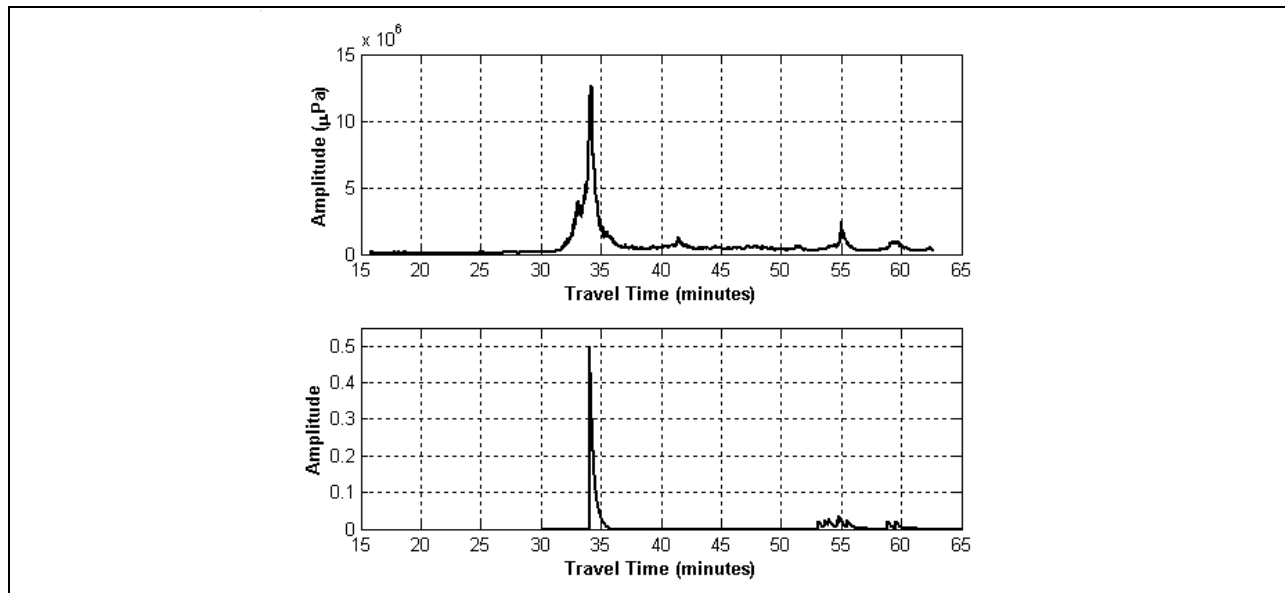


Figure 2. Real received waveform envelope from Diego Garcia North (top) and the output of the reflections model, the synthetic waveform (bottom).

Indian Ocean seismicity grid

The first step in the matched-field localization process was to generate a geographically disparate set of source locations. To attempt matched-field localization on an ocean-size scale, one might begin with a coarse grid of the entire ocean. However, time, measured data, and computer processing power were limiting factors in this research. There are no available recordings of explosions in the Indian Ocean. However, there are recordings of earthquakes. These earthquakes occur in a relatively limited number of geographic areas under the ocean (i.e. along mid-ocean ridges). Earthquakes, therefore, are an excellent source to test the methodology.

To minimize the time and processing power spent calculating synthetic waveforms, a series of source locations was selected that roughly matched the areas of peak seismic activity in the Indian Ocean. Figure 3 shows the map of

seismic activity in the Indian Ocean for 2000 and 2001 (United States Geological Survey) at left and the matched-field replica locations at right. The reflections model was used to create synthetic waveforms for each replica location.

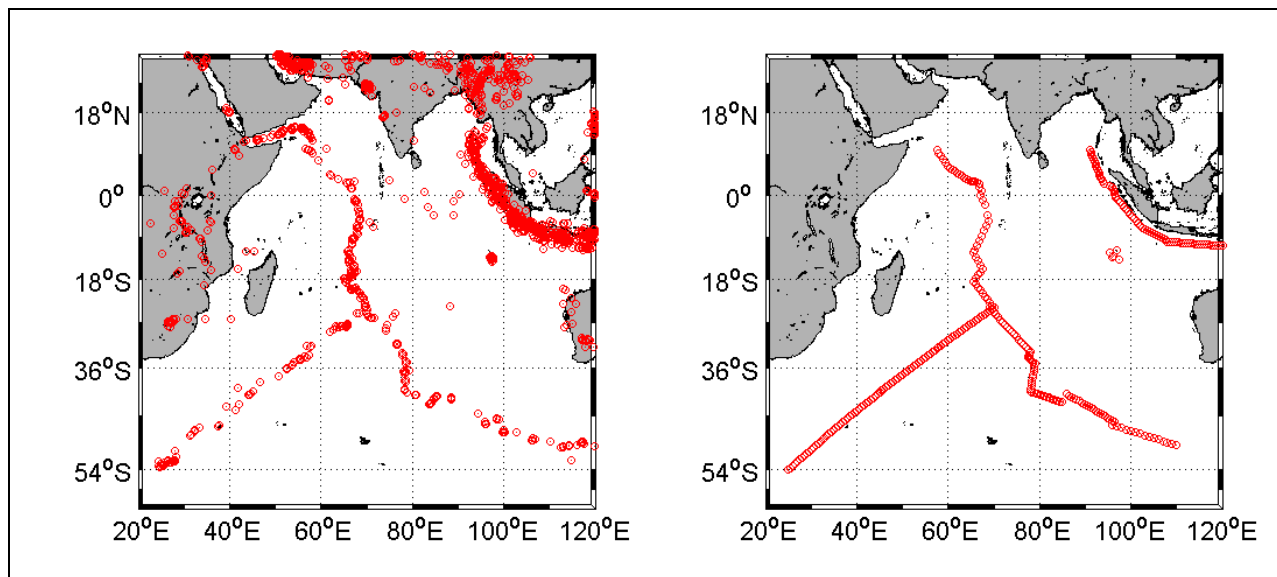


Figure 3. Map of seismic event locations for 2000-2001 (United States Geological Survey) at left, matched field replica locations at right.

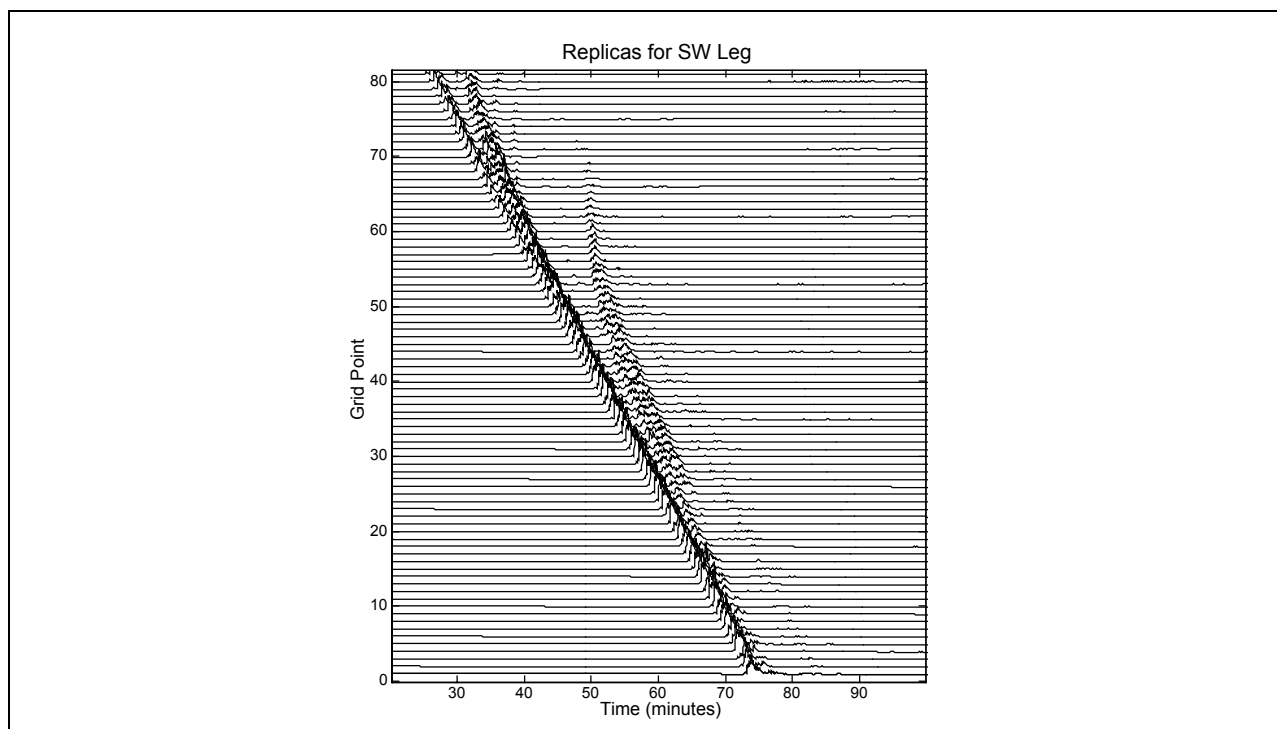


Figure 4. Synthetic waveforms for the Southwest leg of the source replica locations.

Localization Algorithm

A matched-field algorithm was developed to efficiently and effectively localize the earthquake signals and to display the results in a manner that was easily understood. Comparing 300+ replicas to over an hour of signal could be a very time consuming task. Since the only parts of the waveform that are of interest in the localization are the direct

and reflected arrivals, it makes sense to only correlate around them and not over the entire waveform. The real measured envelope is analyzed first. A noise estimate is calculated in 5-sec windows across the envelope. Since the noise estimate is only to be used as a basis for thresholding, it need not be terribly precise. Therefore, in each 5-sec window after the direct arrival time, the slope of the envelope is calculated using the beginning and end samples. Windows that have a slope greater than a prescribed maximum slope are considered signal. Windows with a slope less than a prescribed maximum slope are considered noise. An average value of noise is calculated within each of the noise windows. To detect the direct and reflected arrivals, a threshold is set above the calculated noise estimate. The points at which the waveform is above the threshold are considered direct or reflected arrivals and the rest of the waveform is set to zero. Figure 5 shows an example of the result of the noise estimate and detection. The top graph shows the original waveform. The bottom graph shows the detections in the thresholded waveform. These arrivals are found using a threshold of 6 dB above the noise estimate.

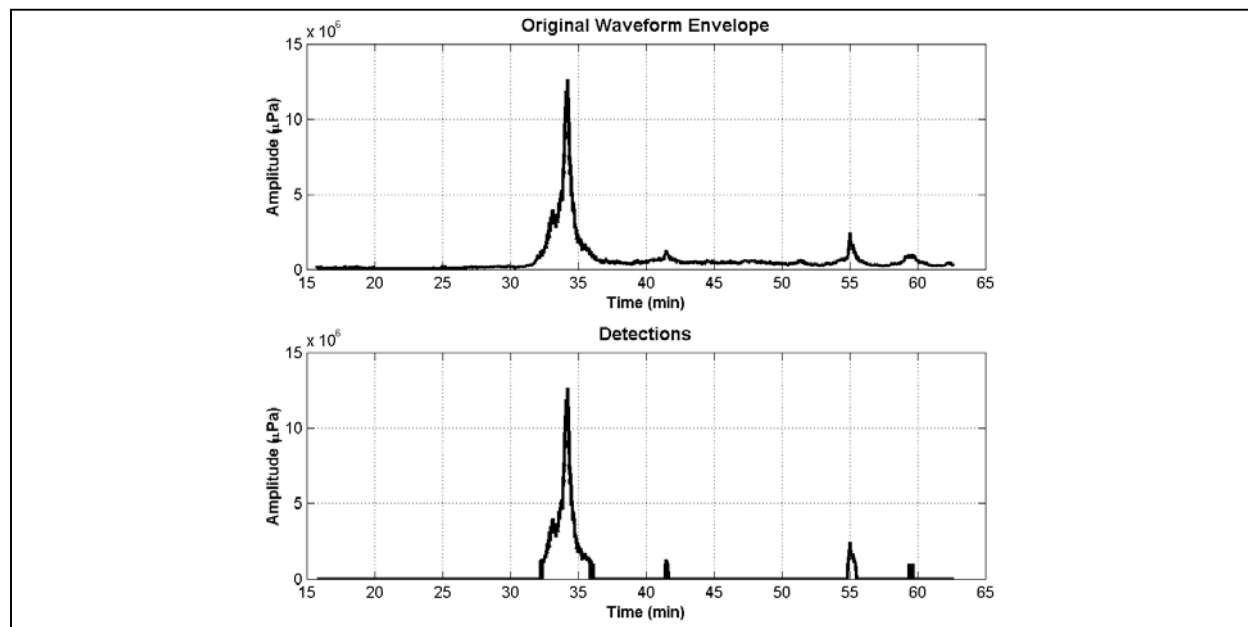


Figure 5. Waveform detection results.

To complete the matched-field localization, the replica waveforms are correlated with this thresholded waveform. However, in this instance and many others, the direct arrival is much stronger than the reflected ones. Each detection area (in time) is normalized by dividing by its maximum to consider the direct and reflected arrivals equally. This operation is performed on both the measured and the replica waveforms.

For the last piece of pre-processing before the actual localization, it is necessary to make sure that the direct arrival in the thresholded waveform would be correlated with the first arrival in the replica waveforms. This eliminates any large correlation between the direct arrival of the thresholded waveform and a reflected arrival in a replica. To achieve this goal, the replica is tested. If the time of the first arrival in the replica does not match the first arrival in the real waveform, the replica is set to zero around the time of the real direct arrival, thus eliminating the chance of any undesired high correlation. Reflected arrivals are correlated simply by their occurrence in time.

To correlate multiple replicas with the thresholded waveform, a loop is set up that cross-correlates the replica waveforms with the raw waveform during the detection time periods. Cross-correlations are performed in 5-sec windows. A replica waveform that is a strong match to the raw waveform in a particular time window has a high cross-correlation at the zero lag time. To determine the relative localization strength of a particular replica waveform, the zero-lag correlation is summed over the correlated waveform segments. Therefore, the replica with the highest summed zero-lag correlation over the direct and reflected arrivals is the strongest localization.

Display of results

Typically, matched-field localization results are displayed as ambiguity surfaces that allow the viewer to pick the most likely localization (for example, in range and azimuth). However, in this case, the potential source positions are located on an irregular grid over the areas of frequent seismicity in the Indian Ocean. The results of the localization are displayed on a map similar to that of Figure 3. However, in this case, the source locations are color-coded by their respective summed zero-lag correlation, with the blue end of the color spectrum being low correlation level and the red end being high correlation level. In this way an ambiguity ‘line’ is formed analogous to the traditional ambiguity surface. Jensen, *et al* (1994) provide more information on ambiguity surfaces.

Localization Case 1 – The January 18, 2000, Jawa, Indonesia, earthquake revisited

The localization algorithm was tested first using the Jawa, Indonesia, earthquake described in Harben and Boro, 2001. A map of the seismic (United States Geological Survey -- USGS) location of the earthquake was shown in Figure 1. The waveform envelope of this earthquake was shown in Figure 2. The detections have already been shown in Figure 2. The output of the localization algorithm is shown in Figure 6. The results displayed in Figure 6 show that the strongest localization strength, or the highest overall correlation occurred at the only red dot on the map. Table 1 is a comparison between the ground truth of the earthquake and the calculated location.

Table 1. Ground Truth Location vs. Calculated Location – Jawa, Indonesia, Earthquake

Location Type	Latitude	Longitude
Ground Truth Source Location (USGS)	13.802S	97.453E
Calculated Location	13.80S	97.45E

The results of this localization demonstrate that, when there is a grid point in close proximity to the event location, this algorithm can localize the event accurately. The distance between the ground truth location and the calculated location is 0.4 km. What is interesting in this result is that there is only one point in the area whose relative correlation level comes near that of the calculated location. Its correlation level, however, is only about two-thirds of that of the localization point. Therefore, based on only the initial test, the algorithm is fairly sensitive to location.

Figure 7 compares the replica waveform at the calculated location with the replica at the point that is nearest to it. These waveforms illustrate the difference in response that occurs with changes in location. The two points are 150 km apart.

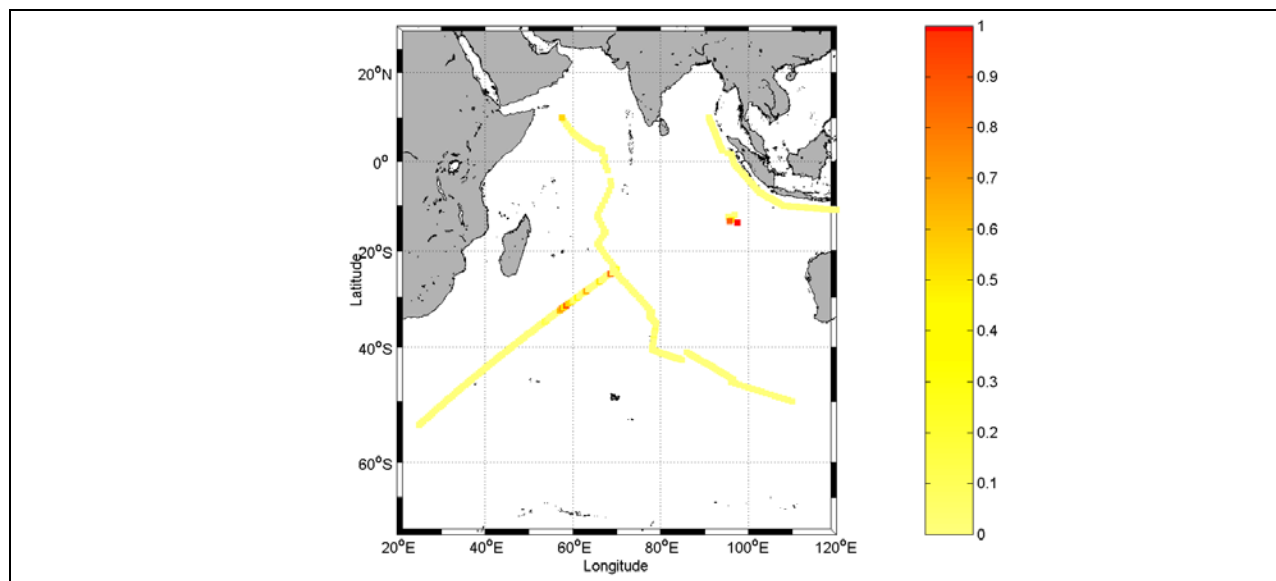


Figure 6. Visualization of the localization of the January 18, 2000, earthquake near Jawa, Indonesia.

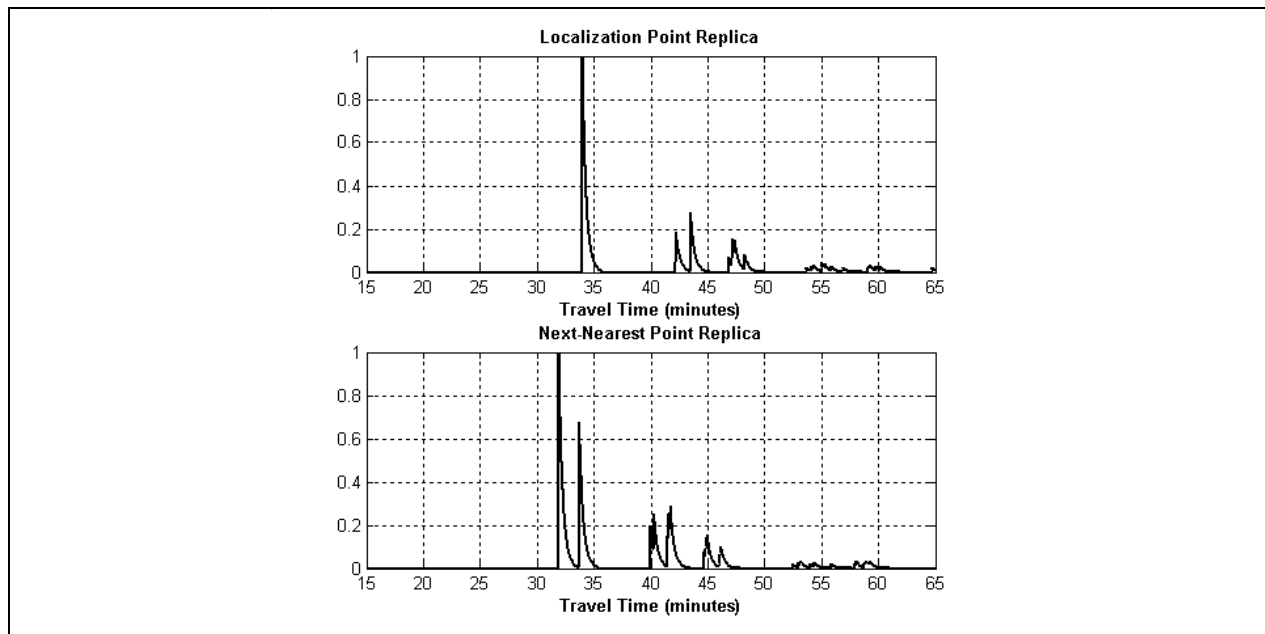


Figure 7. Comparison of the localization point replica with the next-nearest (geographically) replica.

Localization Case 2 – The April 19, 2001, Mid-Indian Ridge Earthquake

This 4.5- m_b earthquake is another event that exhibits direct and reflected arrivals suitable for study and attempted localization. The earthquake's ground-truth location and its relationship to Diego Garcia are shown in Figure 8. In contrast to the first case, there is not a replica source point within 50 km of the actual event location. The mid-ocean ridges are wide in comparison to the discrete grid of replica source locations, and this earthquake occurred away from the grid.

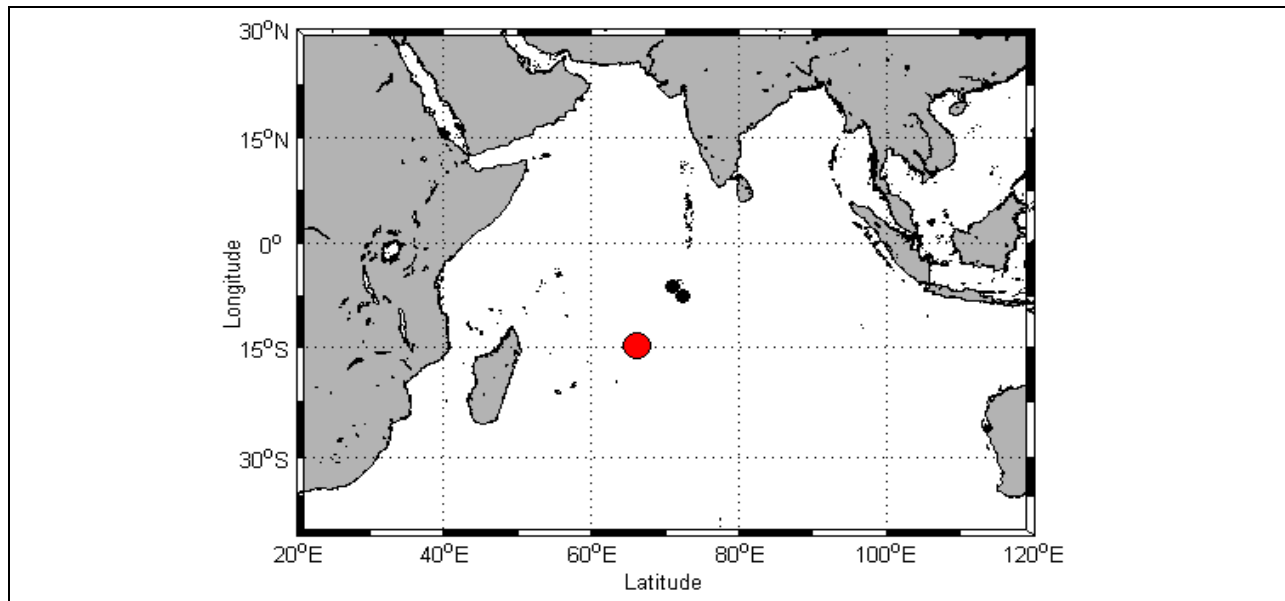


Figure 8. Location of the April 19, 2001, Mid-Indian Ridge Earthquake (red dot) and the Diego Garcia IMS Stations (black dots).

The earthquake's signal envelope, as recorded at the northern Diego Garcia array, is shown in Figure 9. The direct arrival (at ~12 minutes) and the reflected arrivals at 27 and 30 minutes, respectively, are immediately apparent. The localization algorithm output is shown in Figure 10. The comparison between the ground truth location and computed location is shown in Table 2.

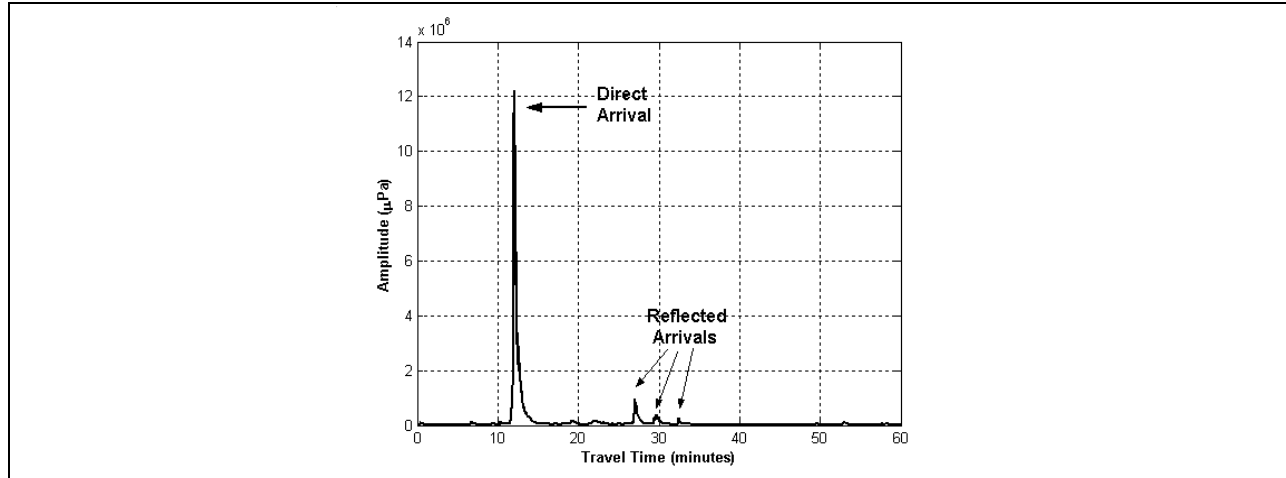


Figure 9. Waveform envelope of the April 19, 2001, Mid-Indian Ridge Earthquake as recorded at DGN.

Table 2. Ground truth location vs. localization location – Mid-Indian Ridge Earthquake

Location Type	Latitude	Longitude
Ground Truth Source Location (USGS)	14.63S	66.21E
Localization Location (Northernmost)	15.13S	67E
Localization Location (Southernmost)	23.67S	69.5E

The analysis of this localization is somewhat more difficult than the first event. The localization output shows two red boxes of nearly equal relative localization strength. The northernmost red box is near the earthquake location (101 km). The southern localization is much further from the earthquake location (1058 km).

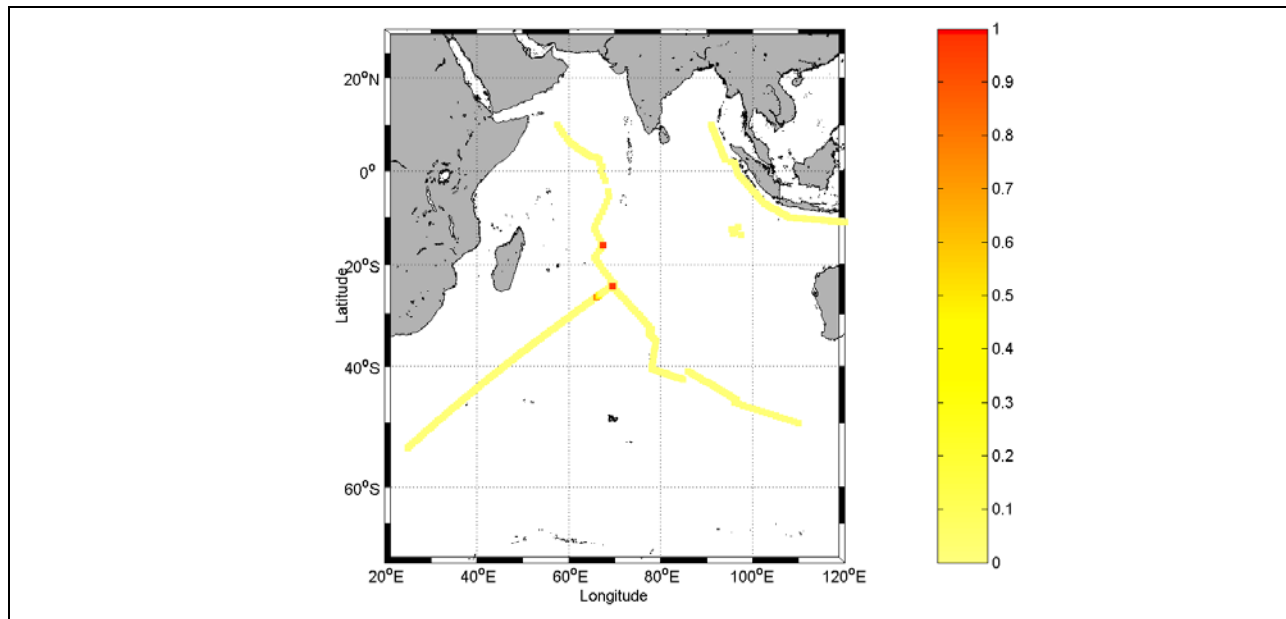


Figure 10 . Localization Algorithm Output.

Many factors could contribute to this result. First, there is not a grid point in close proximity to the earthquake. In the first example, it was shown that the algorithm is very sensitive to location. For an earthquake localization in which the event location does have a corresponding grid point, the surrounding points could be much weaker in correlation level. Therefore, the fact that the localization algorithm produced two localizations in this case is not a surprise. Second, the localization algorithm, as designed, eliminates the amplitude discrimination capability of the cross-correlation function. By normalizing all the arrivals (direct and reflected) by their respective maximum value, the direct and reflected arrivals were weighted equally in terms of the correlation. However, in doing so, the relative strength of the arrivals is masked, since each arrival will have a peak value of one.

CONCLUSIONS AND RECCOMENDATIONS

In this study, it has been shown that long-range hydroacoustic reflections can be used as a basis for the creation of replica waveforms, at a specific receiver location, for a geographically disparate set of source locations. It has also been shown that these replica waveforms can be used in a matched-field localization algorithm to determine the source location of an acoustic signal.

The localization algorithm exhibited sensitivity to the location of the replica positions. If there was a grid point near the event location, the event could be accurately localized. Also, nearby grid points did not exhibit spurious high localization strengths that might damage the accuracy of localization. However, in the case of an event that did not have a nearby replica grid point, the algorithm produced a dual localization. One of these localizations was a true localization, in that the grid point selected was near the event location. However, the other localization point was over 1000 km away from the event location. The two results, though very different, yield some similar conclusions. This algorithm is capable of localizing sources on an ocean-basin-sized scale. However, for the algorithm to make accurate localizations anywhere in the ocean, the grid of potential source locations would have to be fairly dense. The density of the grid, in fact, would probably have to be correlated to the desired localization accuracy.

Though the results of this study are very encouraging, there are many areas of research that could improve the capability of localizing events using long-range hydroacoustic reflections. The most obvious is to extend the calculations here to a grid of an entire ocean. A whole-ocean case would validate this method for use in the IMS. The localization algorithm and reflections models exhibit a few weaknesses that are worthy of further study. For instance, the localization algorithm deliberately eliminates the amplitude discrimination power of cross-correlation. A limited amount of change to the pre-correlation processing could allow the localization algorithm to take full advantage of this characteristic.

A brief list of other possible future study areas follows:

- A study of reflector strength calculations. In the current synthetic waveform model, the amplitudes of the arrivals do not match well to the data. Including a better calculation of reflector area or a better impulse response weighting function might improve the match between synthetic and reflected data.
- A study on the use of higher resolution bathymetry to develop a better measure of bathymetric slope in the reflections model. In what direction should slope be calculated? How can the directional gradient be determined? This study could be performed using higher resolution topographic databases to obtain an accurate, yet unclassified result.
- An investigation of the use of different source functions for convolution with the ocean basin impulse response model in the reflections model. Is there a better source function that is both more representative of the event in question and provides better synthetic replicas?
- An investigation of the use of more than zero-lag correlation. Is there a method that will yield better localizations?
- An investigation of the use of back-azimuth calculations in conjunction with travel time to improve the reflections model.

24th Seismic Research Review – Nuclear Explosion Monitoring: Innovation and Integration

Finally, HydroCAM, the modeling software used to perform the travel-time calculations for this study, assumes a source in the water column when it makes its travel-time calculations. Earthquakes occur many kilometers below the ocean floor. For an earthquake that takes place 30 km under the ocean floor, seismic waves must travel in earth for about 30 km before their energy is converted to sound. Assuming a seismic velocity of approximately 6 km/sec, these waves will take about 5 sec to reach the earth/water interface. The best modeling of earthquakes that could be accomplished in this research was to set up the source on the bottom of the ocean. In the scope of calculations that span hours, the 5-sec bias does not seem to hamper localization, but a final topic of future study would be to analyze the benefit of adding a few seconds to the travel-time measurements to account for this bias.

ACKNOWLEDGEMENTS

The initial research and development of the reflections model for this study was performed under Defense Threat Reduction Agency (DTRA) contract number DSWA 01-97-C-0164. Additional support was provided through internal funding at BBN Technologies. We thank Phil Harben of Lawrence Livermore National Laboratory for providing data and insight during the course of this work. We also thank Dr. Anthony Lyons of Penn State University for useful discussions and suggestions.

REFERENCES

- Angell, J., T. Farrell, and J. Pulli (1998), Characterization of reflected hydroacoustic signals, Proc. 20th Annual Seismic Research Symposium, 650-659.
- Bendat, Julius S. and Allen G. Piersol. *Engineering Applications of Correlation and Spectral Analysis*. Second Edition, John Wiley and Sons, Inc. 1993.
- Hanson, J. (2001), Initial Analysis of Data from the New Diego Garcia Hydroacoustic Station, 23rd Seismic Research Review, Jackson Hole, WY, LA-UR-01-4454.
- Harben, P. and C. Boro. (2001), Implosion Source Development and Diego Garcia Reflections, Proc. 23rd Seismic Research Review, Jackson Hole, WY, LA-UR-01-4454.
- Jensen, Finn B, W.A. Kuperman, M.B. Porter, and H. Schmidt. *Computational Ocean Acoustics*. American Institute of Physics. 1994
- Pulli, J.J., Z. Upton, R. Gibson, T. Farrell (2000), Modeling Long-Range Hydroacoustic Reflections in the Atlantic and Pacific Oceans, Proceedings of the 22nd Seismic Research Symposium, New Orleans, LA, Defense Threat Reduction Agency, OMB No. 0704-0188.
- Pulli, J.J., T. Farrell, and R. Gibson (1999), Characterization and utilization of hydroacoustic signals reflected from continents and bathymetric features, 21st Seismic Research Symposium, Las Vegas, NV, LA-UR-99-4700.

